YOKOHAMA NATIONAL UNIVERSITY

DOCTORAL THESIS

A Numerical Investigation on the Aerodynamic Properties of the Wavy Circular Cylinders

Author:
Kai ZHANG

Supervisor:
Prof. Hiroshi KATSUCHI
Prof. Dai ZHOU
Prof. Hitoshi YAMADA

A thesis submitted in fulfillment of the requirements for the degree of Doctor of Engineering

in the

Department of Civil Engineering

August 8, 2017

Declaration of Authorship

I, Kai ZHANG, declare that this thesis titled, "A Numerical Investigation on the Aerodynamic Properties of the Wavy Circular Cylinders" and the work presented in it are my own. I confirm that:

- This work was done wholly or mainly while in candidature for a research degree at this University.
- Where any part of this thesis has previously been submitted for a degree or any other qualification at this University or any other institution, this has been clearly stated.
- Where I have consulted the published work of others, this is always clearly attributed.
- Where I have quoted from the work of others, the source is always given. With the exception of such quotations, this thesis is entirely my own work.
- I have acknowledged all main sources of help.
- Where the thesis is based on work done by myself jointly with others, I have made clear exactly what was done by others and what I have contributed myself.

Signed:

Date:

Abstract

Driven by the need to mitigate the drag and vibration of the typical cables structures, the current thesis is dedicated to a numerical investigation of the aerodynamics associated with the flow around wavy circular cylinders. This is inspired by the successful flow control of the span-wise waviness found in several marine mammals and their biomimicry innovations. Based on the promising flow control efficacy of the wavy cylinder as has been reported by previous researches, the current work embark upon a detailed analysis of the wavy cylinder at two more complicated conditions.

Firstly, the stationary wavy cylinder subjected to the inclined incoming flow is considered. Three inclination angles, 0°, 30° and 45°, together with 2×2 combinations of shape parameters, namely $\lambda/D_m = 2$ and 6, $a/D_m = 0.1$ and 0.15, have been taken into consideration. The aerodynamic force coefficients in terms of both the span-wise averaged and sectional values are discussed at length. It is revealed that the growing inclination angle invites not only a surge in their span-wise averaged values, but also an enlargement in the sectional difference of the force coefficients. The span-wise correlation of the lift force is found to be enhanced for the wavy cylinders with the increase of inclination angle, while the opposite is true for the normal cylinders. By examining the mean wake properties, it is disclosed that the increase in the span-wise averaged drag force coefficients is closely related to the shrinkage in the vortex formation length and the regression of the base pressure, whereas the sectional distribution of the drag coefficients is largely affected by the stagnation pressure. The mean wall shear stress fields are exploited to shed light on the flow topology of the cylinder surfaces. It is discovered that the wavy cylinders, especially the short-wavelength one, exhibit significant span-wise variation in the separation structure in the inclined flow. Besides, the chaotic surface flow in the rear side of the non-inclined cylinders could be regulated to maintain symmetry by the secondary axial flow in the near wake of the inclined cylinders. The instantaneous three-dimensional vortical structures are visualized by the Q isosurfaces at last to collaborate the previous discussions. A preliminary mechanism for the cessation of flow control efficacy for the wavy cylinders in inclined flow is also presented.

The second contribution of this thesis is that for the first time, the vortex-induced vibration of the wavy cylinder is systematically studied. To this end, the wavy cylinder is mounted flexibly on a spring-damper system and its aeroelastic response to the normal incident stream is studied over a range of interested reduced velocities. It is discovered that the wavy cylinder, although almost eliminates the Kármán vortices in the fixed configuration, shows only limited efficacy on the mitigation of the flow induced vibration in the case of zero structural damping, and the typical initial-upper-lower type response curve is manifested. The aerodynamic forces of the wavy cylinder also magnify significantly in the flexibly mounted cases during synchronization. Moreover, the phase lag between the lift coefficient and the displacement displays a clear change from 0° at the initial branch to 180° at the lower branch. The association of the $2S$ and $2P$ vortex shedding modes to the different branches is also similar to that of the normal cylinder, in which the $2S$ mode corresponds to the initial branch and the $2P$ to the lower branch. In general, despite the absence of the primary shedding frequency in the fixed configuration, the flexibly mounted wavy cylinder exhibits many features that is also found in the normal cylinder. This implies that the vortex induced vibration may not be initiated by the Kármán vortex shedding, and thus may defy the conventional view on the mechanism of the vortex induced vibrations. Additional simulations are performed with non-zero structural damping. It is disclosed that with sufficiently high structural damping, the vibration of the wavy cylinder could be reduced more efficiently than the normal cylinder.

The considered two cases clearly indicates that the aerodynamic behavior of the wavy cylinder is more complicated than what we have expected. Engineering applications of the wavy cylinder should be considered with caution, since direct implantation of this morphology to cable structures may not lead to the desired performance. This thesis should trigger more research topics associated with the wavy cylinders.

Acknowledgements

I consider myself very lucky to have the chance to study and finish my master and doctoral courses at Yokohama, not only because of its beauty and quietness, but more importantly the lovely people here.

My chief advisor, Prof. Hiroshi Katsuchi, has led me into the interesting and challenging topic of cable aerodynamics, and has always been there for me whenever I consult him for council. I enjoyed the fruitful academic discussion with him as well as the personal communications with him. This thesis is the outcome of his support and advice during the 3 years. Appreciation also goes to my associate advisors, Prof. Hitoshi Yamada and Prof. Dai Zhou, who have helped and guided me a lot in the course of my Ph.D. research. It is also because of them that I have the privilege to become the first student under the double-degree agreement between Shanghai Jiao Tong University of China, and Yokohama National University of Japan. The studentship at two universities has greatly accelerated my researches since I could enjoy computational resources, access to academic journals and guidance from both sides.

Prof. Nisiho, Dr. Kim, Prof. Dion and Prof. Fujino are thanked for their inspiring comments in the lab seminars and beneficial personal communications. Dr. Vo, Dr. Naimul and Dr. Dat are thanked for the exchange of ideas on the wind engineering problems here at YNU. My friends from the SJTU lab, Dr. Tao He, Dr. Zhaolong Han, Dr. Yan Bao, Dr. Jiahuang Tu, are thanked for their constant regards and the heated discussion on the fluid mechanics problems.

I would also like to thank all of my previous and current laboratory members for their kind cooperation, support and assistance. I enjoyed the lab trips, all kinds of parties at the sixth floor, and the Nomikai at Wadamachi as well as Yokohama Station. Specially, I would like to thank Mr. Junya Mizutani for being the best tutor during my first half year in Japan. Outside the campus, Mr. Taketoshi Funo from Mitsui Volunteer Group has also helped and guided me a lot in my daily life and my Japanese language study. I am highly obliged and grateful to Japanese government for supporting me with the MEXT scholarship during my master and Ph.D. researches. In the future, I hope I could return the favor and hospitality I have received from the Japanese people.

I have not been able to accompany and look after my parents while I'm in Japan. For the past 30 years, they have provided me with the best they could and are always supportive of my academic pursuit. I would like to express my biggest gratitude to them. This thesis is dedicated to my lovely wife, Yijun Ren, for her unconditional love, patience and understanding. There are sunny and rainy days in life, and it is best to have you by my side.

Kai Zhang
Gumyoji, Yokohama
August 8, 2017

Contents

List of Figures

List of Tables

Chapter 1

Introduction

1.1 Span-wise waviness as flow control approach

Humpback whale (Megaptera novaeangliae) is known as the only baleen whale that relies on maneuverability to capture preys. The extraordinary mobility of this marine mammal is believed to originate from the elongated pectoral flipper, which varies from 0.25 to 0.33 of the total body length (Edel and Winn, 1978). In addition to its scale, the uniqueness of the flippers also lies in the large protuberance or tubercles located sinusoidally on the leading edge, rendering the surface a scalloped appearance (Fish and Battle, 1995). This particular morphology has been shown to maintain high lift and avoid stall at large angles of movement, thus contributing to the enhanced maneuverability (Fish and Battle, 1995).

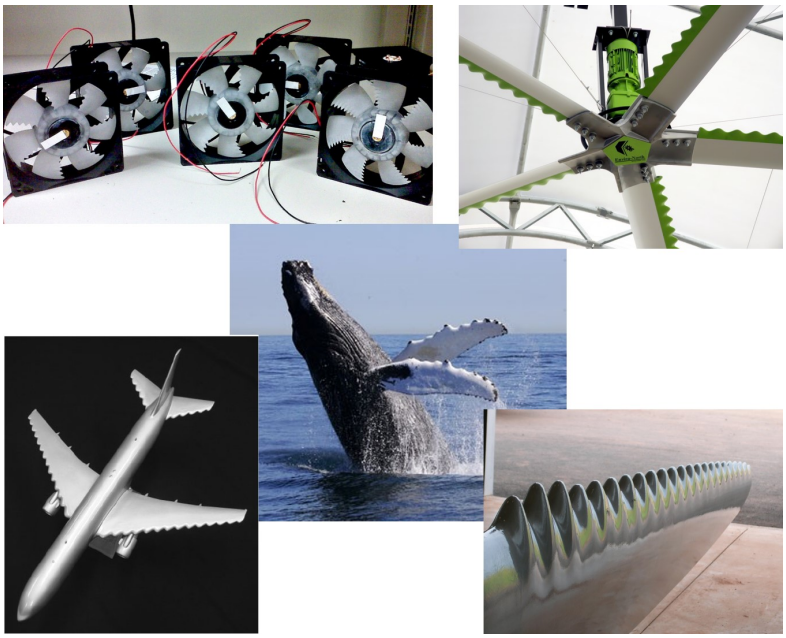

FIGURE 1.1: Bio-mimicry innovations stemmed from the tubercles of the humpback wale flippers. *Middle*: A humpback whale breaching out of the sea. The tubercles on the flippers could be clearly observed. *Top left*: Computer fans equipped with tubercles. Top right: Eco-friendly ceiling fans. *Bottom left*: Conceptual model of commercial jet airliner with leading edge tubercles on the wings and stabilizers (Fish and Lauder, 2006). *Bottom right*: Windmill blade utilizing leading-edge tubercles. Sources of the photos, except stated, are from the WhalePower Tubercle Technology.

Many bio-mimicry innovations, exploiting the *tubercle effect*, have emerged since the

work of Fish and Battle (1995). Some of them are shown in Fig. 1.1. The blades with span-wise waviness in the leading edges, according to the tests of the WhalePower Tubercle Technology[1], have been proven to exhibit significant aero/hydrodynamic performance over the normal wings in that they deliver previously impossible high stall angles, more gradual stall as well as increased lift force in the higher pitch operation. There has also been persisted efforts in the understanding more of the characteristic associated with the wavy leading edge wings/turbines (Miklosovic et al., 2004; Yoon et al., 2011; Weber et al., 2011; Wei, New, and Cui, 2015; Johari et al., 2007; Hansen, Kelso, and Dally, 2011). It is anticipated that this new kind of hyper-stable flow management device has the potential to reform millions of products and even the whole industries.

Coincidently, another marine mammal, the harbor seal (*Phoca vitulina*), has also been revealed to be blessed with such span-wise waviness in their whiskers, as is shown in Fig. 1.2. The whisker, which takes the form of an ellipsoidal cross-section with regularly repeating sequence of wavy profiles along its length, have been demonstrated of high efficacy in alleviating the hydrodynamic forces and mitigating the self-excited vortex-induced vibrations (Hanke et al., 2010; Witte et al., 2012). This allows a harbor seal to detect the velocity magnitude several orders lower than the velocity of the flow in the wake of swimming fish (Dehnhardt, Mauck, and Bleckmann, 1998; Dehnhardt et al., 2001). The biomimetic potential of this discovery has already been exploited in some marine robotics sensory applications (Beem, Hildner, and Triantafyllou, 2012; Kottapalli et al., 2015).

FIGURE 1.2: The whisker of the harbor seal exhibits waviness in the span-wise direction. .
source: http://www.whoi.edu/oceanus/feature/seal-whiskers-inspire-marine-technology

Contrary to the intuitional belief that a smooth, contoured morphology is generally favored in the engineering applications, the above two examples serve as solid evidence that well-designed undulations could lead to better hydro-dynamic performance for the two marine mammals. The extraordinary flow control efficacy of the span-wise waviness has already spurred several innovative applications, and there should be room for more.

1.2 Motivation for the current thesis

In recent years, there has been a surge in the construction of long-span bridges over the world. Fig. 1.3 shows an overview of the famous Sutong bridge, which ranks as the world's second longest cable-stayed bridge at the time of writing. An essential part of such bridge, as its name suggests, is the stay cables. Being long and flexible in nature, such structures are constantly plagued by the excessive aerodynamic forces and various

[1] https://whalepowercorp.wordpress.com/

kinds of vibrations. It is estimated that for a typical cable-stayed bridge over 1000 meters, the wind load on the cables usually exceeds that on the deck and pylon (Hojo, Yamazaki, and Okada, 2000; Svensson, 2013). Although the static force on the cable is of minor importance to the cable itself, it could present a significant design factor as the drag load transfers to the main structural elements such as the girder and pylon. A more notorious problem that concerns the cable engineers is the rain-wind induced vibration (RWIV), which usually occurs under the combination of moderate wind speed with precipitation. The generally accepted explanation for the mechanism for RWIV is the formation of the upper water rivulet, which negatively alters the aerodynamic stability of the cable and lead to vibrations with large amplitude and low frequency (Matsumoto, Shiraishi, and Shirato, 1992). Aerodynamic countermeasures to the RWIV usually takes the form of surface profiling to disrupt the continuous formation of the water rivulets, such as the helical spiral protuberances (Larose et al., 2013), circular rings (Vo et al., 2016), concave fillets (Burlina et al., 2015; Burlina et al., 2016) etc. However, these surface treatments usually result in an enlargement of the effective diameter of the cylinder, which indicates larger drag forces for the stay cables. In view of above, the problem of designing a suitable cable profile, which exhibits low drag and resistance to various vibration phenomenon, remains challenging and patenting.

FIGURE 1.3: Left: an overview of the Sutong Bridges, the world's second longest cable-stayed bridge, from Changshu city, China. Right: A model of the Nanhai Shengkai drilling vessel at Naval Architecture and Ocean Engineering Bldg., Yokohama National University.

A similar problem with the bridge cables is also encountered by the offshore drilling risers, which, for the need of subsea oil and gas exploration, are often suspended thousands of meters beneath the water surface (right picture in Fig. 1.3). Constantly attacked by the ocean currents, these long and flexible structures with low mass ratio are vulnerable to the hazardous vortex-induced vibrations (VIV), whose detrimental effects to the risers are two-fold. Firstly, the effective drag coefficient could increase up to twice the value of a riser that is VIV-free; more importantly, due to the oscillation of the riser, alternative bending stress could lead to a loss of the fatigue strength. One of the most

common types of VIV suppression devices for the drilling risers is the helical strakes. Well-designed strakes could reduce the fatigue damage by over 80%, at the cost of increased drag forces. Fairings have been an effective alternative to strakes without the drag penalty for the risers. However, they are more expensive due to the cost themselves as well as the additional rig time required to install during the riser running (Chakrabarti, 2005).

In order to address the problems described above, it is tempting to apply the spanwise waviness, which has been proven effective in flow control by the humpback whales and the harbor seals, as well as the bio-mimicry innovations inspired therefrom, to the stay cables and drilling risers, both of which are long and flexible structures that are susceptible to fluid induced forces and vibrations. The morphology of the harbor seal whisker could easily be extended to the cable structures, with the circular cross-section replacing the ellipse to account for the omni-directionality of the incoming flow in practical situations. A sketch of the resulted shape, referred to as the wavy circular cylinder, or wavy cylinder for short, is depicted in Fig. 1.4.

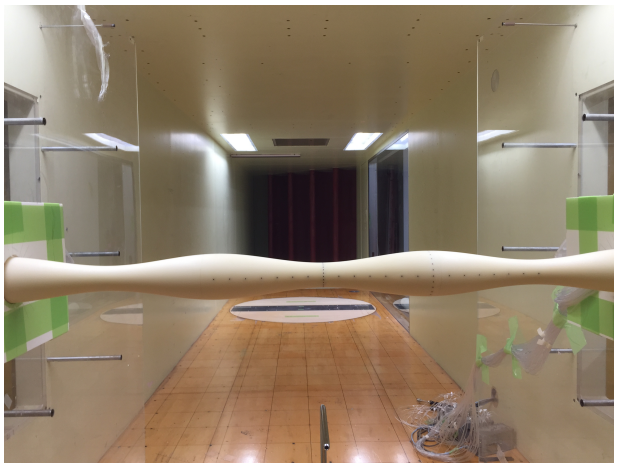

FIGURE 1.4: The wavy circular cylinder

The cross flow past such a geometry has been subjected to extensive researches in the literature, as will be reviewed in Chapter 2. Most of the works have indicated that such a cylinder could significantly modify the wake topology and reduce the aero/hydrodynamic forces. In spite of the abundant researches, there are still quite a lot to explore if such a geometry is to be used in engineering applications such as the stay cables, overhead transmission lines and drilling risers. First of all, there is no general consensus on the aerodynamic properties of the wavy cylinder placed inclined to the incoming flow, since under such configuration the additional axial velocity components hits the wavy tubercles directly and may lead to undesired magnification of the aerodynamic forces. Secondly, while the flow control efficacy of the wavy cylinder in the static cases is generally acknowledged, whether or not it could suppress the vortex-induced vibrations still remains unsolved. Based on the above considerations, we embark upon a curiosity study on these interesting problems by the means of numerical simulation. It is anticipated that the current thesis could shed some light upon aerodynamic performance of the wavy cylinder in the inclined and dynamic configuration. Ultimately, it is the hope of the author that this work should be useful for the potential engineering use of the wavy cylinders.

1.3 Thesis layout

The current thesis is organized as follows. After the general introduction to the span-wise wavy flow control technique in the current chapter, a more detailed literature review is presented in Chapter 2. This review looks at the general aspects associated with the cylinder cross flow, followed by an attempt of new classification of the flow control techniques. Chapter 3 lays the numerical foundation to the current paper. The following texts discuss the main work of the current thesis. Firstly, the flow control efficacy of the wavy circular cylinder in the inclined flow is visited in Chapter 4 by means of large eddy simulation. Next, Chapter 5 is dedicated to the simulation of free vibration of a wavy cylinder that totally suppress the Kármán vortex shedding in the fixed configuration. The cylinders are installed on a spring-damper system, allowing them to vibrate freely in the transverse direction. By comparing the aero-elastic responses of the wavy cylinder with that of a normal cylinder, the VIV suppression efficacy of the former is assessed. At last, we conclude the current thesis in Chapter 6. Some prospects for the use of wavy cylinder in engineering, as well as the prospects for future research, are also outlined.

1.4 Resulted publications

Based on the work described in this thesis, the following archival papers are accomplished.

- Zhang, K., Katsuchi, H., Zhou, D., Yamada, H. & Han, Z., Numerical study on the effect of shape modification to the flow around circular cylinders, *Journal of Wind Engineering and Industrial Aerodynamics*, 152(2016), pp. 23-40.
- Zhang, K., Katsuchi, H., Zhou, D., Yamada, H., He, T. & Lu, J., Large eddy simulation of flow over inclined wavy cylinders, *Journal of Fluids and Structures*, in review.
- Zhang, K., Katsuchi, H., Zhou, D., Yamada, H., Zhang, T. & Han, Z., Numerical simulation of vortex induced vibrations of a flexibly mounted wavy cylinder at subcritical Reynolds number, *Ocean Engineering*, 133(2017), pp. 170-181.
- Zhang, K., Katsuchi, H., Zhou, D. & Yamada, H., A numerical investigation on the flow around a wavy cylinder under forced vibration. (To be submitted)
- Zhang, K., Katsuchi, H., Zhou, D. & Yamada, H., On the fluid dynamics of flow past a wavy circular cylinder at low Reynolds numbers. (In preparation)

The work has also been, and will be presented in several international conferences, which are list below.

- Zhang, K., Katsuchi, H., Zhou, D. & Yamada, H., Numerical investigation of vortex induced vibration of wavy cylinders, 8th International Colloquium on Bluff Body Aerodynamics and Applications, Northeastern University, Boston, Massachusetts, USA, June 7-11, 2016.
- Zhang, K., Zhou, D., Katsuchi, H., & Yamada, H., Numerical study of vortex induced vibration of a cylinder with span-wise waviness, IASS2016 Annual International Symposium, Tokyo University, Tokyo, Japan, September 26-30, 2016.
- Zhang, K., Katsuchi, H., Yamada, H. & Zhou, D., On the fluid dynamics of circular cylinders with span-wise waviness, 7th European-African Conference on Wind Engineering, Liége, Belgium, July 4-7, 2017.

Chapter 2

Background and Literature Review

We present a background tour of the aspects that are associated with our current research topic by reviewing the related literature. Firstly, the general topics of flow around a circular cylinder, including a static cylinder, free vibration and forced vibration are introduced. Next, existing flow control approaches that are applicable to the management of cylinder cross flow are categorized into three groups based on the location where the method is applied to. The emphasis is put on the recently emerged 3D forcing technique.

2.1 Flow around a circular cylinder

Cylinder cross flow is among one of the most studied problems in the fluid mechanics. The meaning of this study is three fold. Firstly, circular cylinder serves as a prototype for many engineering applications, such as the bridge cable, overhead transmission line, drilling riser, chimney, high-rise building, etc. For designing purposes, it is imperative that the aero/hydro-dynamics associated with the circular cylinders be thoroughly understood. Secondly, it contains a kaleidoscope of fluid phenomenon such as the boundary layer separation, free shear layers, Kármán vortex shedding, etc. These problems are of great interest to the fluid dynamics community. Thirdly, owing to its simple configuration, the cylinder cross flow is often used as a benchmark case to validate a new numerical method. In the light of the abundant literature in this field, we propose to present a general overview of the flow around a cylinder in the current section. The discussions are not limited to the static cylinder, but also the vortex-induced vibration, also known as the free vibration, and the forced vibration.

2.1.1 Flow around a static cylinder

Flow regimes

The physics of the cylinder cross flow is constituted of three major parts, the boundary layer, the free shear layer, and the wake (Prasad and Williamson, 1997), the properties of which are mainly dependent on the Reynolds number

$$Re = \frac{U_\infty D}{\nu}, \tag{2.1}$$

in which D is the diameter of the cylinder, U_∞ is the flow velocity, and ν is the kinematic viscosity. The flow undergoes fundamental changes as the Reynolds number is varied. For very small Re values the boundary layer attaches to the cylinder surface and no separation occurs. In the range of $5 < Re < 47$, the boundary layer separates from the cylinder surface and a fixed pair of stationary vortices forms in the wake of the cylinder. When the Reynolds number is further increased, the wake becomes unstable, and is governed by the famous Kármán vortex shedding, in which vortices are shed alternatively

at either side of the cylinder at the Strouhal frequency. This also give rise to the periodic lift forces exerted on the cylinder. The vortex shedding maintains two-dimensionality for $Re < 180$, followed by a transition to three-dimensional flow owing to the span-wise instabilities at $200 < Re < 300$ (Williamson, 1988). With a further increment in Re, transition to turbulence occurs in the wake region (Bloor, 1964), where the vortices are shed in span-wise cells. Despite the turbulent wake for $Re > 300$, the boundary layer still remain laminar for a large range of Re, namely $300 < Re < 3 \times 10^5$. This regime is known as the subcritical flow regime. As for the free shear layer, the Kelvin-Helmholtz instability commences at around $Re \approx 1000$ (Bloor, 1964; Prasad and Williamson, 1997), which further complicates the flow. The subcritical flow prevails until around $Re \approx 3 \times 10^5$, and then the flow becomes critical, marked by a transition of laminar to turbulence in one side of the boundary layer. The drag force in the critical regime suffer from a significant drop, and reaches a minimum at $Re \approx 3.5 \times 10^5$. This is accompanied by the lose of symmetry, resulting in non-zero mean lift force on the cylinder (Schewe, 1983; Rodríguez et al., 2015; Lehmkuhl et al., 2014). The next Reynolds number regime is the named the supercritical flow regime, at which the drag recovers the wake symmetry is regained. This is because the laminar-turbulence transition occurs in both sides of the boundary layer. Further increasing the Re, the boundary layer becomes fully turbulent.

Vortex shedding

The most interesting feature associated the cylinder cross flow is the vortex shedding phenomenon, which occurs extensively over a large range of Reynolds numbers. Vortex shedding occurs as a result of the Hopf bifurcation of the absolute instability in the wake region (Monkewitz, 1988; Zebib, 1987; Jackson, 1987). A detailed description of the vortex shedding process has been put forward by Gerrard, 1966 and is briefly revisited here. As a result of the absolute instability, one of the vortex loop grows larger than the other for $Re > 47$. The smaller vortex, which is of the opposite sign of the larger vortex, constantly gets fed by vorticity from the free shear layers. It is drawn to the larger vortex, and at some point cuts off the vorticity supply from the free shear layer to the larger vortex, which is then shed as a free vortex. Then, the same process takes place in the other side and completes one vortex shedding cycle.

Aerodynamic responses

There are some important aerodynamic parameter in the cylinder cross flow, namely, the drag, lift and the vortex shedding frequency. Usually they are expressed in their non-dimensional forms as

$$C_d = \frac{2F_d}{\rho D U_\infty^2 L}, \tag{2.2}$$

$$C_l = \frac{2F_l}{\rho D U_\infty^2 L}, \tag{2.3}$$

$$St = \frac{fD}{U_\infty}, \tag{2.4}$$

in which C_d, C_l are the drag and lift coefficients, F_d and F_l are the drag and lift forces. L denotes the span-wise length of the cylinder. St is the famous Strouhal number which is a normalized representation of the vortex shedding frequency. The drag force acts in the streamwise direction on the cylinder and is a primary design concern for engineering applications as has been mentioned in section 1.2. In the subcritical regime the drag coefficient maintains a value of around 1 (Zdravkovich, 2003; Sumer and Fredsøe, 2006),

indicating that the drag force scales with the square of the velocity magnitude. On the other hand, there is no general consensus on the value of the lift coefficient (Norberg, 2003), since it is related to the vortex shedding along the span-wise direction, and the imperfect correlation of which may alter the lift force to a great extent. However, the frequency of the lift force, expressed by the Strouhal number, is quite stable and assumes a nearly constant value of around 0.2 in the subcritical regime. The Strouhal number is an important parameter since it allows us to assess the possibility of the related consequences of the vortex shedding, such as vortex induced vibration, noise, wake induced forces, and so on.

Cylinder inclined to incident stream

It is common occurrence that the natural flow attacks the structures from all possible angles. For a circular cylinder, the Cosine Rule, also known as the Independence Principle, has long been established to evaluate the aerodynamics when the flow is inclined to the cylinder axis at small angles. By considering the order of magnitude of terms for small viscosity, Sears (1948) showed that the axial dimension is uncoupled to the other two dimensions and could be safely removed from the laminar boundary layer equations, indicating that the flow maintains the same physics with that at zero yaw. Chiu et al. (1967) confirmed this theory by further developing Sear's method to resolve the equations for both the boundary layer and potential flow in the wake. The flow around a yawed cylinder has been subjected to extensive experimental researches (Hoerner, 1965; Hanson, 1966; Surry and Surry, 1967; Ramberg, 1983; Kozakiewicz, Fredsee, and Sumer, 1995; Zhou et al., 2009; Van Atta, 1968) ever since. It is now generally acknowledged that the validity of the Independence Principle could be expected as long as the inclination angle α is smaller than $40^\circ \sim 50^\circ$, where α is defined as the angle between the velocity vector itself and its component perpendicular to the cylinder axis. For larger α, deviation from the Cosine Rule commences. Worthy of mentioning is that the work of Ramberg (1983) noted that flow behind the inclined cylinder is very sensitive to the upstream end condition, since the flow generated by the end plate may contaminate the entire wake owing to the strong axial flow. The effect of the span-wise boundary conditions have also been studied numerically by Yeo and Jones (2008), in which the slip wall condition is revealed to affect the wake flow significantly while such effect is not observable in the case of periodic wall condition. To mimic an infinite cylinder that is free of end effect, the periodic boundary condition has been employed universally in the numerical researches (Zhao, Cheng, and Zhou, 2009; Zhao et al., 2013; Bourguet, Karniadakis, and Triantafyllou, 2015; Bourguet and Triantafyllou, 2016; Lucor and Karniadakis, 2003). In general these computational efforts have come to the similar conclusions as the experimental works regarding the validity of the Cosine Rule. Besides, they have provided further insights into the flow physics and enhanced our understanding to the flow around an inclined cylinder.

2.1.2 Vortex-induced vibration

The phenomenon

Vortex-induced vibrations of circular cylinders involve quite a number factors such as mass ratio, damping, stiffness, Reynolds number, incoming turbulence intensity, etc., the study of which has fostered voluminous publications that are based on various methods. Comprehensive reviews on theses subjects could be found in Sarpkaya (2004), Gabbai and Benaroya (2005), and Williamson and Govardhan (2004) and son on. The VIV phenomenon is generally featured by self-excited and self-limited oscillations over a range of

reduced velocities in which the vibration frequency locks to natural frequency of the system. The variation of vibration amplitude with respect to the reduced velocity could be fit into Feng's two branch (initial-lower) curve (Feng, 2011), or the three branch (initial-upper-lower) curve of (Khalak and Williamson, 1999) for lower mass-damping. Further more, Govardhan and Williamson (2000) and Govardhan and Williamson (2002) identified a critical mass ratio of around 0.54, below which the vortex induced vibration might occur for all the reduced velocities larger than 5. If the cylinder is allowed to vibrate in both the transverse and in-line directions, the "super-upper" branch, characterized by massive amplitude of 3 diameters peak-to-peak, is unveiled by Jauvtis and Williamson, 2004. These findings have important indications on the practical applications, especially the ocean engineering for which the mass ratio of the structure is usually small.

Intuitively, VIV would not be expected at the Reynolds numbers smaller than 47, at which the Kármán vortex shedding has yet to be triggered for a fixed cylinder. However, flow-induced vibrations has been reported to exist extensively at the subcritical conditions (Mittal and Singh, 2005; Étienne and Pelletier, 2012; Cossu and Morino, 2000). Free vibrations at the subcritical condition occurs over a specific range of reduced velocities, at which the frequency lock-in takes place for all cases. Outside this range, vibration does not develop and the flow remains static as with the case of a fixed cylinder. However, there do exist a lower threshold at $Re \approx 20$ (Mittal and Singh, 2005; Étienne and Pelletier, 2012), below which the VIV phenomenon does not appear. Recently, Kou et al. (2017) applied the dynamic mode decomposition technique to a initially perturbed cylinder wake field and found that the Kármán mode (we will explain this deeper in the next paragraph) vanishes at Reynolds numbers below 18, which precludes the interaction with the structural mode. This is though to be the lowest Reynolds number for the onset of VIV.

The mechanism

Despite the large body of literature on the free vibration of a cylinder in cross flow, there has been much less work on its mechanism. The way we name this vibration: vortex-induced vibration, leads us to believe that the mechanism is similar to the case of an oscillator of natural frequency f_N being forced by the periodic Kármán vortices f_{st}. As the natural frequency of the oscillator approaches the Strouhal frequency, i.e., $f_N \sim f_{st}$, resonance occurs and large amplitude oscillations take place.

However, as has been mentioned previously, free vibration of the circular cylinder are observed even at Reynolds number inferior to 47. This case resembles the classical causality dilemma of the chicken or the egg: does the vibration cause the vortex shedding? or vice versa?

Recently, linear stability analysis (Theofilis, 2011) was extended to the coupled fluid-structure system to shed light upon the mechanism of frequency lock-in phenomenon in vortex-induced vibration. Such kind of researches was firstly conducted by Cossu and Morino (2000), who identified two modes that may be responsible for the onset of instability in the fluid-structure system and referred to them as the nearly structural and von Kármán modes. The former mode corresponds, in the limit of very large mass ratio, to the eigenvalue of the cylinder-only system, and the latter mode is similar to leading eigenvalue that can be computed from the fixed cylinder cross flow. It was demonstrated that the critical Reynolds number for mass ratio smaller than 70 is less than half that of the stationary cylinder. De Langre (2006) employed the wake oscillator model to study the mechanism of the frequency lock-in phenomenon. By discarding the nonlinear terms in the van der pol equation and the damping term in the structural equation, he showed that the solution to this simplified wake oscillator model displays the merging of two

neutral modes, which resembles the coupled-mode flutter of the plunge-torsion instability of airfoils (Blevins, 1990). He further reasoned that the flutter in the current case occurs by coupling between the transverse displacement and the rotation of the position of the separation points on the cylinder. This novel interpretation has been substantiated by Zhang et al. (2015). They approached the linear stability eigenvalues by the construction of the ARX-based reduced order model for the wake, which is then coupled to the structural equation. It was shown that, depending on the eigenvalues of the two modes of interest, the mechanism of frequency lock-in at low Reynolds numbers could be divided into two categories, the 'resonance-induced' and the 'flutter-induced'. More recently, Navrose and Mittal (2016) solved the linearized coupled fluid-structure equations in the finite-element method. In addition to the very similar results obtained by the reduced order model of Zhang et al. (2015), mode shapes corresponding to the different stability regimes were given, owing to the FEM framework. Further, from the energy consideration they showed that only those unstable eigenmodes whose energy ratio (defined as the fraction of total energy of the eigenmode that is contained in the structure as kinetic and potential energy) is above a certain threshold value result in lock-in in the saturated state.

2.1.3 Forced vibration

Forced vibration tests has been useful in understanding the effect of body motion on the flow behavior. The most common configuration investigated so far is a circular cylinder being forced to oscillate harmonically in the cross-flow direction, although the effect of non-harmonic forcing (Konstantinidis and Bouris, 2016; Konstantinidis and Bouris, 2009), and in-line forcing (Konstantinidis, Balabani, and Yianneskis, 2003; Feymark et al., 2013) have also seen noticed. Such configurations allow to study the relative effects of amplitude and frequency of body motion on the flow, such as the wake synchronization, vortex patterns, fluid forces, etc. The result of the forced vibration has sometimes been used to predict the free vibration, usually through the consideration of energy transferred between the fluid and the structure (Kumar, Navrose, and Mittal, 2016; Morse and Williamson, 2009). In the current section, we will main go through the main aspects of the harmonic forcing in the cross-flow direction.

One of the most significant phenomenon found in the flow past an oscillating cylinder is the lock-in/synchronization, which occurs as the external forcing is applied in the vortex shedding frequency of a stationary cylinder. Similar to that in the free vibration, the lock-in region is featured by the vortex shedding frequency diverging from that corresponding to a fixed cylinder and becomes equal to the frequency of the cylinder oscillation. The extent of the frequency lock-in region has been demonstrated to be positively dependent on the vibration amplitude (Koopmann, 1967; Morse and Williamson, 2009; Kumar, Navrose, and Mittal, 2016; Anagnostopoulos, 2000). Outside the synchronization, i.e., the forcing frequency is away from the natural shedding frequency, the lift spectrum is characterized by two distinctive peaks, one at the forcing frequency, and the other near, but not necessarily equal to the vortex shedding frequency of a fixed cylinder. Another celebrated topic in the forced vibration is the determination of the various vortex shedding patterns. Williamson and Roshko (1988) experimentally investigated the flow over an oscillating cylinder with the Reynolds numbers ranging from 300 to 1000 and put forward the famous map in the wavelength-amplitude plane. Several shedding modes, such as the 2S (a single vortex is formed in each half oscillation cycle), 2P (two vortex pairs are shed per cycle), P+S (a vortex pair and a single vortex are shed in a vibration cycle), etc., have been identified. This shedding modes have also been observed in the free vibrations of circular cylinders. In addition, the aero/hydro-dynamic forces

undergo a magnification when the excitation frequency is close to the natural shedding frequency, and a sudden change in the phase angle between the lift force and cylinder displacement when the oscillation frequency is varied around the shedding frequency (Bishop and Hassan, 1964; Carberry, Sheridan, and Rockwell, 2001; Carberry, Sheridan, and Rockwell, 2005).

It is interesting to note that the forced oscillation at the lower Re front has also been visited by some researchers (Buffoni, 2003; Chen, Yen, and Wang, 2011; Jiang and Zheng, 2017). It has been shown that vortex shedding could be triggered at some specific combinations of the frequency and amplitude. Particularly, Jiang and Zheng (2017) noted that at such regime, the frequency of the lift force fluctuation always conforms to the external forcing. This differ significantly from that at higher Reynolds numbers, where there is usually two peaks in the lift force spectrum outside the lock-in region.

Another point worthy of noting is that with small-amplitude transverse cylinder oscillation and harmonic forcing frequency around 1.8 times the natural shedding frequency, the forced vibration could be used as a flow control method (Berger, 1967; Berger and Wille, 1972; Wehrmann, 1965; Schumm, Berger, and Monkewitz, 1994). For the sake of brevity this aspect will not be reviewed in detailed in the current thesis. Interested readers could refer to the publications cited herein.

2.2 Control of flow around bluff body

Flow control has been a discipline lying at the junction of several fields, such as civil, automobile, aeronautical, ocean, biology engineering. More often than not, flow control aims at the suppression of the undesired flow instabilities and the correlated forces, vibrations, noises, etc. However, recent innovative ideas has emerged to maximize the vibrations for the extraction of green energy such as VIVACE [1] (Park, Kumar, and Bernitsas, 2013; Kim, Bernitsas, and Kumar, 2013; Lee and Bernitsas, 2011) and vortex bladeless[2] (El-Shahat, 2016; Cajas et al., 2016). Previous investigations in this discipline have been fruitful in that not only a variety of methods have been proposed, but also some of the basic flow control mechanisms explained. A comprehensive summary was presented in the annual review by Choi, Jeon, and Kim (2008). Conventionally, the control methods could be classified into the passive, active open-loop and active closed-loop controls, in the sense that there is no power input, actuators with power input but no sensor, and sensors combined with actuators with power input, respectively. As we have mentioned in section 2.1.1, the flow around a circular cylinder is constituted from three essential parts, namely, the boundary layer, the free shear layer, and the wake. Flow control techniques of any possible form are applied directly, or indirectly, to either of these three regions to achieve desired goal. It is based on this idea that we propose to classify the flow control approaches into three main categories, which are the boundary layer control, the free shear layer control and the direct wake control. We will go through a detailed tour of these three classes in the following texts.

2.2.1 Boundary layer control

As far as a smooth circular cylinder is concerned, a laminar-to-turbulence transition takes place in the boundary layer at the critical Reynolds number ($Re \approx 3 \sim 5 \times 10^5$) and empowers the boundary layer with more momentum against the adverse pressure gradient, which delays the separation and ultimately engenders the *drag crisis*. The idea of making

[1] http://www.vortexhydroenergy.com/
[2] http://www.vortexbladeless.com/

the boundary layer turbulent to delay separation has bred several kinds of control methods such as surface roughness, dimples, axial grooves and ridges, polygon, etc. We put all these methods into the category of boundary layer control.

The effect of surface roughness to the aerodynamic forces has been investigated by a number of researches. Achenbach (1971) concluded from his wind tunnel experiments that the rougher the cylinder surface, the lower the value of the critical Reynolds number, but the smaller the fall in drag coefficient through the critical regime. He also showed that in the post-critical regime a cylinder with rough surface exhibits higher drag coefficient than the one whose surface is smooth. This statement is supported by Nakamura and Tomonari, 1982.

The role of the surface roughness is to disturb the original laminar flow in the smooth surface and make it turbulent. Within a certain range, the larger the roughness, the easier the transition takes place, and the earlier the *drag crisis* appears. However, for the roughness to be effective, high enough Reynolds number needs to be achieved. Besides, in the postcritical regime, the drag force recovers to a value that is higher than the smooth cylinder. In view of the above, surface roughness is only effective for a short range of Reynolds numbers. It is debatable whether it is of economical use to apply surface roughness to practical applications.

Golf ball travels far in the air, owing to its aerodynamically beneficial surface geometry, the dimples (Bearman, 1976). For the circular cylinder, dimples could also bring about favorable effects such as drag reduction. Actually, it is reported by Bearman and Harvey, 1993 that dimples are superior to the sand roughness since it produces smaller drag coefficient in the postcritical regime.

In a similar fashion, the axially carved grooves also help to reduce the drag force at certain Reynolds numbers. Kimura and Tsutahara (1991) employed both flow visualization and computational methods to study the effect of one groove or cavity placed at around $\theta \approx 80°$. This modification was proved to be effective in reducing the drag force. Similar investigation was conducted by Seo et al. (2013), who found out that 28.2% of drag force is reduced if 3 consecutive grooves were placed at certain orientation in the upwind side of cylinder. However, in practical applications arranging for the groove at the right angle is not easily accomplished, thus regular distribution of this kind groove should be engraved into the cylinder surface. This idea was materialized by Eguchi et al. (2002) in his water tunnel experiment on the newly developed overhead electric wire. In his paper, flow visualization was made to reveal that the shift of the separation point originates from an oscillatory phenomenon of a free shear layer in a groove opening on the wire surface around $70°$ from the stagnation point. The drag crisis of this kind of grooved cylinder commences at around $Re = 3 \times 10^4$ and in the post-critical regime C_d remained lower than the conventional transmission line. Ridged cylinders are also reported to have mitigated the drag force. Ridges as they may seem, they could also be regarded as grooves only the curvature inside is opposite. With this in mind, it is not difficult to conclude that the mechanism of drag reduction could also be categorized into the turbulent boundary layer generated by local separation. Matsumura et al. (2002) investigated the effect of numbers of ridges on the drag reduction and found out that the cylinder with 24 and 30 ridges promoted the drag crisis to a lower Reynolds number than the one with 16 ridges and 15% of drag was reduced.

2.2.2 Free shear layer control

According to Gerrard (1966), the Kármán vortex shedding is sustained by the concentrated vorticity in the free shear layers. It follows that flow control could be achieved if this vorticity supplement mechanism could be inhibited or disturbed. From what we

have learned in the literature, there are at least three sub-classifications which fit the essence of this category, which are detailed below.

Obstacles in the shear layer regions

The technique, proposed by Strykowski and Sreenivasan (1990), involves introducing a smaller control rod within a defined region in the downstream of the cylinder. The most effective region for the suppression of the vortex shedding locates at the shear layer bordering the mean recirculation bubble. In this way, the development of the free shear layer and its access to supplying the primary vortices are obstructed. From a more theoretical perspective, the same authors have shown numerically that the experimentally observes suppression of vortex shedding corresponds to a globally damped wake. It is likely that it is primarily the breaking of the mean flow symmetry which is responsible for the reduction of absolute instability.

A similar approach is adopted by Shao and Wang (2007) and Shao and Wei (2008) to a rectangular cylinder at higher Reynolds numbers. They've shown that vortex shedding from both sides of the cylinder could be suppressed if the element size is greater than a critical value. Besides, a phenomenon of monoside vortex shedding is observed that could not be readily explained by Gerrard (1966)'s model of vortex generation. This observation presents an interest to the fluid mechanics community and is worth deeper investigations.

Stabilization of the free shear layers

The 3D forcing technique has recently gain popularity among the fluid control community owing to its extraordinary efficiency. This approach aims to enhance the resilience of the free shear layers against the rolling-up of the Kármán vortices by introducing three dimensional modifications onto the originally two dimensional base flow.

Perhaps the mostly well-known approach pertaining to this category is the distributed span-wise forcing proposed by Kim and Choi (2005). In this effort, distributed blowing and suction from two slots located at the upper and lower surface is applied to the circular cylinder in axial direction. It was revealed that the in-phase forcing could produce the phase mismatch along the span-wise direction in vortex shedding, weakens the strength of vortical structures in the wake and thus reduces the drag. At the optimal forcing wavelength of $\lambda_z = 5D$ (where D is the diameter of the cylinder), maximum drag reduction, accompanied by total suppression of the vortex shedding at $Re = 100$ could be obtained with the forcing amplitude $\Phi \geq 0.08u_\infty$ (u_∞ is the free-stream velocity), which is much smaller than the other forcing method such as the base bleed (Schumm, Berger, and Monkewitz, 1994). Hwang, Kim, and Choi (2013) shed light upon the mechanism of this method by the use of linear stability analysis to a simplified wake model. In the phenomenological sense, it is explained that the stabilization by the span-wise waviness is due to the formation of the streamwise vortices and its interaction with the tilted Kármán vortex street. From a more theoretical perspective, the span-wise waviness is shown to result in enhanced stability than the two dimensional wake.

The above mechanism could also be achieved in a passive fashion by introducing geometrical span-wise wavy module into the two dimensional bodies. Examples include the wavy trailing edge on a blunt-base model (Tombazis and Bearman, 1997), wavy frontal stagnation face of a rectangular cylinder (Bearman and OWen, 1998), cylinder with wavy axis (Owen, Bearman, and Szewczyk, 2001), and, the cylinder with sinusoidally varying diameter (Ahmed and Bays-Muchmore, 1992; Ahmed, Khan, and Bays-Muchmore,

1993; Lam and Lin, 2009), as is shown in Fig. 1.4. The cross flow of the wavy circular cylinder has been subjected to intensive investigations for the past three decades. Early experimental investigations by Ahmed and Bays-Muchmore (1992) identified the significant span-wise pressure gradient on the cylinder surface, which results in greater sectional drag coefficients at the geometric nodes than the saddles. Ahmed, Khan, and Bays-Muchmore (1993) further looked into the turbulent wake behind a wavy cylinder. The separation line of the boundary layer was found to be span-wisely undulated, which subsequently leads to the three-dimensional development of the turbulent wake. Lam et al. (2004) started to focus on the aerodynamic force reduction of the wavy cylinders. They found out that significant drag and lift force reduction can be obtained in the subcritical Reynolds numbers range of $20000 \sim 50000$ provided that the wavelength ratio lies between 1.45 and 2.27. Furthermore, Lam, Wang, and So (2004) experimentally studied the velocity field and flow patterns in the near wake of a wavy cylinder. It was found out that the vortex formation length of the wavy cylinder is longer than that of the circular cylinder, and at the nodal and saddle planes, the stream-wise velocity distributions are very different compared with those of the circular cylinder. Zhang and Lee (2005) used the PIV technique to investigate the flow structures in the near wake of wavy cylinder and demonstrated well-organized stream-wise vortices in the span-wise direction, and these stream-wise vortices are believed to suppress the formation of the large-scale span-wise vortices and decrease the turbulent kinetic energy in the wavy cylinder wake. Lee and Nguyen (2007) measured the forces on wavy cylinders with different geometric parameters and found the maximum drag reduction of up to 22% compared with the normal circular cylinder. They also showed that the drag reduction seems to be related to the longer vortex formation region. Numerical simulations have also been helpful in interpreting the experimental observations about the wavy cylinder aerodynamics. By large eddy simulation, the cross flow around wavy cylinders of wavelength from 1.136 to 3.333 was studied by Lam and Lin (2008) at $Re = 3000$. Various aspects, such as drag and lift force reduction, longer vortex formation length, three-dimensional wake flow structures, etc., were confirmed. Lam and Lin (2009) subsequently conducted a systematic study on the effect of wavelength and amplitude of a wavy cylinder in the cross flow at low Reynolds numbers. It was revealed that the wavelength plays the dominant role in determining whether a wavy cylinder is capable of drag mitigation while the wave amplitude decides the extent of the reduction. Two values of optimal wavelength were detected, i.e., $\lambda/D_m \approx 2$ and 6, and at the optimized wavelength, the Kármán vortices could be completely annihilated given appropriate wave amplitude. Besides, the Reynolds number was also found to be important in the effectiveness of the flow control. The control efficacy of the wavy cylinder with large wavelengths ($\lambda/D_m \simeq 6$) at the turbulent regime has been further justified by numerical investigations of Lam et al. (2010) and more recently by Lin et al. (2016).

More recently, the twisted cylinder, which is designed by rotating the elliptic cross-section along the span-wise direction, has been studied by Jung and Yoon (2014) with numerical simulations. It has been revealed that the separated free shear layers are relatively more stable, and then roll up into vortices further downstream. As a result, the twisted cylinder is able to achieve reductions in the mean drag of approximately 13 and 5% compared with the results for smooth and wavy cylinders, respectively. A parametric study on the aspect ratio and wavelength of the twisted cylinder was conducted at $Re = 100$ by Kim, Lee, and Choi (2016), revealing not only the optimal geometry for drag reduction, but also a detailed classification of the wake modes. It was concluded that the twisted cylinder produces alternating vortex shedding in the span-wise direction, which weakens the strength of the Kármán vortices and reduces the mean drag and lift fluctuations. These two investigations show that the twisted cylinder controls the flow in a

similar fashion with the span-wise waviness as described above. However, we suggest that its resemblance with the straked cylinder, which will be reviewed in the next section, might be overlooked.

The geometric modification by O-rings attached on the cylinder, as has been proposed by Nakamura and Igarashi, 2008; Nakamura, 2011, should also be classified as a method that stabilizes the free shear layer. In this case, the span-wise protrusion by the large O-rings induces significant transverse vortices in the near wake, which obstruct the formation of the axial Kármán vortex shedding. This mechanism is very similar to that of the wavy cylinder, in which the obstruction of the span-wise vortices is achieved by the streamwise vortices.

Disruption of span-wise coherence

Different from the span-wise periodic waviness that stabilizes the free shear layers and the wake, another kind of 3D forcing methods aims at interrupting the span-wise correlation of the vortex shedding, which produces out-of-phase sectional lift forces that partially cancel each other.

Zhou et al. (2011) investigated a rigid circular cylinder with three-dimensional helical strakes of $10D$ in pitch and $0.12D$ in height at $Re = 10000 \sim 40000$ and found a 98% suppression of the vortex-induced vibration. It was observed in this experiment that the smaller-scale vortices in the free shear layer behind the straked cylinder decay quickly in the stream-wise direction and do not roll up to form the well-organized Kármán vortex. Also, a study of the span-wise correlation in the above paper showed that the correlation length of the vortical structures in the straked cylinder is only about $1/8$ of the bare one. Numerically, Constantinides and Oakley (2006) conducted a DES study on the flow past a straked cylinder ($0.25D$ in height and $15D$ in pitch) at Reynolds number of 6×10^5. Flow visualization showed that the strakes could control the separation of the flow effectively. The separation point was found to be at the tip of the strakes for most of the coverage of the surface and this observation is responsible for the three dimensional flow that breaks the vortex coherence. One drawback of such method is that the strakes usually lead to significant drag increase, which cause detrimental effect to the performance of the deepwater risers.

Helical wires are smaller in height but when attached to the cylinder, they could also serve to control the wake flow. Nebres and Batill (1992) experimentally performed investigations on a circular cylinders helically wrapped with 4 wires. By plotting the surface pressure distribution at various span-wise locations it was revealed that the helical protrusions established a periodic span-wise variation in the separation of the boundary layer, which consequently resulted in an elongated vortex formation length.

2.2.3 Wake modification

One of the most famous direct wake control methods is the wake splitter plate. Early experimentally studies conducted by Roshko, 1954a; Roshko, 1955 showed that an attached plate in the cylinder wake could modify the vortical structures and delay the interaction of the free shear layers. As a result, the base pressure increases and the reduction of the drag is achieved. More detailed investigations of such a configuration have explored the effect of the length , attachment/detachment, Reynolds numbers, etc. (Bearman, 1965; Gerrard, 1966; Apelt, West, and Szewczyk, 1973; Apelt and West, 1975; Nakamura, 1996; Kwon and Choi, 1996; Anderson and Szewczyk, 1997; Ozono, 1999; Bao and Tao, 2013a; Bao and Tao, 2013b). In a study of the dry galloping of the bridge cable, Matsumoto et al. (2010) used the perforated splitter plates to mimic the suppression effect of the axial flow

to the Kármán vortex shedding. It was revealed that while the vortex shedding in the stationary case could be mitigated, the placement of the splitter plate could lead to the divergent-type galloping. Such a mechanism could also be achieved through the active control such as the base bleed, in which flow is blown out from the cylinder base into the wake region (Wood, 1964; Bearman, 1967). From the perspective of local stability properties, Schumm, Berger, and Monkewitz (1994) explained that the absolute instability in the near wake is reduced very effectively by reducing or eliminating the reverse flow.

Chapter 3

Methods

Computational Fluid Dynamics, abbreviated as CFD, is leveraged to unveil the aerodynamics associated with the cross flow of the wavy cylinders. Since we are looking for the detailed mechanisms of the flow mechanisms at a relatively high Reynolds number, large eddy simulation is adopted for the current work. The governing equations, discretization schemes, the solution algorithms will be briefly introduced in this chapter.

3.1 The governing equations for fluids

The LES equations are derived from the classical time-dependent filtered incompressible Navier-Stokes equation:

$$\frac{\partial \overline{u}_i}{\partial x_i} = 0 \tag{3.1}$$

$$\frac{\partial \overline{u}_i}{\partial t} + \frac{\partial \overline{u}_i \overline{u}_j}{\partial x_j} = -\frac{1}{\rho}\frac{\partial \overline{p}}{\partial x_i} + \frac{\partial}{\partial x_j}\left[\nu\left(\frac{\partial \overline{u}_i}{\partial x_j} + \frac{\partial \overline{u}_j}{\partial x_i}\right) + \tau_{ij}\right] \tag{3.2}$$

$$\tau_{ij} = \overline{u_i u_j} - \overline{u}_i \overline{u}_j \tag{3.3}$$

where ν is the kinematic viscosity, $\overline{u}$ and $\overline{p}$ are the filtered velocity and pressure respectively. Eq. 3.3 is termed the sub-grid scale(SGS) stress which requires modeling. The SGS stress τ_{ij} is expressed according to the Boussinesq approximation with the introduction of a turbulent eddy viscosity ν_t:

$$\tau_{ij} - \frac{2}{3}k_t\delta_{ij} = -2\nu_t \overline{S}_{ij} \tag{3.4}$$

$$\overline{S}_{ij} = \frac{1}{2}\left(\frac{\partial \overline{u}_i}{\partial x_j} + \frac{\partial \overline{u}_j}{\partial x_i}\right) \tag{3.5}$$

in which $k_t = \tau_{kk}/2$ is the SGS turbulent kinetic energy and $\overline{S}_{ij}$ is the rate of strain tensor computed directly from the resolved scales.

Methods differ in the modeling of the turbulent eddy viscosity ν_t (Fureby et al., 1997). Lysenko, Ertesvåg, and Rian (2012) compared the performance of the Smagorinsky SGS model with the dynamic k-equation model in the open-source CFD software OpenFOAM. Although the results of both models had experimental data backed on, we found that the results obtained by the latter more convincing. In the current work the dynamic k-equation model is adopted. Instead of assuming the local equilibrium of the production and dissipation of the sub-grid turbulent energy, as is done in the Smagorinsky model (Smagorinsky, 1963), in dynamic k-equation model (Fureby et al., 1997) an exact balance equation for k_t is derived:

$$\frac{\partial k_t}{\partial t} + \frac{\partial}{\partial x_j}\left(\overline{u}_j k_t\right) = P + \frac{\partial}{\partial x_j}\left[\left(\nu + \nu_t\right)\frac{\partial k_t}{\partial x_j}\right] - \epsilon \tag{3.6}$$

$$P = 2\nu_t \overline{S}_{ij}\overline{S}_{ij}, \epsilon = C_\epsilon k_t^{1.5}\Delta^{-1} \tag{3.7}$$

where the SGS viscosity is given by $\nu_t = C_k \Delta k_t^{0.5}$. The model coefficients C_ϵ and C_k are dynamically computed as part of the solution based on the Germano identity (Germano et al., 1991) with test filter $\widehat{\Delta} = 2\Delta$ by the least square minimization procedure proposed by Lilly (1992).

3.2 Discretization

The aim of discretization is to transform the continuous governing equations to a set of discrete algebraic expression that is solvable by certain direct or iterative methods. Two parts constitutes this procedure: the discretization of the solution domain and the equations.

For the spatial domain discretization, OpenFOAM adopts the methodology of Finite Volume Method (FVM). In this approach the solution domain is divided into a finite number of regions called control volumes (CV). The control volumes do not overlap and completely fill the computational domain. In the case of transient problems, time should also be discretized. Usually a prescribed size of time-step is specified throughout the calculation.

As for the equation discretization, the generalized form Gauss theorem is used. Consider a generic form of transport equation for a scalar property ϕ,

$$\frac{\partial \phi}{\partial t} + \nabla \cdot (\mathbf{U}\phi) - \nabla \cdot (\gamma \nabla \phi) = S(\phi). \tag{3.8}$$

Integration of Equation 3.8 over a certain control volume V_P and time-step Δt gives

$$\int_{\Delta t}\left[\frac{\partial}{\partial t}\int_{V_P}\phi dV + \int_{V_P}\nabla\cdot(\mathbf{U}\phi)\,dV - \int_{V_P}\nabla\cdot(\gamma\nabla\phi)\,dV\right]dt = \int_{\Delta t}\int_{V_P} S(\phi)\,dV\,dt, \tag{3.9}$$

in which U indicates the velocity vector and $S(\phi)$ is the source term. The convection term is discretized by Equation 3.10.

$$\begin{aligned}\int_{V_p}\nabla\cdot(\mathbf{U}\phi)\,dV &= \sum_f \mathbf{S}\cdot(\mathbf{U}\phi)_f \\ &= \sum_f \mathbf{F}\cdot\phi_f,\end{aligned} \tag{3.10}$$

where $\mathbf{S}$ is the surface area vector, $\mathbf{F}$ is the mass flux through each of the surface surrounding the CV and this value requires special treatment, as will be elaborated in the next chapter. ϕ_f is the variable value on the surface center, which is obtained using certain convection differencing scheme. In current simulations, *Gauss limitedLiner*, one of the TVD(Total Variation Diminishing) schemes is employed for the convection differencing. The details of this scheme will not be presented here, interested reader are asked to refer to related literatures (Versteeg and Malalasekera, 2007).

The diffusion term is treated in a similar way as the convection, specifically,

$$\begin{aligned}\int_{V_p}\nabla\cdot(\Gamma\nabla\phi)\,dV &= \sum_f \mathbf{S}\cdot(\Gamma\nabla\phi)_f \\ &= \sum_f \Gamma\mathbf{S}\cdot(\nabla\phi)_f.\end{aligned} \tag{3.11}$$

$(\nabla\phi)_f$ is obtained by the gradient scheme specified in the *fvschemes* file and in the current case it is selected to be *Gauss linear*. What's worth attention here is the orthogonality between **S** and $(\nabla\phi)_f$, which originates from the orthogonality of the mesh. Special care should be taken to account for this problem. Some correction approaches are provided in Jasak (1996).

The source term is discretized in Equation 3.12.

$$\int_{V_p} \mathbf{S}(\phi)\, dV = \mathbf{S}_P V_P. \tag{3.12}$$

Equation 3.10 to 3.12 could be substituted into Equation **??** to obtain the semi-discretized form of transport equationHirsch (1990).

The last discretization is performed for the time. In this thesis *backward* scheme, which is of second-order and implicit, is used. It takes the form as Equation 3.13.

$$\frac{\partial\phi}{\partial t} = \frac{\frac{3}{2}\phi^n - 2\phi^o + \frac{1}{2}\phi^{oo}}{\Delta t}, \tag{3.13}$$

where ϕ^n is the variable value at new time, ϕ^o and ϕ^{oo} are the old and second old" times, respectively.

Up to now, the whole discretization process is finished, resulting in the fully discretized transport equation as shown in Equation 3.14

$$\frac{\frac{3}{2}\phi^n - 2\phi^o + \frac{1}{2}\phi^{oo}}{\Delta t} V_P + \sum_f \mathbf{F}\phi_f^n - \sum_f \Gamma\mathbf{S}\cdot(\nabla\phi)_f^n = \mathbf{S}_P V_P. \tag{3.14}$$

3.3 The Solution Procedure

In the absence of other source term, the flow is driven by the pressure gradient as is shown in Equation 3.2, for which no independent evolution exists. This, together with the non-linearity and the couple of the mass and momentum conservation equations, complicates the solution of the N-S equation.

Substitute ϕ with **U** in Equation 3.10 gives the non-linear term $\nabla\cdot(\mathbf{UU})$, which means velocity being transported by itself. Prohibited by the complexity of and large computational resource required by the non-linear solver, this term is conventionally linearized to facilitate computation.

The non-linear term is discretized in Equation 3.15.

$$\begin{aligned}\int_{V_P} \nabla\cdot(\mathbf{UU})\, dV &= \sum_f \mathbf{S}\cdot\mathbf{U}_f\mathbf{U}_f \\ &= \sum_f \mathbf{F}\mathbf{U}_f \\ &= a_P\mathbf{U}_P + \sum_N a_N\mathbf{U}_N.\end{aligned} \tag{3.15}$$

where the subscript N denotes the neighboring CV center. a_P and a_Ns are a function of **U**. Linearisation of the convection term implies that an existing velocity(flux) field that satisfies the continuity Equation 3.2 will be used to calculate a_P and a_Ns.

Equation 3.14 could be reconstructed to take the following form:

$$a_P\mathbf{U}_P = \mathbf{H}(\mathbf{U}) - \nabla p, \tag{3.16}$$

where $\mathbf{H}(\mathbf{U})$ consists of the source part of the transient term and the contribution of the convection and diffusion from the neighboring CVs, *i.e.*,

$$\mathbf{H}(\mathbf{U}) = -\sum_N a_N \mathbf{U}_N + \frac{\mathbf{U}^o}{\Delta t}. \tag{3.17}$$

Take the divergence of Equation 3.16 and noting the continuity Equation **??** we obtain

$$\nabla \cdot \left(\frac{1}{a_P} \nabla p \right) = \nabla \cdot \left(\frac{\mathbf{H}(\mathbf{U})}{a_P} \right). \tag{3.18}$$

Integration of the above equation over a CV gives

$$\sum_f \mathbf{S} \cdot \left[\left(\frac{1}{a_P} \right)_f (\nabla p)_f \right] = \sum_f \mathbf{S} \cdot \left(\frac{\mathbf{H}(\mathbf{U})}{a_P} \right)_f. \tag{3.19}$$

Equation 3.19 together with 3.16 are the final form of the discretised incompressible Navier-Stokes system.

Besides, the surface flux we have mentioned in the previous section is calculated using Equation 3.20.

$$\mathbf{F} = \mathbf{S} \cdot \mathbf{U}_f = \mathbf{S} \cdot \left[\left(\frac{\mathbf{H}(\mathbf{U})}{a_P} \right)_f - \left(\frac{1}{a_P} \right)_f (\nabla p)_f \right] \tag{3.20}$$

We are now in position to move to the solution procedure of the discretized N-S equations. The solver used in this thesis is *pimpleFoam*, which is a variant of the famous PISO(Pressure Implicit with Splitting of Operator) algorithm. The main procedure of the PISO algorithm could be summed up as follows Jasak (1996):

1. Set up the boundary conditions;
2. Solve the discretized momentum Equation 3.16 to compute an intermediate velocity field;
3. Compute the mass fluxes at the cell faces using Equation 3.20;
4. Solve the pressure Equation 3.19;
5. Correct the mass fluxes at the cell faces using Equation 3.20;
6. Correct the velocities on the basis of the new pressure field;
7. Update the boundary conditions;
8. Increase the time-step and repeat from 1.

The PIMPLE algorithm differs from the conventional PISO in the number of the prescribed iterations of the above PISO procedure. The main part of the source code in the *pimpleFoam.C* reads

```
Info<< "Time = " << runTime.timeName() << nl << endl;
// --- Pressure-velocity PIMPLE corrector loop
while (pimple.loop())
{
#include "UEqn.H"
```

```
// --- Pressure corrector loop
while (pimple.correct())
{
#include "pEqn.H"
}
if (pimple.turbCorr())
{
turbulence->correct();
}
}
```

Two parameters control the above algorithm, *nOuterCorrectors* specifies the number of the outer-iteration, *i.e.*, the PISO algorithm. *nCorrectors* specifies the number of pressure corrections inside the PISO algorithm. These two parameters are specified in the *fvSolution*. Here we set *nOuterCorrectors* to be 3 and *nCorrectors* to be 2. This setting is proved to yield stable and accurate results when a larger time-step is used, as will be discussed in Appendix A.

3.4 Matrix Solvers

The N-S equations are discretized by the procedures described in the previous section, resulting in a system of algebraic system. While the direct methods like Gauss elimination, LU decomposition are theoretically applicable to any matrix, in most CFD applications iterative methods are employed since they are more efficient.

In the present thesis, the *GAMG* solver, abbreviated for generalised geometric-algebraic multi-grid solver, together with Gauss-Seidel smoother is used for the pressure equation, and *PBiCG*, preconditioned bi-conjugate gradient solver for asymmetric matrices was used to solve velocity and k equations. A detailed elaboration of these methods would be lengthy and beyond the scope of the current thesis, thus only brief introduction will be presented here.

3.4.1 Multi-grid Methods

Iterative methods such as Gauss-Seidel produce errors that fails to be reduced after a few number of iterations. This problem is more prominent in the refined mesh. A close inspection of this behavior reveals that the convergence rate is a function of the wave-length of the error. While smaller wave-lengths counterparts are smoothed using the fine mesh, the longer ones are left behind. It is these long wave-length components that are retarding a fast convergence.

The multi-grid algorithm is designed to solve all wave-length components of the error and provides rapid convergence rate. The multi-grid strategy combines two complementary schemes. The high-frequency components of the error are reduced applying the Gauss-Seidel methods at fine grid level. For this reason this method is called smoother. On the other hand, low-frequency error components are effectively reduced by a coarse-grid correction procedure. Because the action of a smoothing iteration leaves only smooth error components, it is possible to represent them as the solution of an appropriate coarser system. Once this coarser problem is solved, its solution is interpolated back to the fine grid to correct the fine grid approximation for its low-frequency errors.

3.4.2 Conjugated Gradient Methods

The conjugated gradient method is one of the most popular iterative techniques for solving sparse symmetric positive definite systems of linear equations. Shewchuk (1994)'s textbook gives comprehensive explanation to this method, which we will summarize below.

Noticing that a linear system of equations $\mathbf{A}x = b$ could be transformed into a minimization problem of the quadratic function $\phi(x) = \frac{1}{2}x^T\mathbf{A}x - x^Tb$. By linear search methods as an iterative approach the solution at each iteration could be expressed as

$$x_{k+1} = x_k + \alpha_k p_k.$$

One way to construct the α_k and p_k is the steepest descent method, which, however, is slow in convergence because of its zigzag movement. The other way, as is the main topic of this subsection, is the conjugated gradient method.

For a matrix $\mathbf{A}$ that is symmetric and positive definite, the set of nonzero vectors

$$\{p_0, p_1, \ldots, p_{n-1}\}$$

is termed to possess *A-conjugacy* if it satisfies

$$p_i^T\mathbf{A}p_j = 0 \quad \forall i \neq j.$$

Such vectors are linearly independent and hence form the basis of the space $\mathbf{R}$ defined by the matrix $\mathbf{A}$. Thus we can express the difference between the exact solution x^* and the first guess x_0 as a linear combination of the conjugate vectors:

$$x^* - x_0 = \alpha_0 p_0 + \alpha_1 p_1 + \ldots + \alpha_{n-1} p_{n-1}.$$

These vectors are reduced each at an iteration, *i.e.*, at step k, x_k is the exact solution of x^* projected into the solution space spanned by the k vectors. After n steps, the error initial error vector diminishes and the the exact solution is sought.

Work remains is to find the conjugated vectors p_k and their corresponding α_k. It is found that the new conjugate vector p_k could be obtained using only the previous vector p_{k-1} and the negative residual $-r_k$, *i.e.*,

$$p_k = -r_k + \beta_k p_{k-1},$$

where β_k is given as

$$\beta_k = \frac{r_k^T r_k}{r_{k-1}^T r_{k-1}}.$$

3.5 Equation of motion for the structure and FSI algorithm

The motion of the rigid cylinder body is governed by:

$$m\frac{d^2Y}{dt^2} + c\frac{dY}{dt} + kY = F_Y, \tag{3.21}$$

where Y denotes the transverse displacement of the cylinder, m, c and k are the structural mass, damping and stiffness, respectively. F_Y represents the lift force in the cross-flow direction and is calculated by integrating the pressure and wall shear forces over the whole cylinder surface. The *sixDoFRigidBodyMotion*, an OpenFOAM built-in solver developed

in the spirit of Dullweber, Leimkuhler, and McLachlan (1997), is employed to integrate Eq. 3.21. The coupled fluid-structural problem are solved through a partitioned, weakly-coupled algorithm in which the two subsystems advance in a staggered fashion, as is depicted in Fig. 3.1. The structure solver is invoked at the beginning of each time step, the output of which drives the motion of the mesh and serves as the boundary condition for the fluid solver. As has been discussed by He, Zhou, and Bao (2012), He et al. (2014), and He (2015), in contrast to the strong coupling scheme, the weak coupling technique has the advantage of being less computational intensive. However, it does not assure the exact satisfaction of the equilibrium on the fluid-structure interface so that the cumulated errors may lead to a spurious solution or even a failure. This problem is frequently encountered in the case of small mass ratio and strong added mass effect. However, considering that for the current problem, the weakly-coupled algorithm has been reported to yield robust FSI results (Bao, Zhou, and Tu, 2011; Placzek, Sigrist, and Hamdouni, 2009; Tu et al., 2014), we decided to stick with the current scheme. In order to alleviate the numerical instability initiated from the time-lag effect, we choose a small enough time-step based on the mesh dependency test, which will be presented in Appendix A.

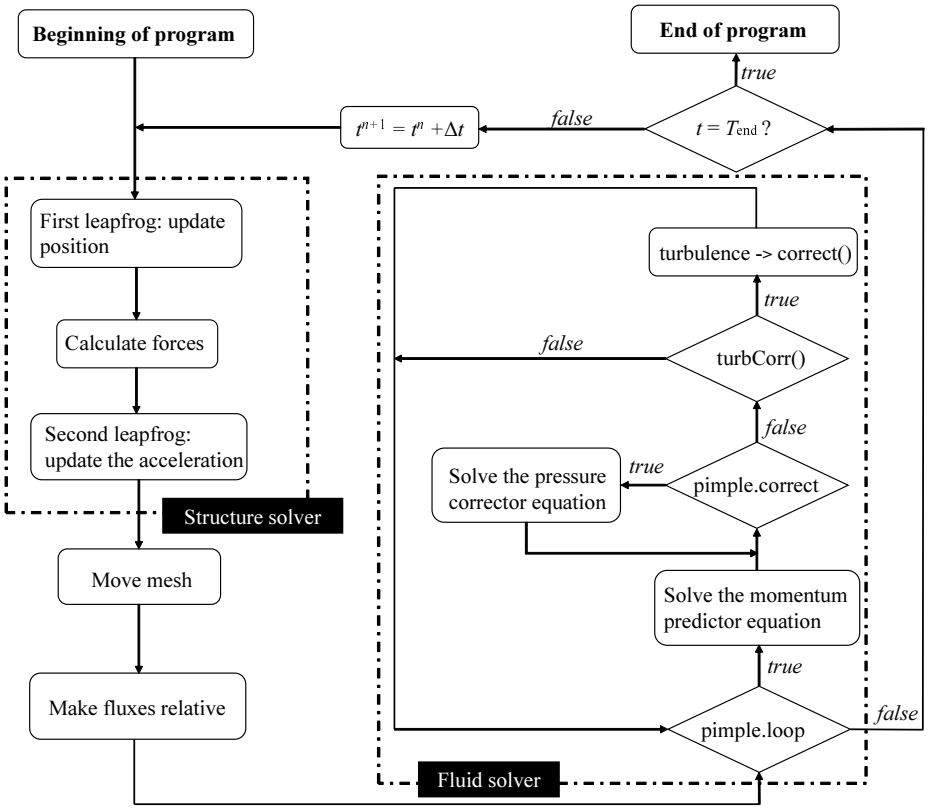

FIGURE 3.1: Algorithm of the solution procedure

Chapter 4

Inclined Wavy Cylinder in the Fixed Configuration

4.1 Case setup

As has been reviewed in section 2.2, the cross flow around a fixed wavy cylinder has been subjected to intensive researches. Also, the flow around an inclined normal cylinder is also generally understood. However, when it comes to the inclined flow over a wavy cylinder, much less information has been acquired so far. The only reference on this aspect is the work of Lam et al. (2010). It was found out that although the mean drag and the fluctuating lift coefficients of a yawed wavy cylinder are less than those of a correspondingly yawed circular cylinder at the same flow condition, the independence principle is not no longer suitable for the inclined wavy cylinders, and with the increase of the yaw angle, the advantageous effect of wavy cylinder on force mitigation becomes insignificant. However, their discussion was limited to only one wavy shape, which makes it difficult to form a conclusive view on the current topic. It is based on this consideration that we embark upon a detailed investigation on the aerodynamics of the inclined flow around a wavy cylinder.

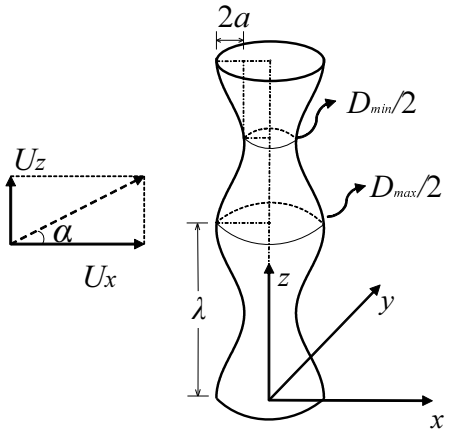

FIGURE 4.1: Schematic of the wavy cylinder subjected to inclined incident stream

A schematic view of the current problem is sketched in Fig. 4.1. The diameter of the wavy cylinder is corrugated by the wavelength λ and the amplitude a through the following relationship:

$$D_{(z)} = D_m + 2a\cos\left(2\pi z/\lambda\right), \tag{4.1}$$

in which D_m is the averaged diameter. The axial locations at which the diameter maximizes (D_{max}) and minimizes (D_{min}) are referred to as 'node' and 'saddle', respectively. Based on the literature survey in Chapter 2, two wavelengths, $\lambda/D_m = 2$ and 6, each with amplitude $a/D_m = 0.1$ and 0.15, are considered in this work. To facilitate our discussion, abbreviations like 2_0.1, which stand for the wavy cylinder with $\lambda/D_m = 2$ and $a/D_m = 0.1$, are used throughout the following text. In order to accommodate more of the three-dimensional flow features, the length of the cylinders are designed to be relatively long: $L = 18D_m$ and $16D_m$ for the $\lambda/D_m = 6$ and 2 cases respectively. The cylinder is subjected the flow with uniform velocity $U = (U_x, 0, U_z)$. In the current work, the stream-wise velocity U_x is kept fixed while the span-wise velocity U_z is varied to yield three different values of inclined angle $\alpha = 0°, 30°$ and $45°$. The Reynolds number is defined based on the characteristic diameter D_m, the stream-wise velocity component U_x and the kinematic viscosity μ, i.e., $Re = D_m U_x/\mu$, and is kept constant at 5000. Simulations with the same setup and parameters are also conducted for the normal circular cylinder to serve as the basis based on which the aerodynamic performance of the wavy cylinders could be evaluated. The length of the normal circular cylinder is also taken to be $16D$.

The cylinder is placed in the center of a circular computation domain, which has a radial extension of $20D_m$. The curvilinear O-type mesh is used with $N_c \times N_r = 180 \times 180$ grids in the cross section (N_c and N_r refer to the number of grids in the circumferential and radial directions, respectively). The radial grid points are clustered in the vicinity of the cylinder with an expansion factor of 1.035 in avoidance of abrupt change of the grid size, and the first grid is placed at around $1.4 \times 10^{-3}D$ away from the cylinder wall. 250 and 280 grids are prescribed in the span-wise direction for the $L = 16D_m$ and $18D_m$ cases, respectively. The total number of control volumes thusly mounts up to around 9×10^6. The non-dimensional time-step is fixed at 0.01. The current mesh resolution is chosen after the mesh dependency test, as will be presented in the next section. The inlet boundary is assigned with a constant velocity $U = (U_x, 0, U_z)$. Periodicity is enforced in the span-wise direction of the cylinder. At the outlet boundary the reference pressure $p_\infty = 0$ is specified. The cylinder wall is set to be no-slip.

4.2 Force coefficients

A summary of the mean drag, rms lift force coefficients and the Strouhal numbers as a function of α is presented in Fig. 4.2. The results from Lam et al. (2010) at $Re_\infty = 3900$ (Re_∞ indicates that the velocity magnitude U_∞ is used rather than the normal component) for the inclined normal and 6_0.15 wavy cylinders, and Aljure et al. (2017) at $Re = 5000$ for the normal cylinder only are also included for comparison. For the normal cylinder at $\alpha = 0°$, Aljure et al. (2017) obtained $C_l' = 0.156$, while in the current paper a much smaller value of 0.073 is achieved. It should be noted that in our previous work (Zhang et al., 2016), where the same numerical setup as this work has been employed to studied a circular cylinder with spanwise length of $L_z = 6.28D$, the rms lift coefficient is around 0.147, which is closer to the work of Aljure et al. (2017). According to Norberg (2003), since the lift force on the circular cylinder is not perfectly correlated in the axial direction, the sectional rms lift coefficient is always greater than or equal to the finite section rms lift coefficient. In the current paper we have studied a much longer cylinder, in which the deteriorated spanwise correlation results in a much smaller C_l'. The same phenomenon has also been mentioned in the work of Lee, Campbell, and Hambric (2014). As for the wavy cylinders examined here, great drag and lift mitigation has been achieved

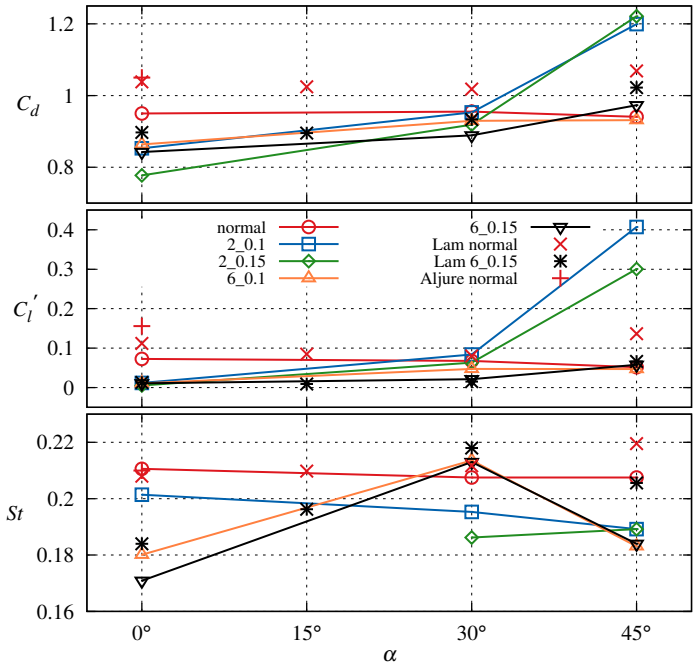

FIGURE 4.2: Summary of the mean drag coefficient C_d, rms lift force coefficient $C_l^{'}$ and the Strouhal number

at $\alpha = 0°$. The Strouhal numbers of the wavy cylinders also suffer certain decrease compared with the normal cylinder. The results obtained in our study agree qualitatively with that of Lam et al. (2010) at $Re = 3900$. Worthy of noting is that the 2_0.15 case, the primary frequency of the lift force coefficient becomes so weak that could not be detected, suggesting the complete suppression of the Kármán vortex shedding.

Situations are quite divided for the normal and wavy cylinders as the inclination angle increases. For the normal cylinder, an increase of the inclination angle up to $45°$ induces no drastic changes in the C_d, $C_l^{'}$ and St. This confirms the validity of the independence principle. As for the wavy cylinders, there is a discernible rise in both the C_d and $C_l^{'}$ as α grows to $30°$. Further increasing to $45°$, while the growth for the long-wavelength cylinders is moderate, both the drag and lift undergo a surge in the cases of $\lambda/D_m = 2$. The drag coefficient reaches around 1.2 and the lift becomes $60 \sim 80$ times of that of the normal cylinder. This implies a major deviation from the cosine rule. Since in the current paper C_d is defined based on the streamwise velocity U_x only, the surge in the mean drag coefficient could intuitively understood as being induced by the action of the additional spanwise velocity U_z on the tubercles: the steeper the waviness, the more pronounced this effect is, and the larger the C_d becomes. Another cause for the increase in the drag, as well as the lift, lies in the intensification or the resurrection of the Kármán vortex shedding with the increase of inclination angle (Roshko, 1954b). This also results in the increase in the lift coefficients. Frequency-wise, the wake instability in the 2_0.15 case revives as the inclination angle increases, and the Strouhal numbers for the short-wavelength cases are maintained at around 0.19. The long-wavelength cylinders, however, exhibit a relatively large variation in the St-α relationship: the shedding frequency ascents to around 0.21 at $\alpha = 30°$, and then drops to around 0.18 at $\alpha = 45°$. This phenomenon is also qualitatively manifested in the work of Lam et al. (2010). The detailed mechanism of the variations in the St with α, however, remains unclear and warrants further investigations.

Owing to the three-dimensional nature of the wavy geometry, it is also interesting

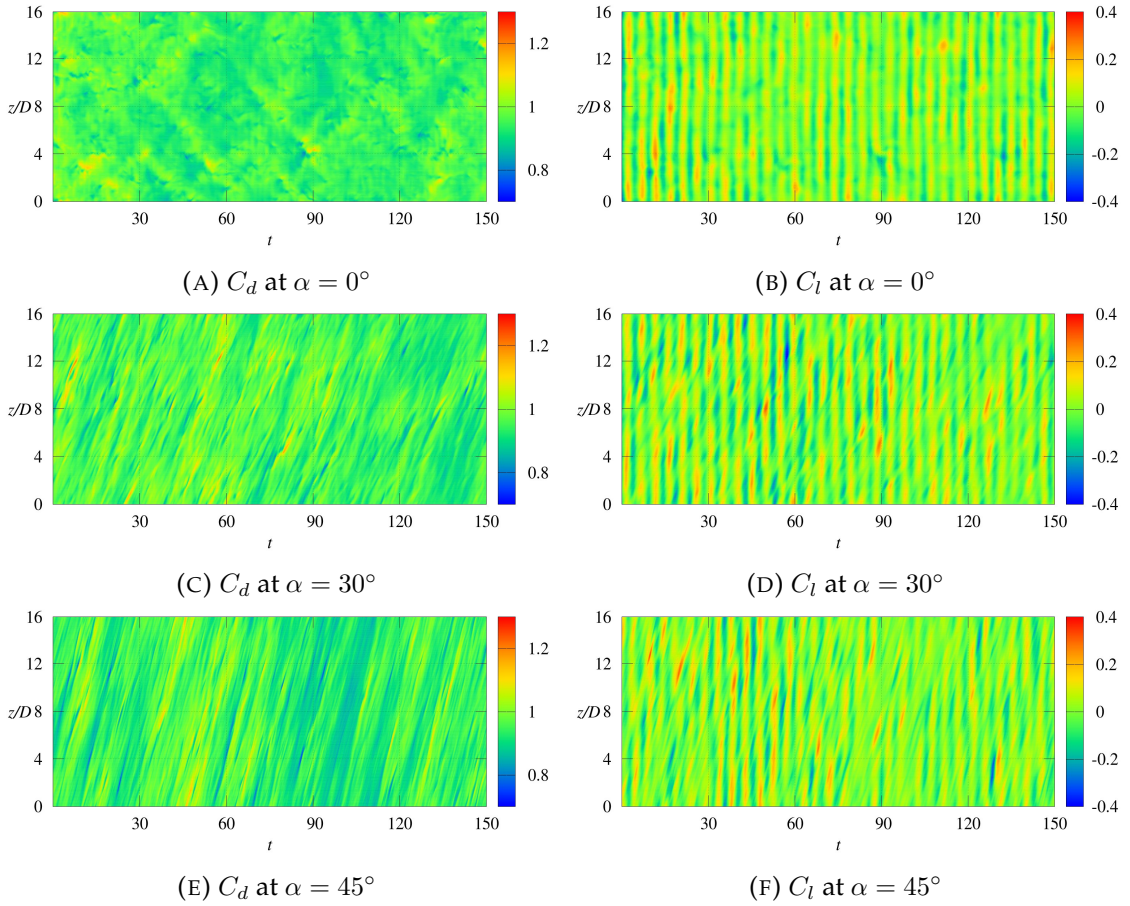

(A) C_d at $\alpha = 0°$ (B) C_l at $\alpha = 0°$

(C) C_d at $\alpha = 30°$ (D) C_l at $\alpha = 30°$

(E) C_d at $\alpha = 45°$ (F) C_l at $\alpha = 45°$

FIGURE 4.3: Spatial-temporal distribution of the force coefficients of the normal cylinder

to examine the spanwise distributions of the force coefficients. Figs. 4.3, 4.4 and 4.5 present such results for the circular cylinder, 2_0.15 and 6_0.15 wavy cylinders. In each of the plots, the horizontal axis represents the non-dimensional time and the vertical axis is the cylinder's axial coordinate. Note that the vertical axis of the normal cylinder is normalized by the cylinder diameter D and that of the wavy cylinders by the wavelength λ. Efforts are made to unify the legends however they are adjusted where necessary for better visualization of the patterns. The lift coefficient plots of the normal cylinder (Fig. 4.3) are generally consisted of repeated filaments parallel to the z-axis, with their regularity gradually obscured by the increasing yaw angle. Specifically, the filaments are somewhat obliquely stretched in the inclined cases, indicating that the local peak force is traveling along the cylinder in the direction of U_z. This kind of stretching pattern has also been identified by Yeo and Jones (2008) in their detached eddy simulations of yawed circular cylinders at $Re = 1.4 \times 10^5$, and they further related this phenomenon with the low-frequency vibrations of the inclined cables such as dry galloping of bridge cables. As for the drag coefficient plots, at $\alpha = 0°$, local maxima and minima that are induced by the random turbulence effect scatter the plot and no obvious patterns could be noticed. However, with the increase of the inclination angle, the stretching pattern takes place and appears to be more persistent than the lift coefficients. It could be imagined that in the inclined cases, the random turbulence that engenders the local maxima and minima are being transported by the spanwise velocity component, resulting in the stretched patterns. It should be noted that the spanwise flow acting on the cylinder surface is not only induced by the incoming freestream flow, but also the secondary axial velocity in

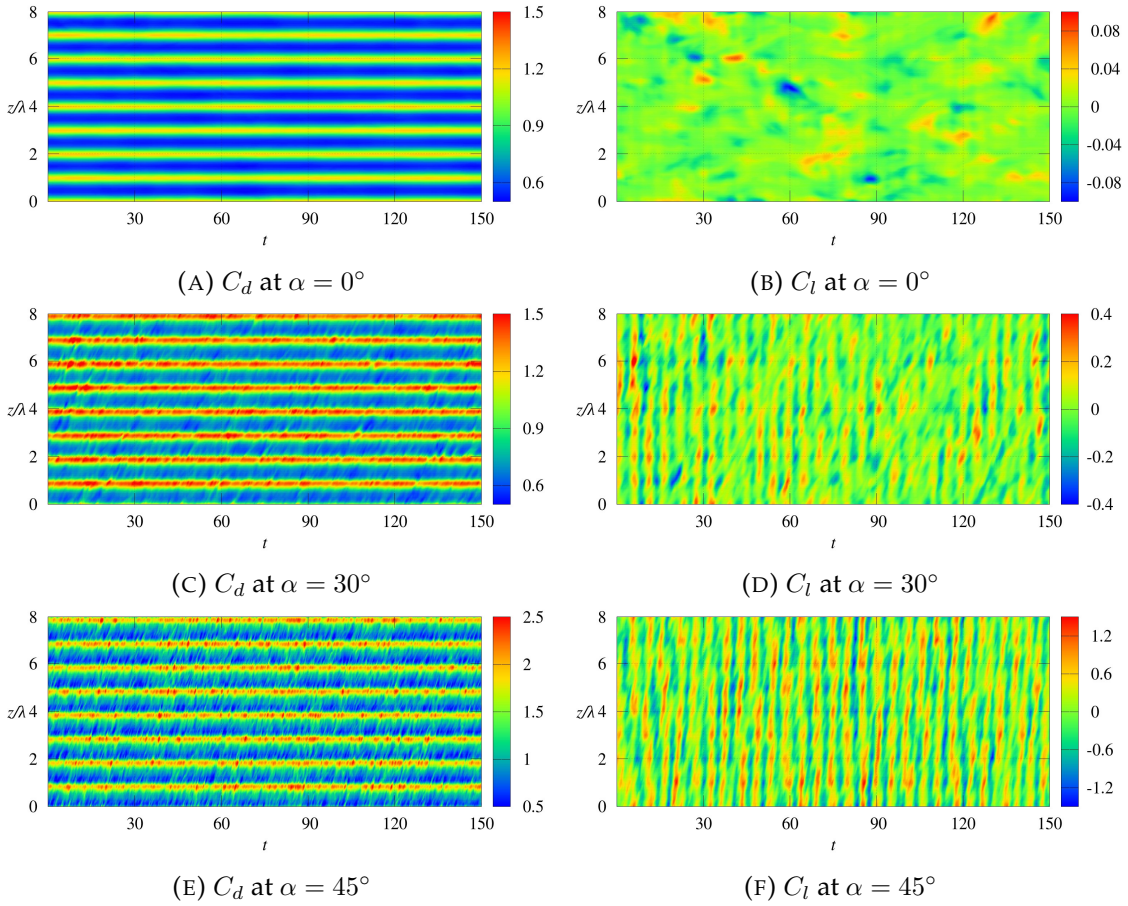

(A) C_d at $\alpha = 0°$ (B) C_l at $\alpha = 0°$

(C) C_d at $\alpha = 30°$ (D) C_l at $\alpha = 30°$

(E) C_d at $\alpha = 45°$ (F) C_l at $\alpha = 45°$

FIGURE 4.4: Spatial-temporal distribution of the force coefficients of the wavy cylinder with $\lambda/D_m = 2$ and $a/D_m = 0.15$

the near wake. This aspect will be given a closer inspection in section 4.5.

Interestingly, while the lift coefficients of the 2_0.15 wavy cylinder (Fig. 4.4) are rendered with irregularity both temporally and spatially, a spanwisely periodic, temporally steady pattern prevails the C_d plot. This attests to our previous notion of the total suppression of the Kármán vortex shedding by this particular wavy cylinder. However, as the additional axial velocity intervenes, the temporal repeated pattern similar to the case of the normal cylinder appears, suggesting the resurrection of the Kármán instability in the wake. As for the drag coefficients in the inclined cases, the spanwise periodicity is well preserved, yet with less temporal steadiness. The position of the maximum sectional drag coefficient, however, shifts slightly to the lower part of the nodes, at which the flow attacks the local surface perpendicularly.

As for the 6_0.15 wavy cylinder (Fig. 4.5), while the drag coefficients share the same features with the 2_0.15 case, the spanwisely periodic pattern is also clearly manifested by the C_l in both inclined and non-inclined cases. Particularly, the temporal variation of the lift coefficients at the saddle plane appears much smaller compared with that at the node. To further shed light on this matter, FFT analysis are conducted for the sectional lift coefficients and the results are presented in Fig. 4.6, with the legend representing the absolute magnitude of the Fourier transform. The normal and the 2_0.15 cylinders are also included for the sake of completeness. Compared with the normal cylinder, in which the vortices shed with uniform intensity along the axial direction, the energy content at the St frequency differs between the nodes and saddles for the wavy cylinders. Strong fluctuation of the C_l is associated with the node and weak with the saddle. Notably, for

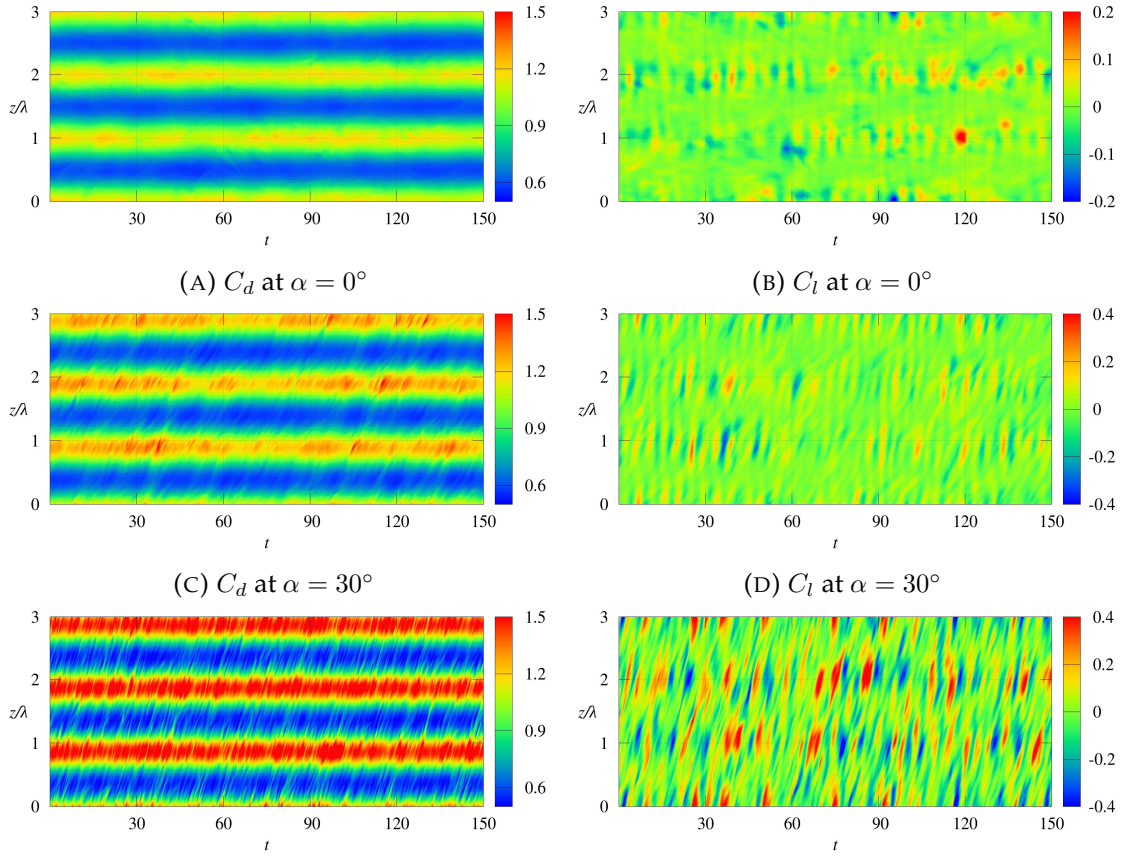

(A) C_d at $\alpha = 0°$ (B) C_l at $\alpha = 0°$

(C) C_d at $\alpha = 30°$ (D) C_l at $\alpha = 30°$

(E) C_d at $\alpha = 45°$ (F) C_l at $\alpha = 45°$

FIGURE 4.5: Spatial-temporal distribution of the force coefficients of the wavy cylinder with $\lambda/D_m = 6$ and $a/D_m = 0.15$

the 6_0.15 wavy cylinder at zero incidence, the lift coefficient is mitigated so significantly that it remains almost dormant for a large portion in the vicinity of the saddle plane. This spanwise intermittency also persists for the $\alpha = 30°$ and $45°$ cases to some extent. Another feature in the these plots is that as the inclination angle increases, the energy content in the lift force tend to be dispersed into multiple frequencies. This should be a result of the irregularity of the force coefficients over the cylinder with time.

4.3 Span-wise correlation of the lift force coefficients

With the spatial-temporal force coefficients at hand, the spanwise correlation of the lift coefficients, which quantitatively indicates the three-dimensionality of the cross-cylinder flows, could be obtained. The cross-correlation coefficient between forces at different spanwise locations is calculated as

$$\rho\left(z_i, z_j\right) = \frac{\sum\limits_{t=0}\left\{\left[C_l\left(z_i,t\right) - \overline{C_l\left(z_i\right)}\right]\left[C_l\left(z_j,t\right) - \overline{C_l\left(z_j\right)}\right]\right\}}{\sqrt{\sum\limits_{t=0}\left[C_l\left(z_i,t\right) - \overline{C_l\left(z_i\right)}\right]^2}\sqrt{\sum\limits_{t=0}\left[C_l\left(z_j,t\right) - \overline{C_l\left(z_j\right)}\right]^2}}, \tag{4.2}$$

in which $C_l\left(z,t\right)$ is the lift force coefficient at spanwise location z and time t, the overline of which is its time-averaged value. The related correlation length is defined as

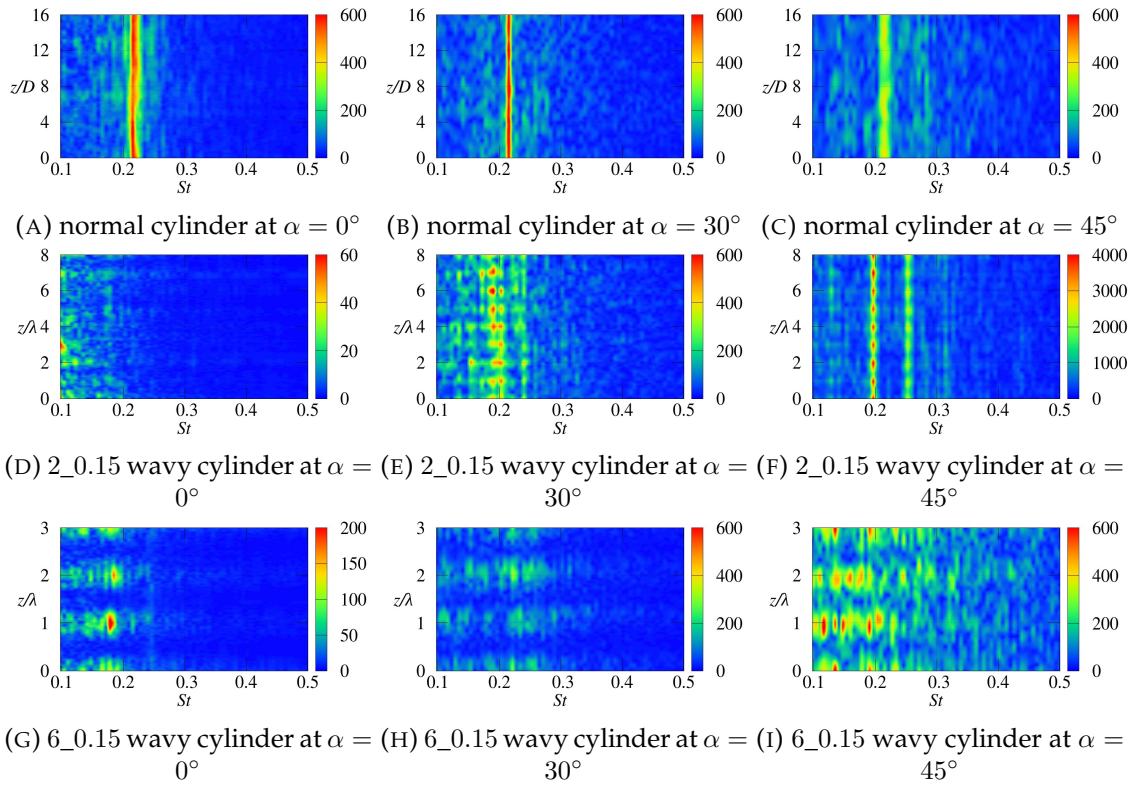

(A) normal cylinder at $\alpha = 0°$ (B) normal cylinder at $\alpha = 30°$ (C) normal cylinder at $\alpha = 45°$

(D) 2_0.15 wavy cylinder at $\alpha = 0°$ (E) 2_0.15 wavy cylinder at $\alpha = 30°$ (F) 2_0.15 wavy cylinder at $\alpha = 45°$

(G) 6_0.15 wavy cylinder at $\alpha = 0°$ (H) 6_0.15 wavy cylinder at $\alpha = 30°$ (I) 6_0.15 wavy cylinder at $\alpha = 45°$

FIGURE 4.6: Magnitude spectrum of the Fourier transform of the sectional lift coefficients

$\Lambda = \int_0^\infty \rho(z)\, dz$. Since the sectional lift coefficients as shown in Fig. 4.3, 4.4 and 4.5 are calculated based on the axial mesh cells, for each set of data Equation 4.2 would generate a symmetric $N_z \times N_z$ matrix, where N_z is the number of the grids in the spanwise direction. Such matrices for the cases of 2_0.15 and 6_0.15 wavy cylinders are visualized in Fig. 4.7. In these plots, the main diagonal represents the self-correlation and thus features the largest value of unity. High value is also maintained in the vicinity of the top left (as well as bottom right, because of the symmetry) corner, which stands for the correlation of the periodic spanwise ends. An important pattern to notice with the increasing inclination angle is that the dependence of the spanwise reference location on the cross-correlation gradually becomes clear. To be more specific, the correlation curve drops slower if the reference point is selected at the node than at the saddle. Thus, the conventional point-to-point representation of the cross-correlation is not appropriate here because the ambiguity in the choice of the reference point.

In order to circumvent this problem, the procedure described by Blackburn and Melbourne (1996) is employed here to condense the cross correlation information. Since in these matrices, the elements in each diagonal parallel to the main diagonal represent the cross-correlations of two locations separated by the same distance, each diagonal is averaged to obtain the mean values of cross correlations ρ as a function of the spanwise separation s. The results of such an procedure is given in Fig. 4.8. Only half of the total length is shown here because of the cyclic boundary condition we have enforced in the spanwise ends. There has been quite a scatter in the literature on the lift correlation of a circular cylinder, particularly at $Re = 5000$. While from the research of Leehey and Hanson (1970) and Iida et al. (1997) a correlation length of around $\Lambda \approx 6 \sim 7D$ was obtained, Norberg (2003) identified a locally maximum value of $\Lambda/D \approx 10.5$ at $Re = 5000$, with which, as he reasoned, the spanwise resonance in between the vortical structures

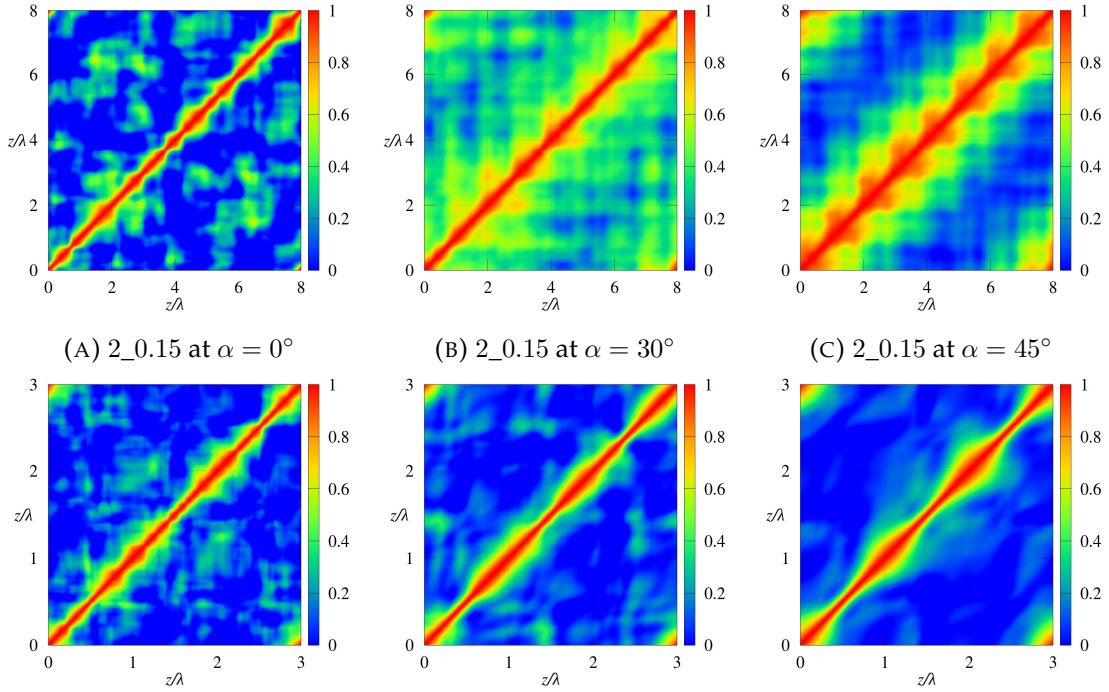

(A) 2_0.15 at $\alpha = 0°$ (B) 2_0.15 at $\alpha = 30°$ (C) 2_0.15 at $\alpha = 45°$

(D) 6_0.15 at $\alpha = 0°$ (E) 6_0.15 at $\alpha = 30°$ (F) 6_0.15 at $\alpha = 45°$

FIGURE 4.7: Cross correlation matrices of the lift force coefficients for the 2_0.15 and 6_0.15 wavy cylinders

of mode B (Williamson, 1996) and shear layer vortices (Bloor, 1964) is associated. Recently, Lee and Nguyen (2007) conducted a detached eddy simulation of flow around circular cylinders at the same Reynolds number. The correlation curve in their research converged to zero at $8D$, and the resulted correlation length Λ should be smaller than $5D$. We have simulated the cylinder cross flow of the same spanwise extent with Lee et al. Lee, Campbell, and Hambric, 2014's research. However, in our case the lift force of normal cylinder at zero incidence is far better correlated than that in their work. In view of this, the current work does not fully accommodate the three-dimensionality in the wake of the normal cylinder, for which a spanwise length of more than $21D$ is required based on the result of Norberg (2003). However, we argue that with the same numerical setup and schemes, the flow characteristics of different cases could be studied on the comparative basis. This being said, we proceed our discussion on the spanwise correlations of the various cases in the current work.

In the case of $\alpha = 0°$, while the shedding of the vortices in the normal cylinder wake exhibits quite high spanwise uniformity, the introduction of the axial waviness greatly reduces the correlation length of the sectional lift force. However, the role the axial velocity component U_z plays in the spanwise correlations seems to differ between the normal and wavy cylinders. For the former, there is a monotonic decrease of the correlation coefficients with the increase of α. This is also reflected in the sectional lift coefficients in Fig. 4.3 as the obliquely stretched pattern gradually obscure the plots. On the other hand, the shedding uniformity in the wake of the wavy cylinders appears to be enhanced with the existence of U_z for the wavy cylinders. Take the 2_0.15 cylinder for example. At $\alpha = 0°$, because of the annihilation of the Kármán vortices, the lift forces are generated by the chaotic turbulence effect and thus are poorly correlated. The vortex shedding revives and further strengthens with the increasing inclination angle, and the lift forces

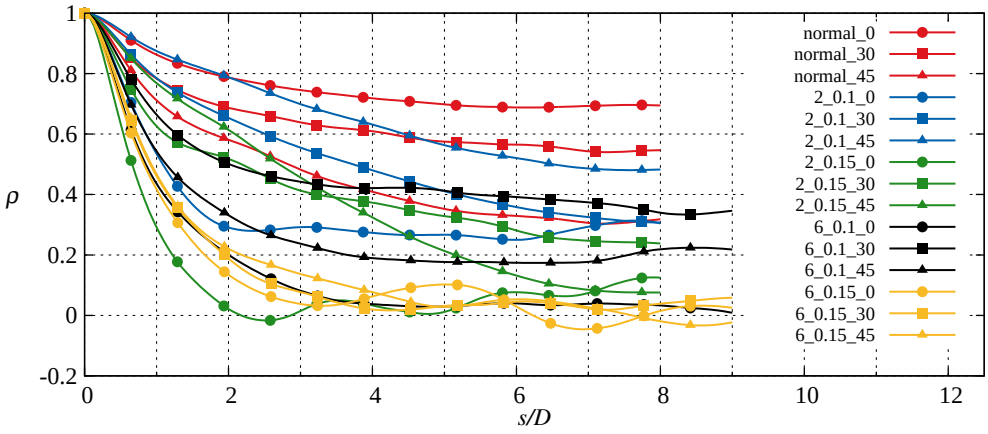

FIGURE 4.8: The averaged spanwise correlations of the lift force coefficients

are largely governed by the well-organized and periodic vortices, which, albeit highly three-dimensional, still takes certain spanwise distance to decorrelate. One exception is made by the 6_0.15 cylinder, in which the lift correlation remains low regardless of the inclination angle. This will be further discussed in section 4.6 by the visualization of the wake vortical structures.

4.4 Sectional force, vortex formation length and pressure

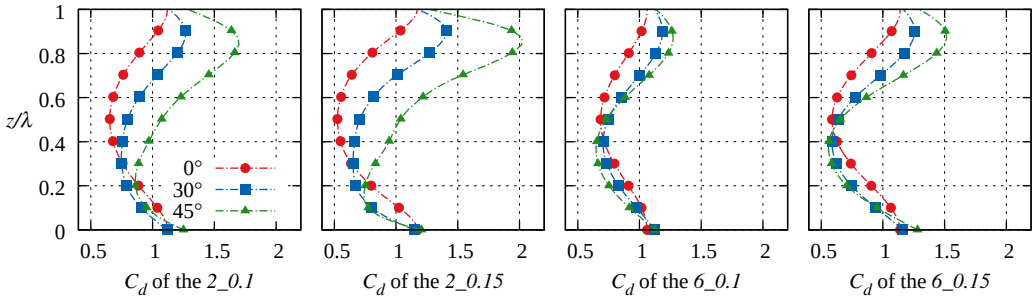

(A) The sectional drag coefficients.

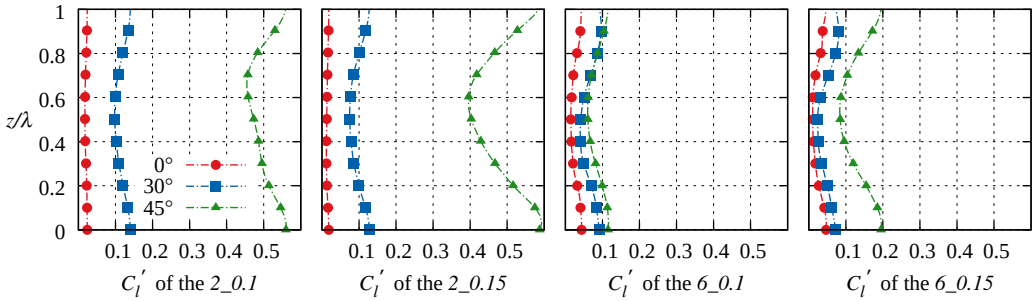

(B) The sectional rms lift coefficients.

FIGURE 4.9: Span-wise distribution of the mean drag and rms lift coefficients

As has been elucidated in the section 4.2, great variation of the force coefficients are observed in the spanwise direction. Meanwhile, it has also been pointed out in previous

researches that the wake of the wavy cylinders presents inherently three-dimensional flow structures. It is generally acknowledged that the reduced drag is signaled by the elongated vortex formation length as well as the increased base pressure (Zdravkovich, 1997). However, the inter-relationship between the sectional forces and these wake properties, especially in the inclined cases, are less studied. In the current section, we intend to present a detailed analysis to this aspect.

Firstly, the spatial-temporal distributions of the force coefficients, as have been illustrated in Fig. 4.3, 4.4 and 4.5, are condensed by taking the temporally averaged (for C_d) or rms values (for C_l) for each span-wise section. The results are presented in Fig. 4.9. A general trend to notice, in addition to the surge in the overall values of C_d and C_l', is the enlarged variation in their sectional values as the inclination angle increases. For example, in the extreme case of 2_0.15 cylinder at $\alpha = 45°$, the minima in the drag coefficient is around 0.75 while the maxima reaches as high as 2. Judging from the same figure, it could be appreciated that the increase in the total drag is largely contributed by the surge at the location slightly to the bottom of the node plane, where the inclined flow attacks the surface perpendicularly. It is also worthwhile to point out that since in the current figure the rms lift coefficients are calculated sectionally, their spanwise averaged values judged from Fig. 4.9b tend to be larger than that is shown in Fig. 4.2, in which the C_l is firstly axially averaged and then be applied the rms operator.

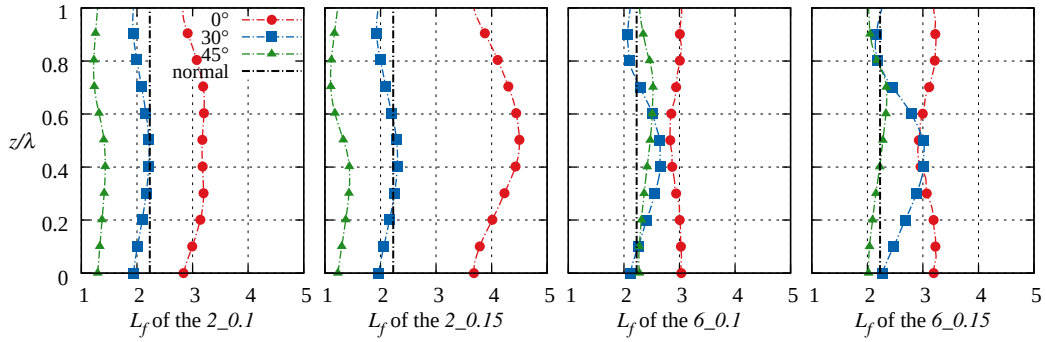

FIGURE 4.10: Span-wise variation of the vortex formation length L_f. $z/\lambda = 0$ and 1 represent the node plane and $z/\lambda = 0.5$ is the saddle plane.

Fig. 4.10 compiles the sectional vortex formation length L_f of the wavy cylinders. In the current context, L_f is simply defined by the intersection of the contour $u_{mean_x} = 0$ and the plane $y = 0$, where u_{mean_x} is the mean stream-wise velocity. Since the variation of the vortex formation lengths of the normal cylinder at different inclination angles is negligibly small, they are indicated by a single dot-dashed line in each figure for comparison. As has been shown in Fig. 4.9a, at zero inclination angle, for the short and long-wavelength cylinders alike, the drag coefficient maximizes at the node and minimizes at the saddle. However, the vortex formation lengths for the long and short-wavelength cylinders present an inverse fashion regarding their spanwise distributions: L_f is shorter at the node and longer at the saddle for the wavy cylinders with $\lambda/D_m = 2$ and the opposite is true for the ones with $\lambda/D_m = 6$. Similar phenomenon has also been identified by Lin et al. (2016) and Lam and Lin (2009), and they have ascribed it to the flow separation features and the wake vortical structures for the different wavelengths. A nice schematic explanation for this phenomenon could be found in Fig. 10 of Lin et al. (2016). Specifically, for $\lambda/D_m < 6$, the separation occurs earlier at the saddle and later at the node, thus, the separated free shear layers at the node appear convergent toward each other and at the saddle the trend is divergent. This difference leads to the larger vortex formation length at the saddle and smaller at the node. Whereas for $\lambda/D_m > 6$, the separation is

delayed at the saddle and forwarded at the node, thus an inverse fashion could be observed in the L_f. We will also cover the separation topology in the next section. Despite these sectional differences, the L_f even at its smallest sectional value of the four wavy cylinders is still larger than that of the normal cylinder, exemplifying their flow control efficacy at $\alpha = 0°$.

Things are quite different in the inclined cases. For the short-wavelength cylinders, the vortex formation length shrinks significantly to be inferior to that of the normal cylinder, collaborating the increase in the drag, as well as the decrease in the base pressure, as will be discussed next. The sectional difference in L_f fades with the increase of α. As for the long-wavelength cylinder, the shrinkage in the L_f as α increases is somewhat smaller. However, great sectional variation is observed at $\alpha = 30°$, in which the curved shape appears to be flipped, i.e., L_f becomes longer at the saddle and shorter at the node. Further increasing α to $45°$, the sectional variation becomes trivial again. Not much resemblance could be noticed in the between the shapes in L_f and C_d. Thus, the common belief that larger L_f is associated with smaller C_d does not hold true in the sectional sense.

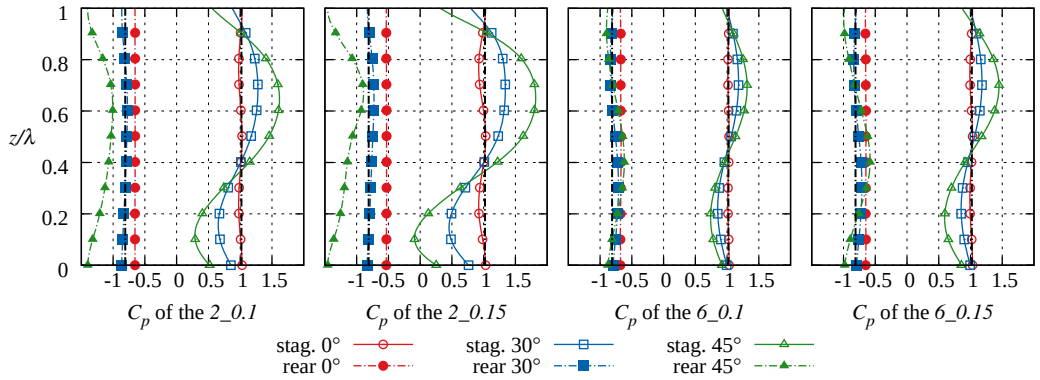

FIGURE 4.11: The sectional pressure coefficients at the stagnation and base lines. $z/\lambda = 0$ and 1 represent the node plane and $z/\lambda = 0.5$ is the saddle plane.

In Fig. 4.11, the pressure coefficients at both the stagnation and base lines are plotted for the various cases as a function of the normalized wavelength. The pressure coefficient is calculated as $C_p = (p - p_\infty)/(\rho U_x^2/2)$, in which p_∞ refers to the pressure at the outlet boundary. In the zero-angle cases, while the spanwise variation of the base pressure seems negligible, there is discernible variation to observe for the stagnation pressure, especially in the 2_0.15 wavy cylinder. C_p undergoes a smooth peak-valley-peak transition from the node to saddle, making two waves in one geometric wavelength. The pressure difference between the cylinder's stagnation and base, at which the local pressure forces act in the same direction of the drag, is often used as an indicator of the effectiveness of the drag mitigation (Zdravkovich, 1997). Since at both the base and stagnation lines C_p does not exhibit much variation between the nodes and saddles, the big sectional difference of the drag coefficients, as is shown in Fig. 4.9a, seems difficult to comprehend. As a matter of fact, by considering the azimuthal contribution of the local pressure to the total drag, we have explained in our previous work that the difference of the sectional drag between the node and saddle planes mainly originates from the pressure distribution in the range of $\theta \approx 30° \sim 70°$ (θ being calculated from the stagnation point), where the C_p at the saddle plane contribute more negatively to the total drag than that at the node (see Fig. 18 of Zhang et al. (2016)). Nevertheless, the base pressure of the wavy cylinders at zero incidence is significantly larger than the normal cylinder. This serves as the main cause for the large reduction in C_d of the wavy cylinders.

In the inclined cases, the pressure coefficients at the stagnation line exhibits drastic variation as α increases. The maxima and minima C_ps shift to the region in between the node and saddle planes. This is a direct result of the inclined flow hitting on and separating from the wavy tubercles. The sectional variation in the base pressure is less drastic, and it is not until α reaches $45°$ that the spanwise difference begins to be significant. From an axially-averaged sense, the stagnation pressure coefficients, however drastically they fluctuate in the spanwise direction, remains at a mean value of 1, while a consistent drop in the base C_p is observed as α increases. Thus, the correspondence of the larger C_d with smaller base pressure Zdravkovich (1997) is still valid for the inclined wavy cylinders. On the other hand, by comparing the undulated shape of C_p in the current figure and the drag coefficients in Fig. 4.9a, it is not difficult to find certain similarity between the stagnation C_p and the C_d. Thus, from a sectional point of view, it is reasonable to concluded that the sectional drag in the inclined wavy cylinder is more influenced by the pressure at the stagnation line rather than the base.

4.5 Surface flow topology

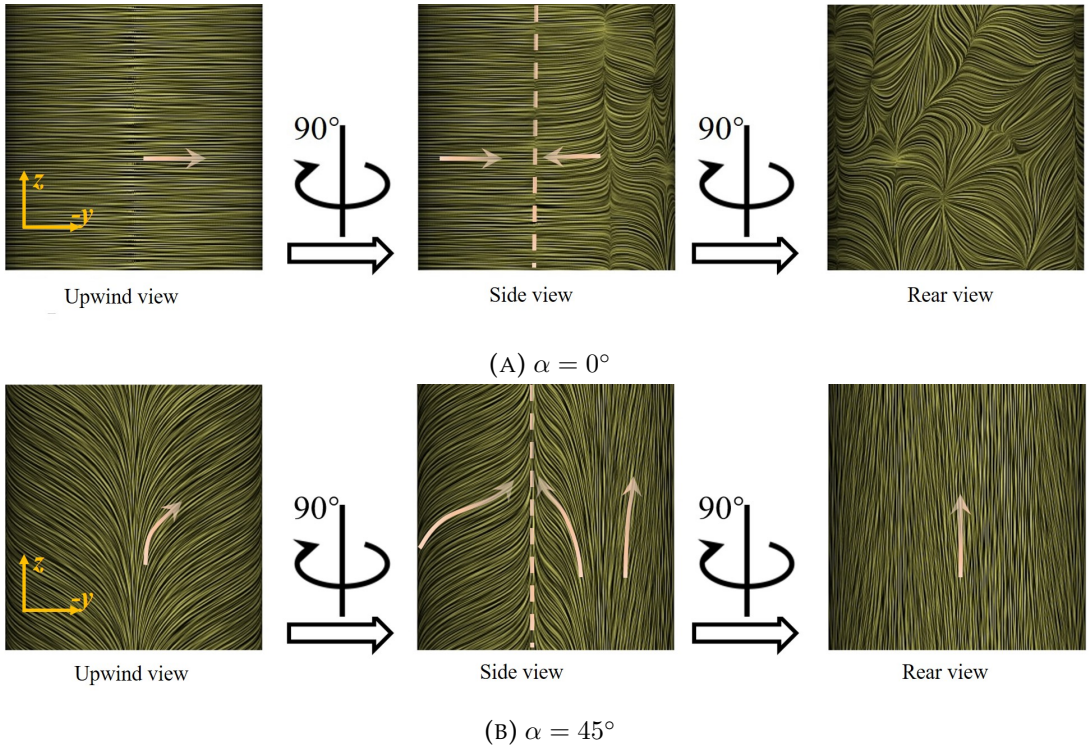

FIGURE 4.12: Averaged wall shear stress fields visualized by LIC method for the normal cylinder. The upwind, side and rear views are taken in the x, y and $-x$ directions, respectively. The arrows indicate the local flow direction. The dashed lines in the side views depict the boundary layer separation lines.

The time-averaged wall shear stress fields are visualized by the line integral convolution (LIC) technique (Cabral and Leedom, 1993) in this section to give an overview of the surface flow topology on the cylinder walls. Fig. 4.12 depicts the surface flow structure for the normal cylinder at $\alpha = 0°$ and $45°$. For the former angle, the surface flow topology could be categorized into three major regions: the boundary layer region that emanates from the upwind stagnation line and ends at the separation line in the side

view, the well-organized reverse flow region, and the chaotic wake region with no clear pattern to notice. When it comes to $\alpha = 45°$, all the three regions could still be recognized. The boundary layer travels downstream with a consistent spanwise motion, and is met by the tilted reverse flow at the separation line. The separation occurs at almost the same location with that in the zero angle case, validating Sear's theory (Sears, 1948) of the independence principle on the boundary layer. In place of the chaotic wake region, the rear view of the inclined cylinder is rendered by the strong spanwise motion. This indicates the existence of the secondary axial flow in the near wake of the cylinder, as has been reported in Matsumoto et al. (1990).

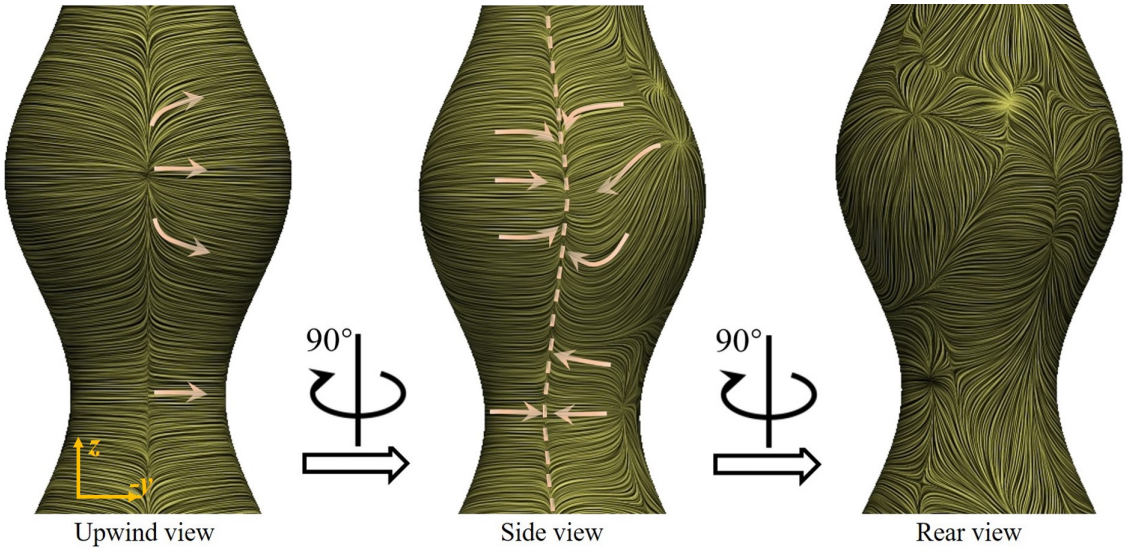

(A) $\alpha = 0°$

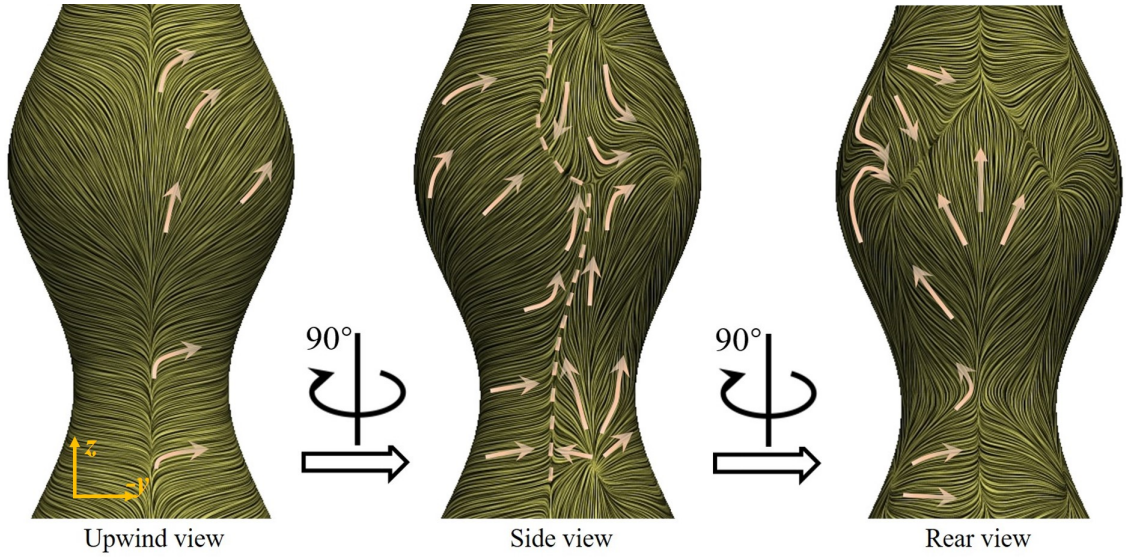

(B) $\alpha = 45°$

FIGURE 4.13: Averaged wall shear stress fields visualized by LIC method for the 2_0.15 cylinder. Please refer to Fig. 4.12 for the specifications.

The surface flow topology of the 2_0.15 wavy cylinder, as is depicted in Fig. 4.13, is more complicated than the normal cylinder. At $\alpha = 0°$, the boundary layer flow diverges from the stagnation point at the node plane and then converges to the node again as the flow is about to separate. This trend gradually weakens until at the saddle plane such

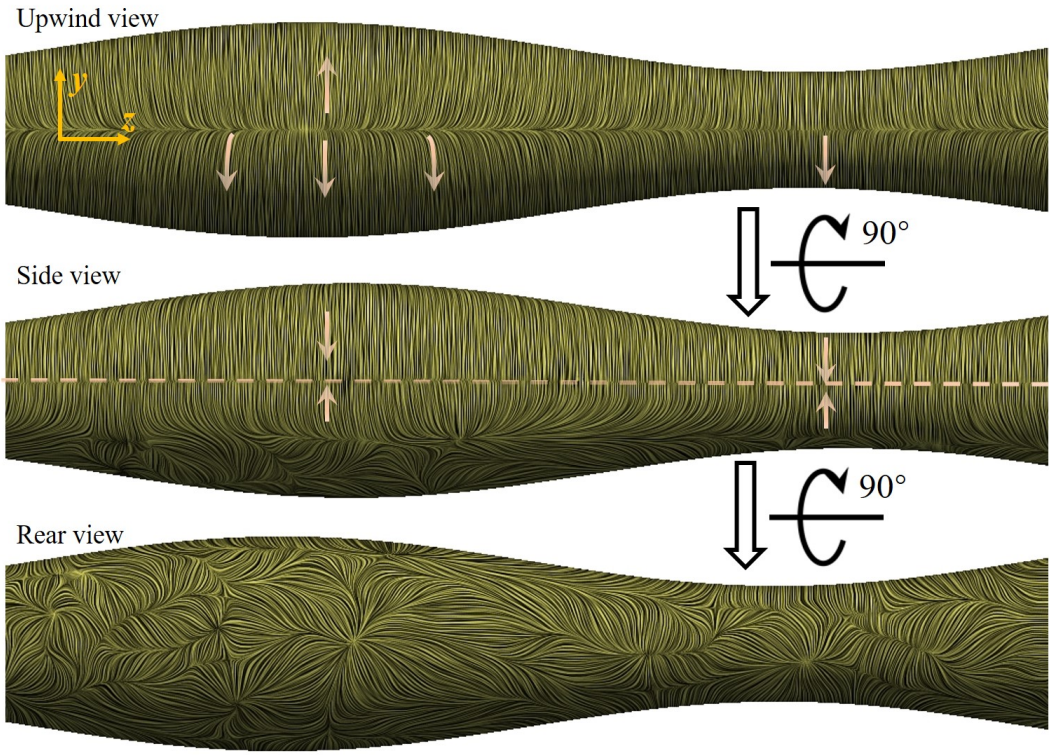

(A) $\alpha = 0°$

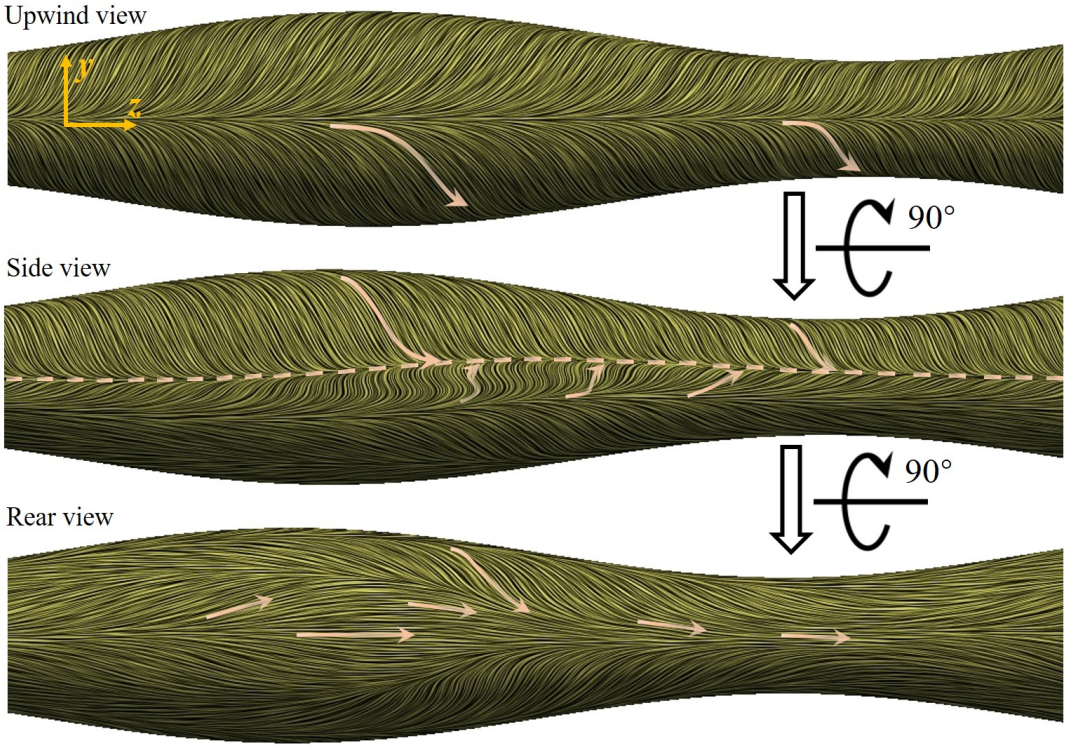

(B) $\alpha = 45°$

FIGURE 4.14: Averaged wall shear stress fields visualized by LIC method for the 6_0.15 cylinder. Please refer to Fig. 4.12 for the specifications.

curved motion dies out and the boundary layer flows straightly from the stagnation until separation. Unlike uniform separation line in the normal cylinder case, the wavy cylinder poses an undulated separation structures, in which the separation angle is delayed at the node and forwarded at the saddle. This collaborates the discussion on the vortex formation length in Fig. 4.10. The reverse flow region does not hold symmetry to the node plane. This might be caused by the insufficient averaging time. Nevertheless, the reverse flow also appears to maintain a convergent trend to the node. The rear view of the wavy cylinder remains chaotic. The situation is even more intricate at $\alpha = 45°$. Since the inclined flow attacks the wavy cylinder perpendicularly at the lower side of the tubercle, the local boundary layer there is featured by strongly tilted streamlines in the same direction of the incoming velocity. However, once the streamlines travel over the tubercle to its upper side, the axial velocity is blocked and the spanwise momentum of the surface flow is largely weakened. Owing to this highly three dimensional boundary layer structure in the upwind side, the wavy cylinder at $\alpha = 45°$ engenders a complex separation line, as is indicated by the dashed line in the side view. The reverse flow appears to be emanated from the the source points located slightly lower to the each saddle planes. Thus, as could be observed in the side view, the upper side of the tubercle features the reverse flow with downward motion and the lower part with the upward motion. These two opposite streams collide near the node plane and converge to the sink point at further downstream. The rear side of the inclined wavy cylinder poses great symmetry with respect to the x-z plane. The streamlines in the base region of the node is featured by strong spanwise motion, signaling the presence of the axial flow as has been introduced in the inclined normal cylinder. This axial flow even causes local separation at the upper side of the tubercle. From the node's upper side to the saddle's lower side, the flow field is less affected by the axial flow since this region is resided at the leeward side (in terms of the wake axial flow) of the node.

As for the $6\_0.15$ cylinder (Fig. 4.14), the situation in the $\alpha = 0°$ case largely resembles the normal cylinder. Owing to the mild geometric steepness, the curved motion of the boundary layer near the node is much weaker than that in the $2\_0.15$ case. The separation features an almost straight line over the spanwise direction just like the normal cylinder. The reverse flow is well-formed and could be easily be recognized. The flow field in the rear side still remain patternless as the other two cylinders. In the case of $\alpha = 45°$, as the blocking effect of the node to the spanwise velocity component becomes weak, consistent axial motion in the boundary layer flow is observed at both the node and saddle. The separation line is slightly undulated. The base flow structure is reorganized by the secondary axial flow and poses symmetry to the x-y plane. Much more diluted patterns, compared to the $2\_0.15$ cylinder, could still be recognized in the rear view. However, the local separation does not occur in the rear side for the current case.

4.6 Three-dimensional vortical structures

An important discovery of the current work is the cessation of the flow control effectiveness as the wavy cylinders are placed inclined to the flow. This is manifested by the surge in the drag and lift coefficients, shrinkage of the vortex formation length as well as the decrease in the base pressure. Particularly, in the case of $2\_0.15$ wavy cylinder, the Kármán instability that is dormant in the zero incidence case is brought alive by the axial velocity U_z. In this section, an attempt is made to shed light upon this matter by visualizing the three-dimensional vortical structures in the wakes of the wavy cylinders.

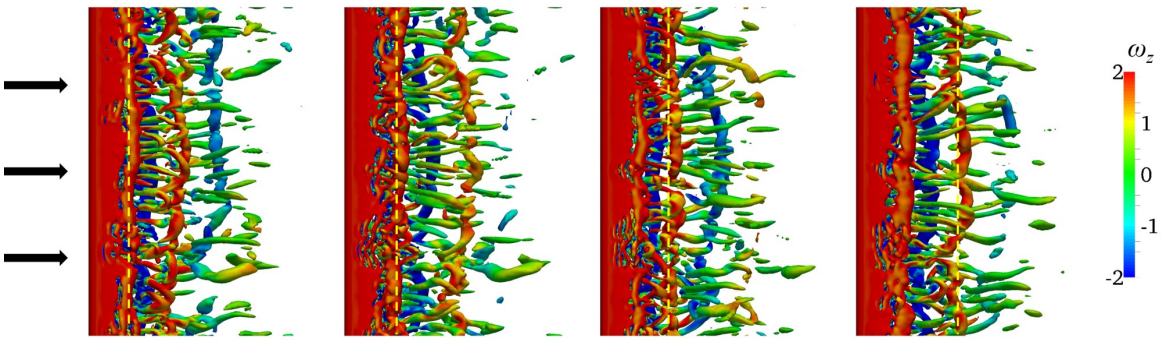

(A) $\alpha = 0°$

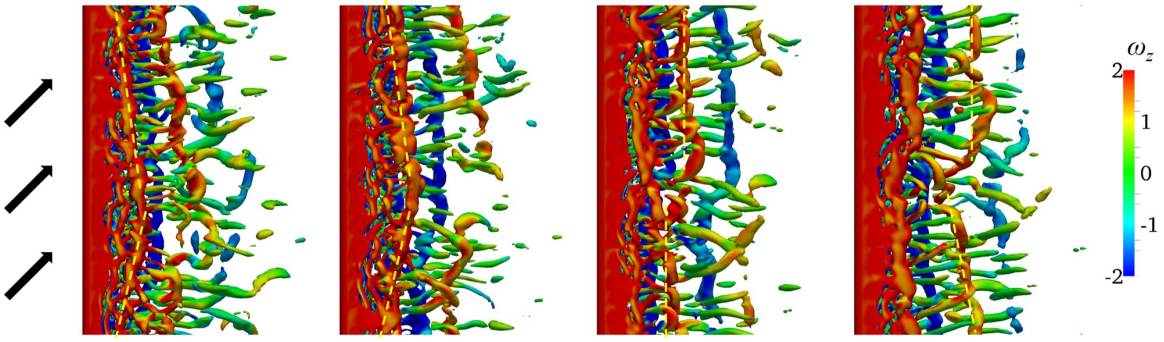

(B) $\alpha = 45°$

FIGURE 4.15: Iso-surfaces of $Q = 0.5$ for the flow around the normal cylinder at four successive instants with an interval of 2 non-dimensional seconds.

Fig. 4.15 shows the instantaneous vortex flow in the wake of the normal cylinder at four successive instants intervaled by 2 non-dimensional seconds. The vortices are described by the iso-surface of $Q = 0.5$, where Q is the second invariant of the velocity gradient tensor (Hunt, Wray, and Moin, 1988). The surfaces are colored by the spanwise vorticity ω_z in order to roughly distinguish the vortices that shed from the one side from another. Yellow dashed lines are created to indicate the development of the vortex shedding process. At $\alpha = 0°$, although the integrity of the shear layer sheets gets constantly disrupted by the Kelvin-Helmholtz instability (Bloor, 1964; Prasad and Williamson, 1997), the development of the mature Kármán vortex tubes appears quite uniform throughout the spanwise direction. Besides, the fine scale streamwise vortices in the shape of Mode B (Williamson, 1996) could also be clearly observed. When it comes to $\alpha = 45°$, significant spanwise variation in the Kármán vortex tubes could be noticed. Particularly, in the four frames shown in Fig. 4.15b, the oblique development (first two frames), breakdown (third frame) and misalignment (last frame) of the vortex shedding have been captured. This kind of phenomenon collaborates the deteriorated lift correlation at $45°$ as is shown in Fig. 4.8. However, such phenomenon only occurs sporadically, thus it is not of the same nature with the double-mode shedding reported by Ramberg (1983).

The Q iso-surface for the wake of the 2_0.15 wavy cylinder is presented in Fig. 4.16. At $\alpha = 0°$, instead of the intact Kármán vortex tubes found in then normal cylinder, the near wake of the wavy cylinder is mainly characterized by break down of the free shear layer owing to the mechanism of the KH instability. This process appears to occur independently by blocks in between each wavelength, as is nicely shown in the second frame. While the generated KH vortices are convected downstream, they are deformed

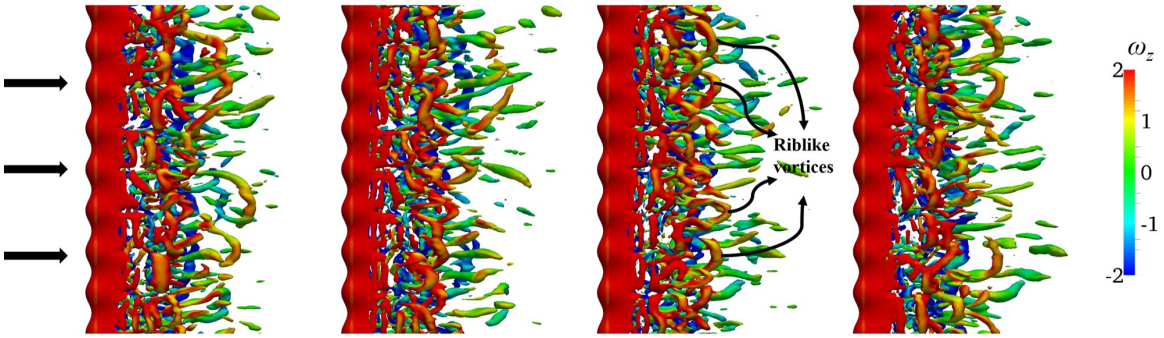

(A) $\alpha = 0°$

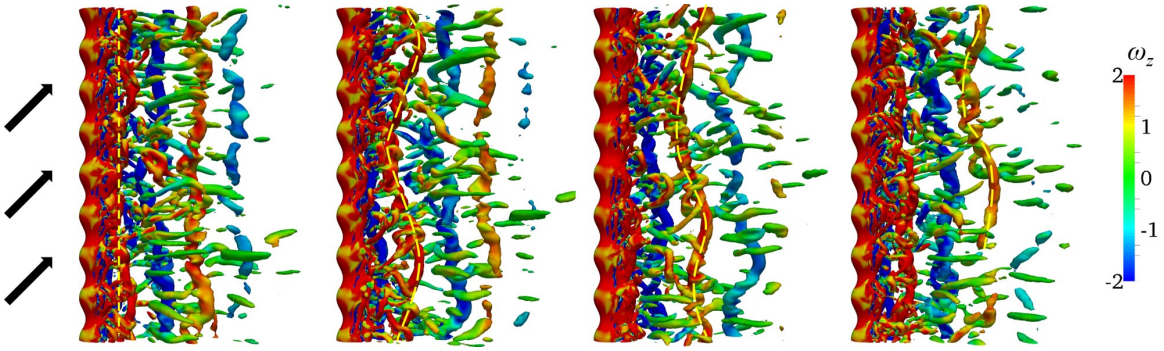

(B) $\alpha = 45°$

FIGURE 4.16: Iso-surfaces of $Q = 0.5$ for the flow around the 2_0.15 wavy cylinder at four successive instants with an interval of 2 non-dimensional seconds.

by the uneven velocity distribution at the node and saddle and form the riblike vortices as indicated in the third frame. Such a vortical structure has also been visualized by Lam and Lin (2009) at $Re = 100$. These small scale vortices grows weaker and weaker until they disappear in the further downstream. In contrast, even though the breakdown of the free shear layer in the $\alpha = 45°$ case shows great irregularity, the wake is able to reorganize itself to form the clear Kármán vortex tubes, as are shown in Fig. 4.16b. The four successive frames clearly depicts the formation, development and diminish of the vortex shedding process. However, although the Kármán vortex tubes remain intact, they vary greatly in the spanwise direction. This has led to the low lift correlation reported in Fig. 4.8. Still, no sign of the inclined shedding phenomenon has been observed in this case.

For the 6_0.15 wavy cylinder (Fig. 4.17), Kármán vortex shedding does not manifest itself clearly in the case of $\alpha = 0°$. The wake is rendered orderless by small-scale streamwise vortices and the riblike vortices. These vortical structures decay very quickly as they move downstream. Interestingly, the four snapshots in Fig. 4.17a capture the transformation of the spanwise vortices into the streamwise ones. As is indicated by the black dashed circles, in the first frame the vortex of interest inherits strong spanwise vorticity from the free shear layer region. As it convects downstream, the ω_z intensity gradually weakens and at last it deforms into the streamwise vortex. Such kind of phenomenon could also be observed in many other locations. Different from the 2_0.15 case, Kármán vortex shedding does not recur, at least not intact, in the wake of the 6_0.15 wavy cylinder at 45°. Instead, large and small scale vortices intermingle with each other, rendering the wake even more chaotic than the zero angle case. The absence of the organized Kármán vortices in the current case also corresponds to the smaller increase in the total C_d

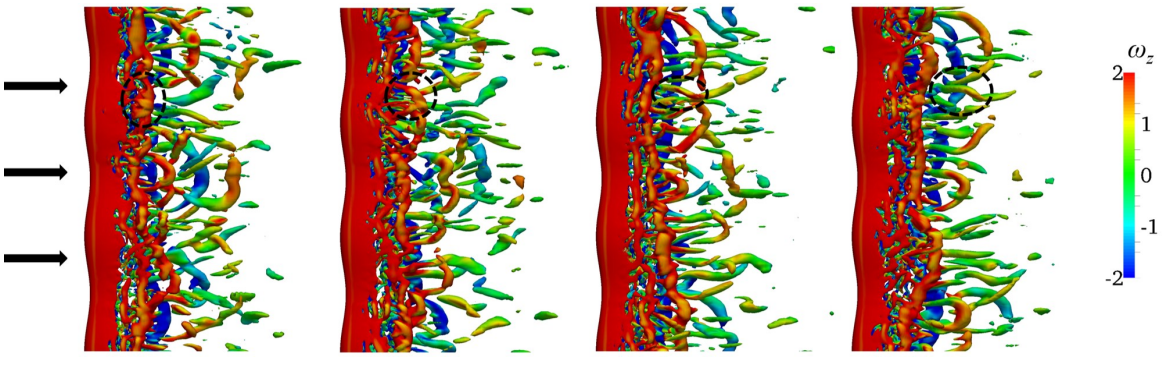

(A) $\alpha = 0°$

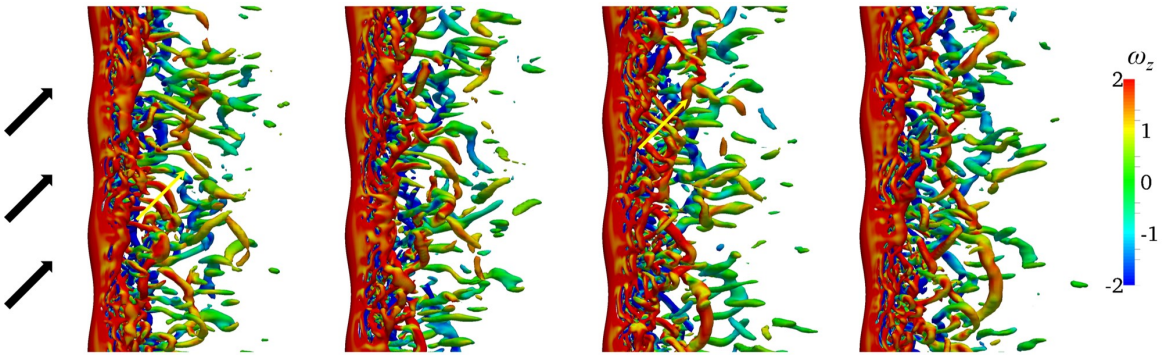

(B) $\alpha = 45°$

FIGURE 4.17: Iso-surfaces of $Q = 0.5$ for the flow around the 6_0.15 wavy cylinder at four successive instants with an interval of 2 non-dimensional seconds.

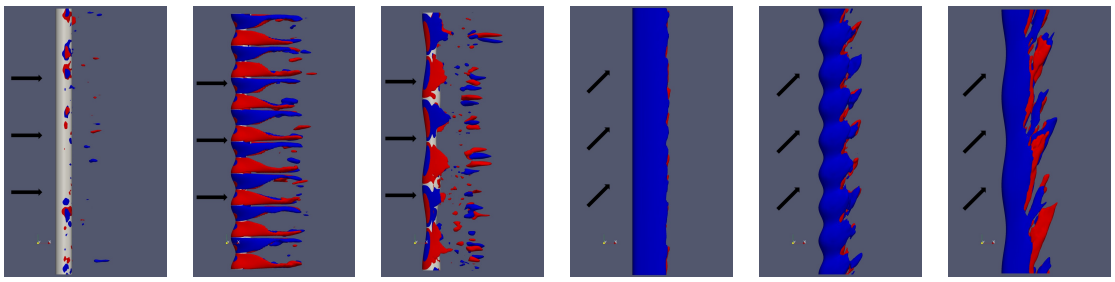

(A) normal, 0° (B) 2_0.15, 0° (C) 6_0.15, 0° (D) normal, 45° (E) 2_0.15, 45° (F) 6_0.15, 45°

FIGURE 4.18: Contour of time averaged stream-wise vorticity $\omega_x = \pm 0.5$ for the normal, 2_0.15 and 6_0.15 cylinders at $\alpha = 0°$ and $\alpha = 45°$. Red color indicates the positive vorticity and blue color negative vorticity.

and C_l as shown in Fig. 4.2. Occasionally, inclined alignment of the vortices, as indicated by the yellow arrows in the first and third frames, could be observed to be transported by the inclined flow at a $45°$ angle. Overall, the Kármán vortex shedding could be better suppressed by this long-wavelength cylinder even in the inclined cases.

Previous researches have attributed the flow control effectiveness of the wavy cylinders to the additional streamwise vortices (ω_x) that adhere to the near wake (Lam and Lin, 2009; Lin et al., 2016). It is surmised that the spanwise periodic positive and negative streamwise vortices ω_x could stabilize the shear layers to a great extent and thus retard their rolling up into the mature Kármán vortices. Fig. 4.18 presents the stream-wise vorticity calculated from the time-averaged velocity fields for selected cases. In the $\alpha = 0°$ cases, the spanwise periodic arrangement of the positive and negative vortices are clearly

depicted for the wavy cylinders, while for the normal cylinder such vortical structures could hardly be observed owing to the canceling effect in the time-averaging process. However, when it comes to the inclined cases, the strong zig-zag arrangement of ω_x no longer exists in near wakes of the wavy cylinders. Instead, the wake of the $2\_0.15$ wavy cylinder have come to be dominated overwhelmingly by the streamwise vortices of the same sign, which seem to smooth out the spanwise undulation of the geometry. Thus, the vortex suppression efficacy of the wavy cylinders is lessened and they shed Kármán vortices just like the normal cylinder does. The wake of the $6\_0.15$ cylinder, however, is still decorated with some opposite-signed vortices at further downstream. This may help to disrupt the formation of the Kármán vortex shedding even in the inclined situation.

4.7 Summary

Large eddy simulations have been conducted to study the flow over the inclined wavy cylinders at $Re = 5000$. Three angles, 0°, 30° and 45°, together with 2×2 combinations of geometry parameters, namely $\lambda/D_m = 2$ and 6, $a/D_m = 0.1$ and 0.15, have been taken into consideration. In addition, the normal cylinder has also been included for the comparison purpose. The simulation results are interpreted from various aspects such as the spatial-temporal force distribution, span-wise correlation, mean wake properties, surface flow topology, three dimensional vortical structures, etc. The main conclusions in the current research are summarized as follows.

1. The wavy cylinders are confirmed to exhibit satisfactory flow control efficacy compared with the normal cylinder. However, as the additional span-wise velocity sets in, the beneficial effect is lessened. This is reflected in the significant surge in the drag and lift coefficients, shrinkage of the vortex formation length as well as the decrease in the base pressure coefficients. Particularly, in the case of the $2\_0.15$ wavy cylinder, the Kármán instability that is totally suppressed at $\alpha = 0^\circ$ recurs in the inclined cases. Generally speaking, the flow control performance of the long-wavelength cylinders is better than the short-wavelength ones in the presence of U_z.

2. Along with the surge in the averaged C_d and C_l, the differences between the sectional values in the vicinity of the node and saddle planes also grow larger with α. The maximum drag coefficient, which occurs at the node plane in the zero incidence case, shifts slightly to the lower part of the node at which the inclined incoming flow attacks the local surface normally. While the increase in the mean drag is attributed to the decreased base pressure, the variation in the sectional drag coefficient is found to be largely affected by the stagnation pressure.

3. A quantitative evaluation of the lift correlation has been realized by plotting the averaged correlation coefficients against the spanwise separation. A monotonic decrease in the span-wise uniformity is observed for the normal cylinder subjected to the increasing α, whereas the correlation is generally enhanced for the wavy cylinders in the inclined cases. This is owing to the intensified vortex shedding process in the inclined wavy cylinders taking over the effect of the random turbulence on the lift coefficients.

4. The mean surface flow topology reveals intricate boundary layer separation structure in the $2\_0.15$ wavy cylinder. Such structure is milder in the $6\_0.15$ case. The chaotic rear surface flow in the zero angle cases could be regulated by the secondary axial flow to maintain symmetry with respect to the x-z plane. Instantaneous vortical structures are visualized by the Q criterion. Clear recurrence of the Kármán vortex shedding is found in the $2\_0.15$ case as α increase from 0° to 45°. The wake remains orderless in the $6\_0.15$

cylinder regardless of the inclination angle. The disappearance of the zig-zag arrangement of the positive and negative ω_z is believed to result in the cessation of the flow control efficacy in the inclined cases.

Chapter 5

Flow-induced Vibration of Wavy Cylinders

5.1 Case setup

In this chapter, we carry out numerical simulations to study the aero-elastic properties of the wavy cylinder. As is shown in Fig. 5.1, the wavy cylinder of mass m is mounted on a spring-damping system with stiffness k and damping c in the transverse (y) direction. The geometric parameter for the current wavy cylinder is $\lambda/D_m = 2$ and $a/D_m = 0.175$. The Reynolds number is kept at 5000. The reduced velocity, defined as $U_r = U_\infty/(f_n D_m)$, is considered as the only varying parameter in most of this chapter. Unlike the scenario in the experiments, where the freestream velocity U_∞ is usually varied, we modify the reduced velocity by change the stiffness k of the spring, which consequently set the value of the natural frequency of the cylinder via the relationship $f_n = \sqrt{k/m}/(2\pi)$. The mass ratio of the cylinder, $m^* = 4m/\left(\rho\pi D_M^2\right)$ is fixed at 2.55. In this way, the effect of Reynolds number and mass ratio to the VIV response could be eliminated. Unless otherwise specified, the structural damping c is set to zero to encourage maximum vibration amplitude. The performance of the wavy cylinder is evaluated based on the comparison with the normal cylinder with identical fluid and structural parameters. In this regard, the present work also contributes to the database of numerical prediction of the normal cylinder's VIV at moderate Reynolds number.

The aspect ratio, i.e., length-to-diameter ratio, $L/D = 4$ is chosen for the normal and wavy cylinder. Although higher values of aspect ratio is preferred in predicting the flow properties especially the span-wise correlation, as we have adopted in Chapter 4, for current case it would resulted enormous increase in the consumption of the computational resources. Actually, according to Lei, Cheng, and Kavanagh (2001), good agreement of force coefficients and Strouhal number with experimental data could be achieved with span-wise length above twice the cylinder diameter. As for the wavy cylinder, $L/D = 4$ accommodates two wavelengths. It was revealed that one wavelength height is sufficient for the simulations regardless of whether the flow is laminar (Lam and Lin, 2009) or turbulent (Lam and Lin, 2008). Based on the above statements, the currently chosen aspect ratio should ensure fairly accurate results of the force coefficients and the VIV responses. The mesh resolution employed in this work is similar to what we have introduced in section 4.1. An independent mesh dependency test, as will be shown in section **??**, have been conducted to confirm the adequacy of the mesh to the dynamic cases.

5.2 Force mitigation of the static wavy cylinder

Before we proceed to present

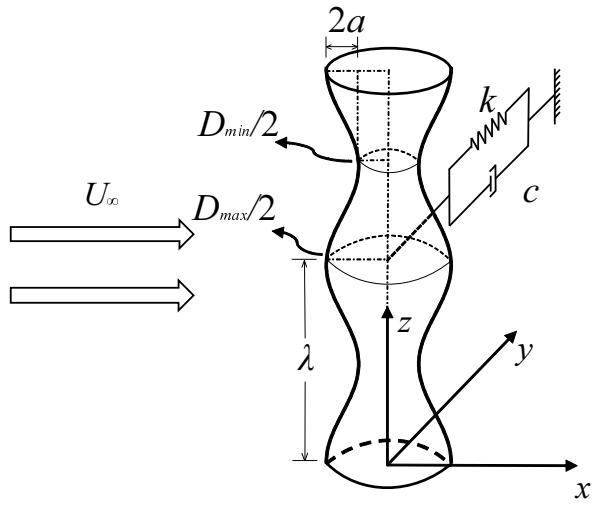

FIGURE 5.1: Schematic of the setup for vortex-induced vibration

TABLE 5.1: Drag, lift force coefficients and Strouhal number at different Reynolds number in the static configuration

Re	C_d		C_l		St	
	normal	wavy	normal	wavy	normal	wavy
1000	1.06	0.85	0.18	0.010	0.21	-
3000	0.97	0.82	0.093	0.011	0.21	-
5000	0.95	0.80	0.075	0.013	0.21	-

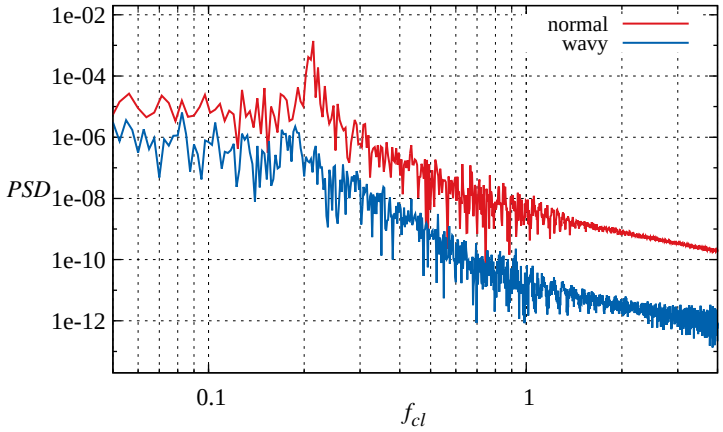

FIGURE 5.2: Power spectrum of lift force coefficients of normal and wavy cylinders at $Re = 5000$

The drag, lift force coefficients and the Strouhal number of both the normal and wavy cylinders are summarized in Table 5.1 at three subcritical Reynolds numbers, i.e., $Re = 1000, 3000$ and 5000. The same mesh as $Re = 5000$ case is used for the simulations with the other two Reynolds numbers. Compared with the normal cylinder, the wavy cylinder presents around 15% to 20% reduction in the drag force coefficients. The mitigation in the lift coefficient is even more pronounced, ranging from 83% to 95%. In addition, the shedding frequency of the Kármán vortices behind the wavy cylinders at the tested three Res could not be detected. This is manifested in Fig. 5.2, where the PSD

of the lift coefficients of the normal and wavy cylinders at $Re = 5000$ are presented. The other two Reynolds numbers are not shown here since the behavior of the lift spectrum is similar. It could be observed that the PSD of the normal cylinder is characterized by a sharp peak at the vortex shedding frequency $f_{cl} = 0.21$. However, such a well-marked vortex shedding frequency is not recognizable for the wavy cylinder, rather, its frequency distribution resembles white noise for $f_{cl} < 0.2$. The absence of the primary frequency in the PSD of C_l indicates that the vortex shedding has been massively suppressed. This is further supported by the two snapshots of axial vorticity ω_z contour, as are presented in Fig. 5.3. For the normal cylinder, well-formed Kármán vortex loops are clearly displayed. However, in the case of wavy cylinder, the free shear layers are distorted and roll up at much further wake than the normal one, and the developed vortices appear rather irregular. The detected small-amplitude lift force might be attributed to the 3-dimensional turbulence effect that is inherent in the cylinder wake at $Re = 5000$.

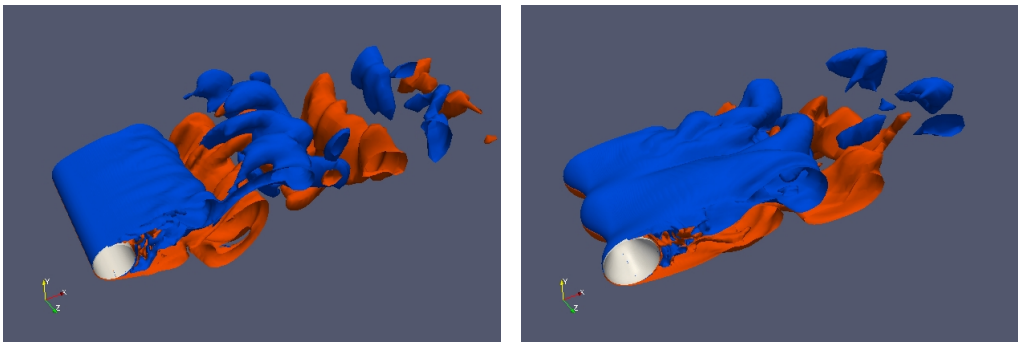

(A) Normal cylinder (B) Wavy cylinder

FIGURE 5.3: Contour of $\omega_z = \pm 0.5$ of the static normal and wavy cylinders at $Re = 5000$

5.3 Dynamic response

The vortex induced vibration responses in terms of both maximum amplitude and primary frequency of the current study are plotted against the reduced velocity in Fig. 5.4, together with the data from the experimental works of Khalak and Williamson (1996) and Khalak and Williamson (1997) ($m^* = 2.4$, $Re = 2000 \sim 12000$), Stappenbelt, Lalji, and Tan (2007) ($m^* = 2.36$, subcritical Re) and the numerical investigation from Zhao et al. (2014) ($m^* = 2$, $Re = 1000$). Efforts are made to convert some of the cited data that are based on the natural frequency in water f_{nw} to f_n. Although the resolution of reduced velocities in the current study is not fine enough to delineate the detailed boundaries between different response regions, the vibration amplitude variation obtained from our numerical simulation fits aptly to the classical initial-upper-lower branch type curve (Khalak and Williamson, 1999), and as far as the normal cylinder is concerned, good agreement is achieved between our simulation with the literature. The maximum displacement predicted by the current work occurs at $U_r = 5$ and is around 0.98, which is close to the experiment of Khalak and Williamson (1996) and much larger than the DNS of Zhao et al. (2014) at $Re = 1000$. This proves VIV's dependency on the Reynolds number. The lower branch is characterized by a plateau with almost constant amplitude of around 0.6 persisting within $U_r = 7 \sim 10$. At the same range the reduced frequency f/f_n locks to a value slightly larger than 1, indicating that rather than following the Strouhal law as in the lower reduced velocity regimes, the vibration has come to be dominated by the

structural frequency. The slight deviation from unity of the frequency ratio is a result of the added mass effect (Khalak and Williamson, 1999).

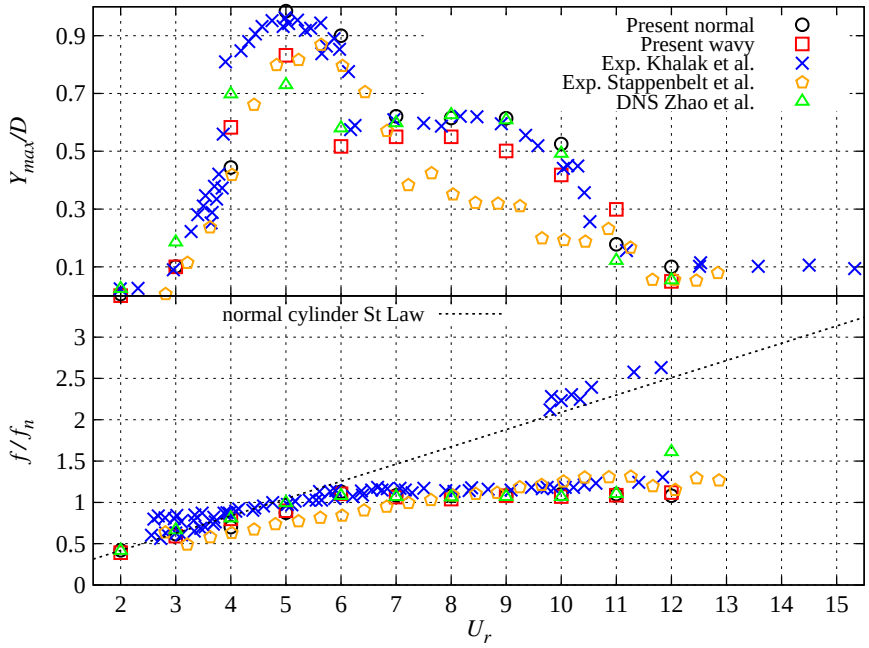

FIGURE 5.4: VIV response of normal and wavy cylinders, with data from literature

The wavy cylinder exhibits a similar response curve as the normal cylinder, with noticeably smaller vibration amplitude at most of the simulated reduced velocities. At $U_r = 5$, where the maximum oscillation occurs, a 15% reduction in amplitude compared with the normal cylinder could be discerned. Compared to the largely suppressed lift force when it's fixed, wavy cylinder's performance in alleviating vortex induced vibration could be concluded disappointing. Large amplitude vibrations still occur within quite a lrage range of reduced velocities. Frequency-wise, the reduced frequency of the wavy cylinder almost overlap with the normal cylinder at the synchronization range. It is surprising to find such coincidence in the response curves of the wavy and normal cylinders, since the former does not have a leading shedding frequency, as is revealed in Fig. 5.2. Thus, it might experience vigorous VIV at some reduced velocities other than 5. We believe that the occurrence of this coincidence might not be fortuitous. As a matter of fact, it has been revealed by previous studies (Lam et al., 2004; Zhang et al., 2016) that even though the vortex shedding intensity is reduced by the wavy cylinder, the frequency of the mitigated lift force remains nearly the same with the normal cylinder. In the current case, the primary shedding frequency of the wavy cylinder has been suppressed to such a level that is not able to be detected. It seems that flexible mounting unveils the concealed primary frequency, which then plays its role in determining the vibration response.

To further check the Reynolds number dependence of the wavy cylinders' dynamic characteristics, the maximum vibration amplitude and the normalized frequency at $Re = 1000$ and 3000 are also included in Fig. 5.4 at $U_r = 3$, 4, 5 and 7. Except that at $Re = 1000$ the largest vibration of the normal cylinder occurs at $U_r = 4$ rather than 5, the responses of both the normal and wavy cylinders resemble each other with minor difference in the values, and the initial, upper and lower branches could also be vaguely discerned from the amplitude plot. The frequency responses of the normal and wavy cylinders at the said two Res are also very close to each other. No significant difference could

be observed in the vibration amplitude at the said two Reynolds numbers compared to $Re = 5000$, although the largest vibration amplitude occurring at $U_r = 5$ or 4 decreases as the Reynolds number decreases, which is in accordance with the result of Lucor, Foo, and Karniadakis (2005). This fact suggests that the different flow control behavior of the wavy cylinder at fixed and flexibly mounted configurations is associated with a large range of Reynolds numbers. Since at the three test Reynolds numbers the vibration responses appear qualitatively similar, in the texts that follow, only the results of case $Re = 5000$ will be presented.

5.4 Force coefficients

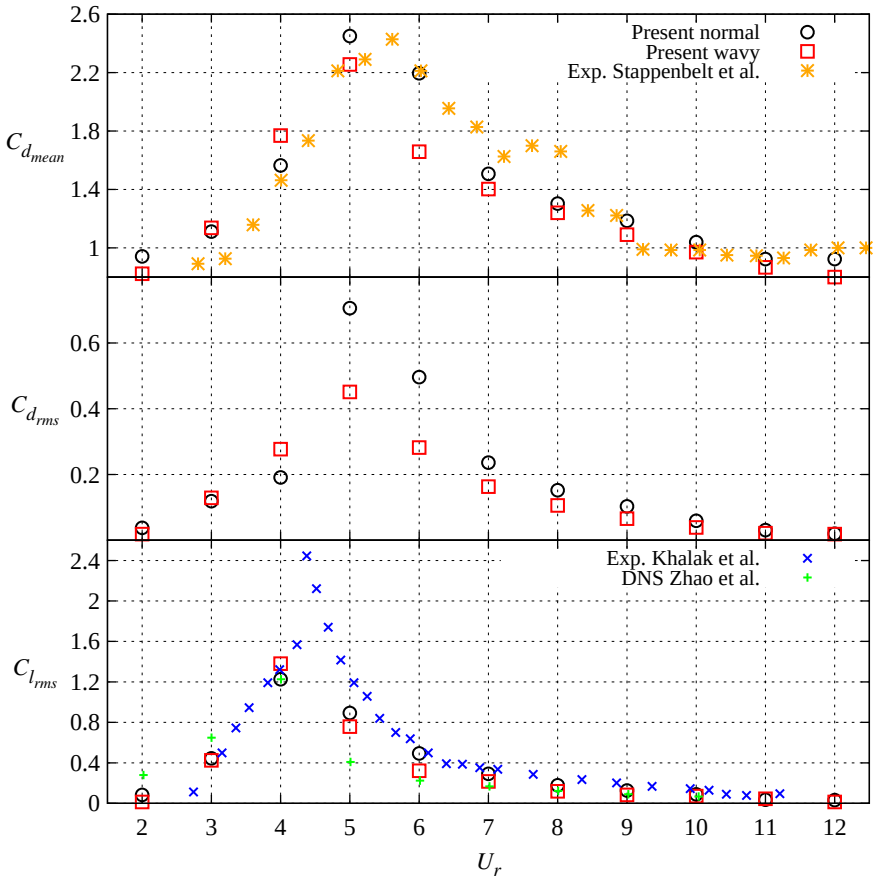

FIGURE 5.5: Mean drag, rms drag and lift coefficients

The span-wise averaged mean drag and rms lift coefficients are summarized in Fig. 5.5. Experimental data from Stappenbelt et al. Stappenbelt, Lalji, and Tan, 2007, Khalak and Williamson Khalak and Williamson, 1999 and numerical study from Zhao et al. Zhao et al., 2014 are also included in the figure for comparison. Although the motion of the cylinder mainly couples with the lift force, a significant amplification of drag is seen in both the mean value and its fluctuation during the lock-in range. The mean C_d predicted by our simulations is in considerably good agreement with the experiment of Stappenbelt et al. Stappenbelt, Lalji, and Tan, 2007. For the normal cylinder, the mean C_d reaches a peak of around 2.4 at $U_r = 5$, at which its fluctuation also maximizes. This corresponds to maximum instantaneous C_d of around 4, which is four times larger than a fixed cylinder. The mean and fluctuation C_d of the wavy cylinder are generally smaller

than that of the normal cylinder. The maximum instantaneous C_d occurring at $U_r = 5$ of the wavy cylinder is around 3, which is also approximately four times larger than the fixed configuration.

As far as the rms lift coefficients are concerned, the discrepancy between the wavy and normal cylinders at each reduced velocity is minor. Both $C_{l_{rms}}$ go through massive magnification during the synchronization. Our numerically predicted maximum rms C_l, which occurs at $U_r = 4$, agrees well with the DNS of Zhao et al. Zhao et al., 2014, but falls far short of the experimental investigation by Khalak and Williamson Khalak and Williamson, 1999 occurring at $U_r = 4.4$. It is highly likely that, as noted by Zhao et al. Zhao et al., 2014, the rms lift coefficient may reach a peak between $U_r = 4 \sim 5$ if the simulation in the said range were conducted with smaller reduced velocity intervals.

Moreover, the span-wise distributions of the sectional temporally averaged drag and the rms lift force coefficients are presented in Fig. 5.6. The sectional coefficients are defined based on the local diameters, i.e., by replacing the average diameter D_m. Previous studies have shown that in the static configuration, the sectional drag force coefficient C_d at the geometric nodes is greater than that at the geometric saddle, while there is not much variation in the sectional lift force coefficient C_l in the span-wise direction Ahmed and Bays-Muchmore, 1992; Zhang et al., 2016. These conclusions are generally true for the current work when the wavy cylinder is static, except that the C_d reaches the minimum in between the node and saddle section. This could be attributed to the large geometric gradient at the middle sections (where $D(z) = D_m$). The force coefficients are actually calculated as $C_i = \Sigma C_p \cdot n_i \cdot A$, where $i = x, y$ or z denotes the Cartesian coordinate, n_i is the i component of the surface normal unit vector, for which the identity $n_x^2 + n_y^2 + n_z^2 = 1$ holds, C_p is the pressure coefficient defined as $C_p = 2(p - p_\infty)/\rho U^2$ and A is the surface area that is proportional to the local radius of the cylinder. In the middle section, the span-wise geometric gradient is as large as $n_z = 0.5 \times dD(z)/dz|_{0.5} = 0.55$. It consumes quite a portion of the unit vector, yielding smaller values of n_x and n_y. Although the integration area A at the middle section is greater than the saddle, this effect is offset by the massive decreases in the values of n_x and n_y, the minimum values of the force coefficients at the middle section are thus engendered.

The motions of the wavy cylinders influence the sectional forces differently depending on the U_r. Apart from the increased values, the undulations in the span-wise distributions of the sectional force coefficients are slightly exaggerated at most of the reduced velocities. This is particularly true for the lift coefficients as span-wise variations, with maximum at the node and minimum at the saddle, has come to be noticeable in Fig. 5.6b. However, compared to the $C_{d_{mean}}$, these span-wise fluctuations in the lift coefficients are still insignificant. Glaring exceptions are observed at $U_r = 4$ and 5, at which the drag coefficients at the saddle exceed that at the node. The same conclusion also holds for the lift coefficients, although their minimum values are found at the middle sections at the said two reduced velocities. As is recorded in Fig. 5.4, both reduced velocities correspond to the top two maximum vibration amplitude, which is thought to be responsible for the observed abnormality. This is confirmed by an additional case with structural damping $c = 4.8$ at $U_r = 5$, denoted as $Ur5\_c4.8$ in Fig. 5.6. In this case, the vibration amplitude has been suppressed to $0.3D$. It could be observed in the damped case that the force coefficients at the saddle has been suppressed to be lower than that at the node. More detailed results about the cases with non-zero damping will be presented in Section 5.6.

The span-wise correlation of the lift force serves as an accurate measurement of the three dimensionality in the near wake of the body. Bearman (1984) noted that the correlation length experiences a significant increase when the oscillation magnitude exceeds $Y_{max}/D = 0.05$. However, more recent studies indicated that there exists certain ranges in the lock-in region where the span-wise correlation suffers severe drop (Lucor, Foo,

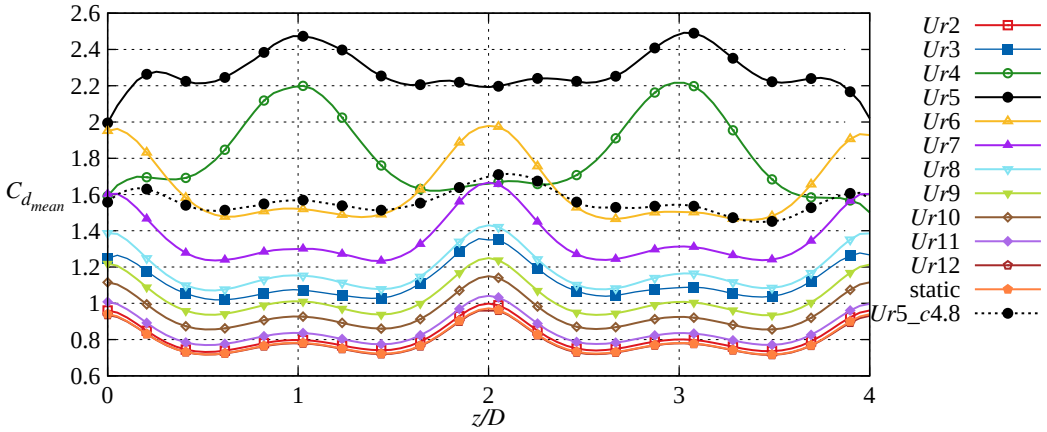

(A) Time-averaged sectional drag force coefficient $C_{d_{mean}}$

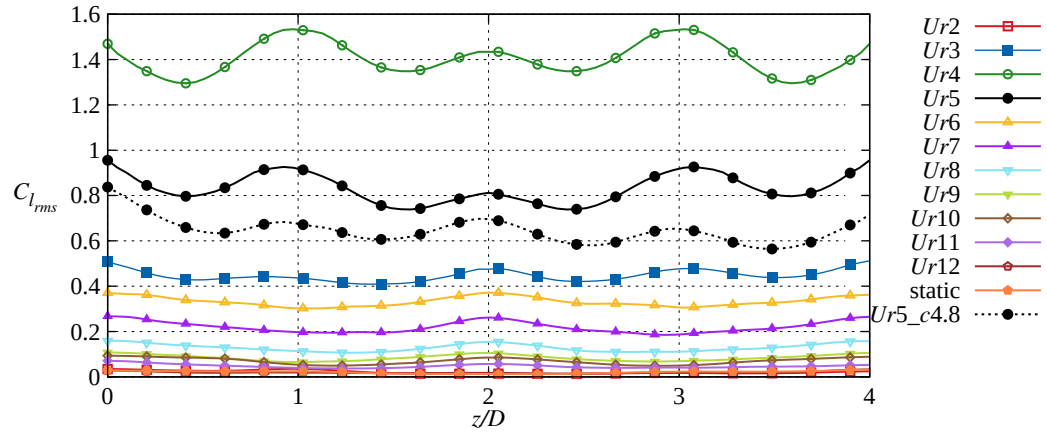

(B) rms sectional lift force coefficient $C_{l_{rms}}$

FIGURE 5.6: Span-wise distribution of the mean drag and the rms lift force coefficients

and Karniadakis, 2005; Zhao et al., 2014; Hover, Techet, and Triantafyllou, 1998; Hover, Davis, and Triantafyllou, 2004). In the current work, we define the correlation coefficient of the lift force coefficients as follows:

$$r\left(0,z\right)=\frac{\sum\limits_{t=0}\left\{\left[C_l\left(0,t\right)-\overline{C_l\left(0\right)}\right]\left[C_l\left(z,t\right)-\overline{C_l\left(z\right)}\right]\right\}}{\sqrt{\sum\limits_{t=0}\left[C_l\left(0,t\right)-\overline{C_l\left(0\right)}\right]^2}\sqrt{\sum\limits_{t=0}\left[C_l\left(z,t\right)-\overline{C_l\left(z\right)}\right]^2}}, \tag{5.1}$$

in which $C_l\left(z,t\right)$ is the lift force coefficient at span-wise location z and time t, the overline of which is its time-averaged value. Figure 5.7 presents the span-wise correlations at different reduced velocities of both the normal and wavy cylinders. It could be seen in Fig. 5.7a that the lift force of the normal cylinder at $U_r = 3$ and 4, which are in the initial branch, are almost fully correlated. The correlation stays stably high before it drops to minus again at the end of the synchronization range. The above descriptions are generally consistent with the findings of the previous publications that the correlations deteriorate at the ends of the upper and lower branches.

The correlation curves for the wavy cylinder are complicated by the span-wise waviness, as could be observed in Fig. 5.7b. By comparing the static cases of the wavy and

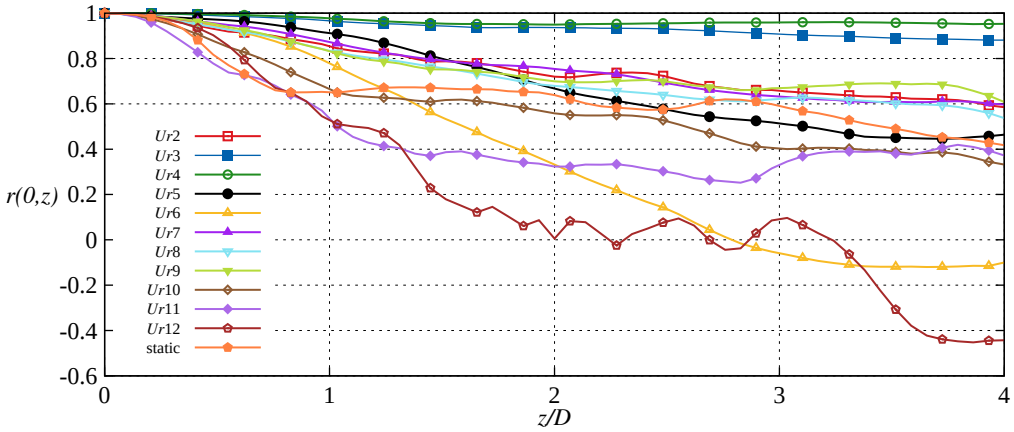

(A) Normal cylinder

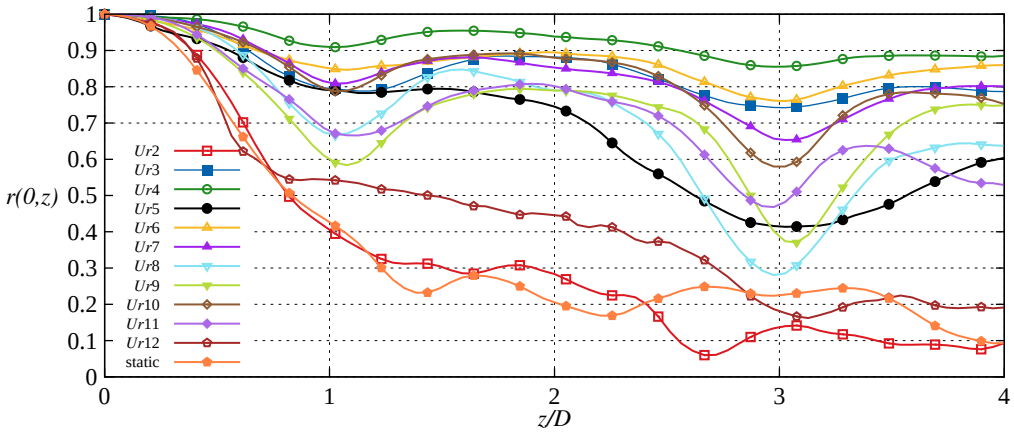

(B) Wavy cylinder

FIGURE 5.7: Span-wise correlation of lift force coefficients of normal and wavy cylinder

normal cylinders, it is revealed that the geometric waviness substantially decreases the span-wise correlation length. However, it is greatly enhanced once the wavy cylinder is excited to vibrate. Another remarked feature is that for most of the reduced velocities, and inclined undulated pattern that conforms to the wavy geometry is displayed. Since we calculate the correlation based on a fixed end node location, a recovery of the coefficient is observed at the other two geometric nodes after the dip at the saddle locations. This is significantly contrasted to the exceptions made at $U_r = 2, 12$ and the static case, in which such undulated patterns are not found. We could infer from this discrepancy that, when the wavy cylinder is static or undergoing small amplitude vibrations, the near wake flow presents high three dimensionality because of the span-wisely protruded shape. When large amplitude oscillation occur, the control of the near wake is taken over by the motion of the structure, as is reflected by the coherence between the geometry and the correlation curves. The poorly correlated region at the end of the upper branch found in the normal cylinder is not detected for the wavy one. Again, we attribute this to the coarse resolution of the reduced velocity.

The decreased span-wise correlation length has been considered to contribute favorably to the suppression of the vortex induced vibrations of the straked cylinder (Zhou et al., 2011; Constantinides and Oakley, 2006; Korkischko et al., 2007), which are used widely in the engineering applications (Kumar, Sohn, and Gowda, 2008). In our study

of the wavy cylinders, the deteriorated correlation is also manifested in the static case, although it clearly fails to suppress the oscillations as the reduced velocity enters the lock-in region. Thus, it seems to be problematic to universally regard the decreased axial correlation as an indicator of a successful attempt of VIV mitigation. As a matter of fact, the reduced correlations are resulted from different mechanisms in the two cases. In the straked cylinder, the helical add-ons chop up the flow and the vortex dislocations occur along the cylinder. This leads to irregular shedding of the shear layers and consequently annihilation of the conventional Kármán vortices. While for the wavy cylinder, the lift force is quite small and its primary frequency is missing. As mentioned in Section **??**, it is likely that the deteriorated lift coefficient correlation is a result of the unsteady turbulence effect. Albeit contorted in a 3-dimensional fashion, the shear layers emanated from the wavy cylinder are well-organized. As the initial disturbance in the cylinder motion is introduced, the efficacy of the 3-dimensional shear layer in stabilizing the wake is lost. Rather, the shear layers interact with each other in a way that is similar to the normal cylinder, large amplitude of vibration is thus engendered.

5.5 Phase and vortex modes

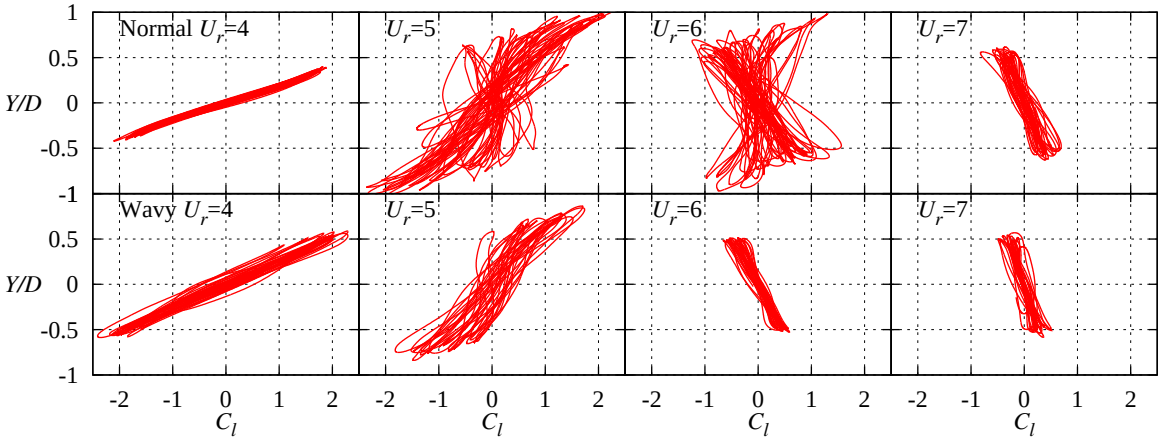

FIGURE 5.8: Variation in the phase portrait of the lift force coefficient, C_l, relative to the transverse vibration amplitude, Y/D of the normal (first row) and wavy (second row) cylinders.

The Lissajous plots of the lift force coefficient and transverse vibration amplitude at $U_r = 4 \sim 7$ are presented in Fig. 5.8 to identify the relative phase lags in different branches. Judging from the shapes of these phase portraits, a clear change of relative phase angle from nearly 0 o nearly 180 ould be noticed between the initial branch of $U_r = 4$ and the lower branch of $U_r = 7$, in both the normal and wavy cylinders. The phase diagrams of the normal cylinder at the $U_r = 5$ and 6 are characterized by significantly larger vibration amplitude and appear less organized than the other two branches. This chaotic behavior suggests that different states reside in this regime and intermingle with each other. The phase portrait of the wavy cylinder at $U_r = 5$, however, does not exhibit such phenomenon. It is revealed by Khalak and Williamson (1999) that while the initial-upper transition is hysteric, the upper-lower transition is associated with intermittent switches between the upper and lower branches. Navrose and Mittal (2013) also confirmed this unstable phenomenon via CFD simulations. A deeper knowledge of this behavior is provided by the instantaneous phase lag between the lift and displacement as well as the frequency, which could be obtained by performing the Hilbert transformation

to the recorded time histories of the lift force and displacement. For a signal $s(t)$, given its Hilbert transform $\hat{s}(t)$, the analytic signal is defined as:

$$s_A(t) = s(t) + j\hat{s}(t) = A(t)\, e^{j\phi(t)}, \tag{5.2}$$

in which $\phi(t)$ is the instantaneous phase. The instantaneous frequency could be obtained as

$$f(t) = \frac{1}{2\pi}\frac{d\phi(t)}{dt}. \tag{5.3}$$

One may refer to the work of Khalak and Williamson (1999) for further details on this technique. Fig. 5.9 shows the time histories of the lift coefficient, displacement, phase angle and frequency. At $U_r = 5$ (Fig. 5.9a), most of the time is spent with the upper branch, as is evidenced by the in-phase lift and displacement. Phase jump is only observed at very small portion of time, e.g., $t \approx 50$ and 160. The instantaneous frequency at this U_r is quite stable, even in the presence of the phase jump. The variation of the phase angle $\phi(t)$ becomes quite drastic when it comes to $U_r = 6$. Phase jumps are discerned all along the time span. The time spent on the upper branch is comparable with that of on the lower branch. Moreover, together with the jump in $\phi(t)$, the instantaneous frequency also undergo a sudden shift. The upper branch is associated with lower frequency and at the lower branch the frequency is higher.

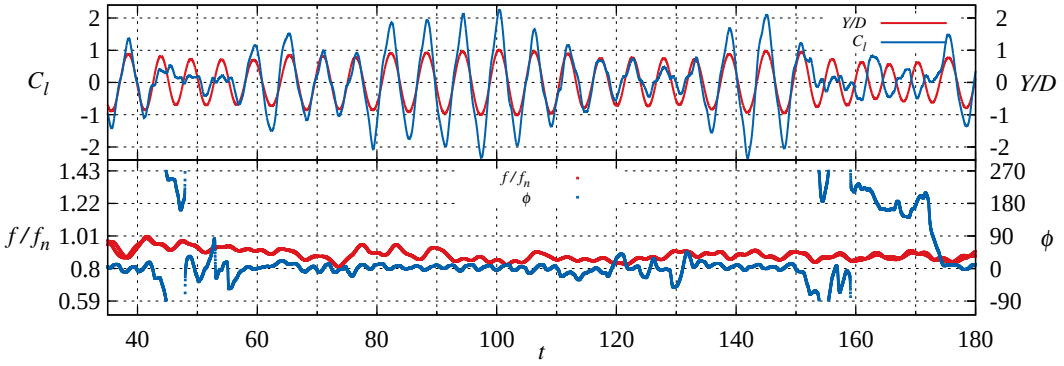

(A) $U_r = 5$

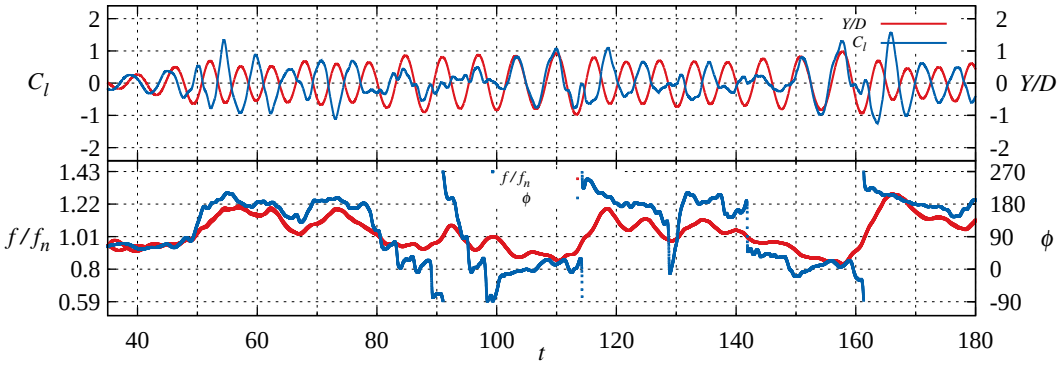

(B) $U_r = 6$

FIGURE 5.9: Instantaneous lift force coefficient, displacement, frequency and phase angle of the normal cylinder at $U_r = 5$ and 6.

It is generally known that the different response branches are associated with different vortex shedding patterns (Govardhan and Williamson, 2000). While the initial branch corresponds to the $2S$ mode (two single vortices per cycle), in the lower branch two pairs of vortices shed in each cycle, forming the $2P$ mode. The shedding mode for the upper

branch seems to be dependent on the Reynolds number. Govardhan and Williamson (2000) identified the $2P$ mode at $Re \approx 3100$. However, $2S$ mode is found at $Re = 1000$ in the numerical study by Navrose and Mittal (2013). Moreover, Zhao et al. (2014) observed at $Re = 1000$ that the two modes coexist in the span-wise direction. In the current study, the axial component of the vorticity fields ω_z are plotted in Fig. 5.10 and 5.11 in an attempt to confirm the vortex shedding patterns. As expected, the vortices behind the the normal cylinder shed in the $2S$ mode in the initial branch ($U_r = 4$) and $2P$ mode in the lower branch ($U_r = 7$). The upper branch ($U_r = 5$) is observed to be dominated by the $2P$ mode at $Re = 5000$. This is in agreement with the work of Govardhan and Williamson (2000) at higher Re and at variance with Navrose and Mittal (2013) at lower Re. In the upper-lower transition regime ($U_r = 6$), there exists significant span-wise variation in the shape of the vorticity contour, which undermines the clear inspection of the shedding mode. This also corroborates the deteriorated correlation of the lift forces, as is shown in Fig. 5.7a. As for the wavy cylinder, the vortex shedding patterns are in general consistent with the normal cylinder. The $2S$ and $2P$ modes could be clearly observed at the initial ($U_r = 4$) and lower branch ($U_r = 6$ and 7). However, at the upper branch ($U_r = 5$), in contrast to the well-organized vortex loops that are observed at the other reduced velocities, the wake is dominated by many small-scale irregular vortices, and the shedding mode can not be clearly identified.

5.6 The effect of structural damping

TABLE 5.2: VIV responses with additional structural damping

$m^*\zeta$	Case	Y_{max}/D	$C_{d_{mean}}$	$C_{l_{rms}}$
0	normal	0.98	2.45	0.89
0	wavy	0.83	2.26	0.76
0.61	normal	0.39	1.74	0.80
0.61	wavy	0.30	1.64	0.63
0.91	normal	0.25	1.39	0.64
0.91	wavy	0.012	0.86	0.030

Additional simulations are conducted with non-zero structural damping, i.e., $c \neq 0$, at $U_r = 5$, at which the maximum vibration amplitude is observed for both the normal and wavy cylinders without damping. The damping coefficient is defined as $\zeta = c/\left(2\pi\sqrt{mk}\right)$. The results are shown in Table 5.2. Although only the damping is varied, the combined mass-damping parameter $m^*\zeta$ is used since it has been proven useful in collapsing the peak vibration amplitudes (Khalak and Williamson, 1999; Griffin, 1980; Bahmani and Akbari, 2010). It could be seen that as the damping reaches a medium level at $m^*\zeta = 0.61$, although the three indicators ($Y_{max}/D, C_{d_{mean}}$ and $C_{l_{rms}}$) of wavy cylinder are smaller than the normal cylinder, the extent of reduction remains at the same level as the zero-damping case. However, with further increase of the damping ratio ($m^*\zeta = 0.91$), the vortex induced vibration of the wavy cylinder has shown to be almost eliminated, together with massively mitigated drag and lift force coefficients. At the same value of damping, the normal cylinder still experiences oscillations with considerable amplitude. This is in agreement with the finding of Owen, Bearman, and Szewczyk (2001), who devised the cylinders with wavy axis and with helical bumps in attempt to reduce the hydrodynamic forces as well as VIV. In their work, a significant decrease in the vibration amplitude was observed as the mass-damping parameter reaches around 0.8.

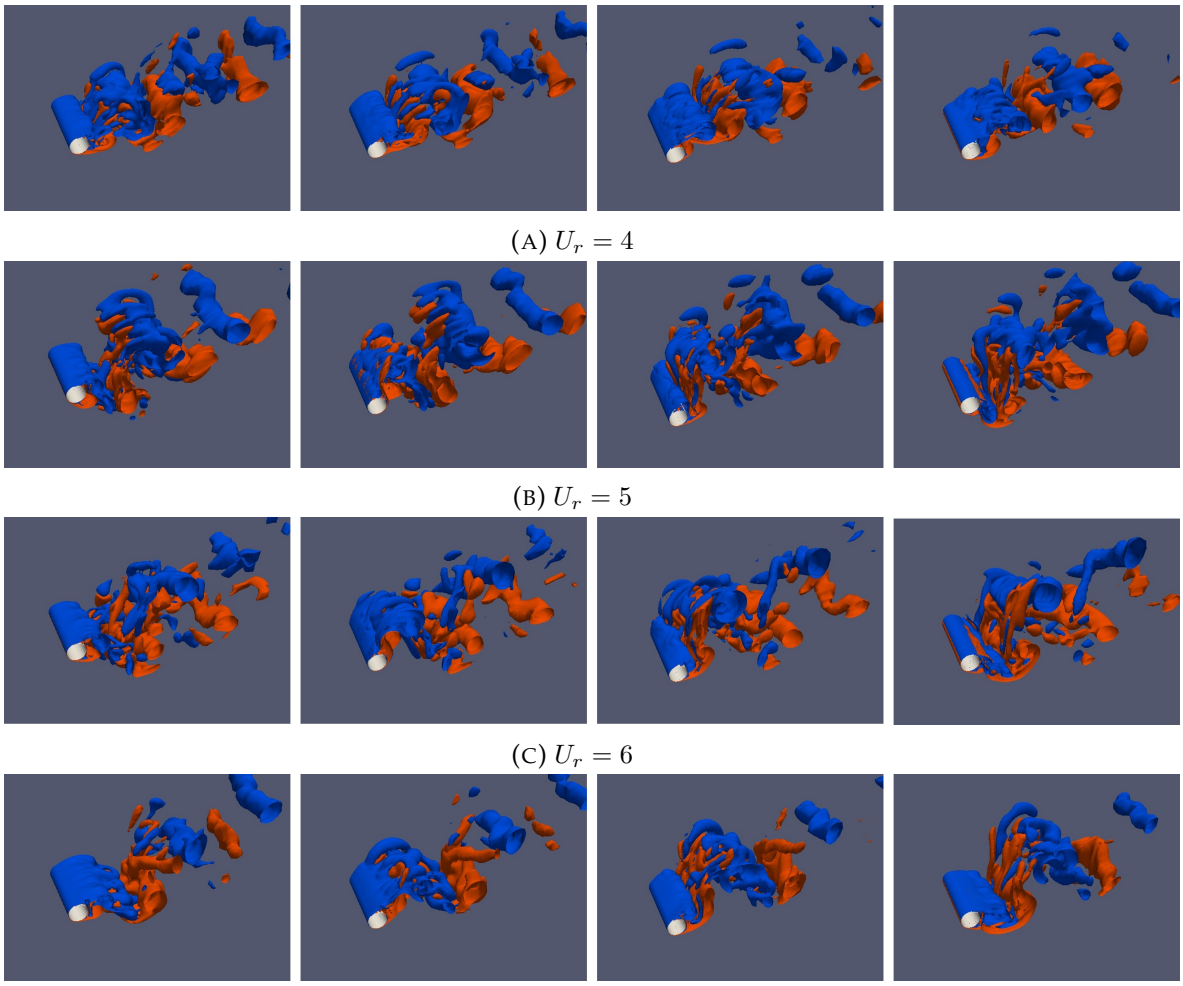

(A) $U_r = 4$

(B) $U_r = 5$

(C) $U_r = 6$

(D) $U_r = 7$

FIGURE 5.10: Contours of span-wise component of vorticity $\omega_z = \pm 0.5$ for the normal cylinder. The four time instants the each U_r correspond to the cylinder at positive maximum position, the middle position with downward motion, the negative maximum position, the middle position with upward motion. For $U_r = 5$ and 6, the snapshots are selected in the time periods that the displacement is in and out of phase with the lift forces, respectively. The blue color represents the minus value of ω_z and the orange color represents the positive value.

Although only $U_r = 5$, rather than the whole reduced velocity spectrum is investigated, we cautiously conclude that the wavy cylinder could be used as a low VIV-responsive device if sufficient damping is supplied. Additionally, it is surmised, based on the validity of the mass-damping parameter in predicting the maximum response amplitude, that the wavy cylinders with larger mass ration, such as the case of the cable in air, might show better performance in mitigation of the VIV than the normal cylinder. Further researches are under consideration to verify this conjecture.

5.7 A perspective from the forced vibration test

Forced vibration tests have been useful in predicting and interpreting the free vibrations, as have been introduced in section 2.1.3. For the normal cylinder under forced vibration,

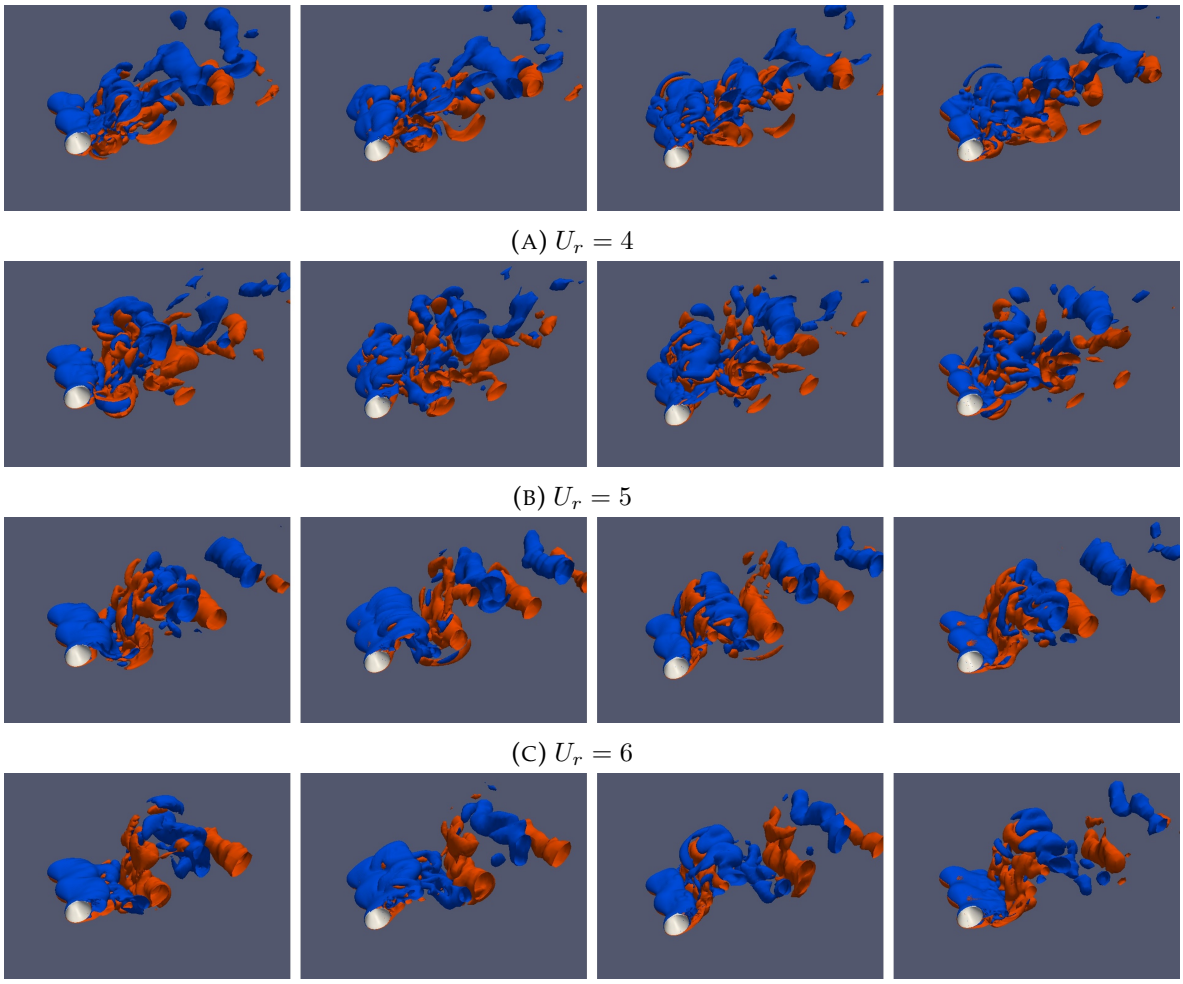

(A) $U_r = 4$

(B) $U_r = 5$

(C) $U_r = 6$

(D) $U_r = 7$

FIGURE 5.11: Contours of span-wise component of vorticity $\omega_z = \pm 0.5$ for the wavy cylinder. The four time instants are the same with Fig. 5.10.

the interaction of between the external forcing frequency and the inherent vortex shedding frequency could lead to complicated phenomenon such as frequency modulation, lock-in, etc. However, in the case of the wavy cylinder, the vortex shedding has been completely suppressed, leaving only the external frequency in the system. It intrigues us to know how would the wake of the wavy cylinder respond to the external forcing with different frequencies.

In this section, the cylinders are given a prescribed sinusoidal motion in the transverse direction, i.e.,

$$y\left(t\right) = A_{ex} \sin\left(2\pi f_{ex} t\right), \tag{5.4}$$

in which A_{ex} and f_{ex} denote the forcing amplitude and the frequency. In this section, we investigate $A_{ex} = 0.2D_m$ and $f_{ex}D_m/U_\infty = 0.1 \sim 0.3$ with an interval of 0.05. Considering that the Strouhal number for the normal cylinder at $Re = 5000$ is around 0.2, the investigated frequency range should be enough for the lock-in phenomenon to occur.

Fig. 5.12 presents an FFT analysis of the lift coefficients of the forced vibration test for the normal and wavy cylinder. In the case of the normal cylinder, the when the excitation frequency is either too small or too large, the spectrum is characterized by two distinctive peaks, representing the excitation frequency and the inherent vortex shedding frequency. As f_{ex} approaches the Strouhal frequency of 0.2, the peak corresponding to

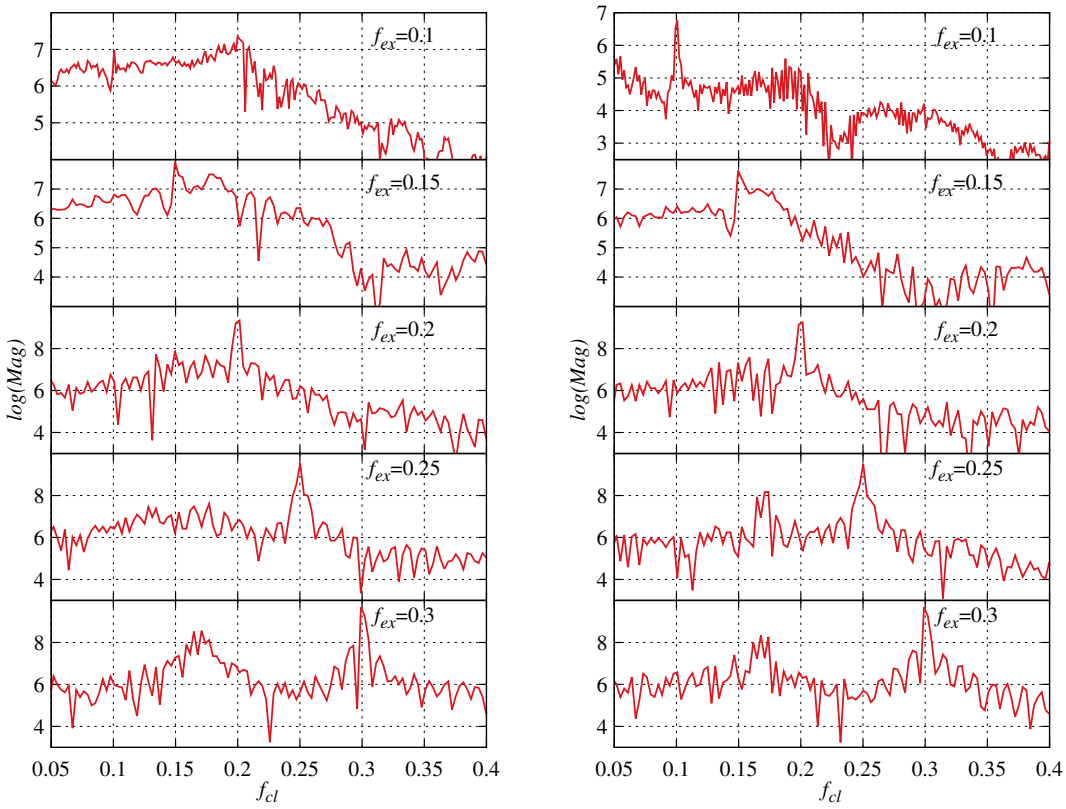

(A) normal cylinder (B) wavy cylinder

FIGURE 5.12: The FFT analysis of the lift force coefficients from the forced vibration test with $A_{ex} = 0.2D_m$.

the Strouhal frequency becomes insignificant and the lift force is dominated by a single frequency at f_{ex}, reproducing the famous lock-in phenomenon in the forced vibration test. As for the wavy cylinder, although the inherent shedding frequency has been effectively suppressed in the fixed configuration as is shown in section 5.2, the two-peak response could still be observed at the two ends of the tested frequencies. Different from the normal cylinder, in which the synchronization region occurs at $f_{ex} = 0.2 \sim 0.25$, the lock-in region shifts to $f_{ex} = 0.15 \sim 0.2$ in the wavy cylinder case. Another point to notice is that in the case of $f_{ex} = 0.1$, an reverse in the relative strength of the Strouhal and excitation frequencies could be observed between the normal and wavy cylinder. This is because at such low frequency the flow control efficacy is less disturbed by the external forcing.

The recurrence of the Strouhal frequency in the oscillating wavy cylinder could be understood further by the coherence of the span-wise lift force coefficients, as are plotted in Fig. 5.13. The magnitude-squared coherence is defined as

$$Coh_{\alpha}\beta\left(f\right) = \frac{\left|P_{\alpha\beta}\right|^2}{P_{\alpha\alpha}\left(f\right)P_{\beta\beta}\left(f\right)}, \tag{5.5}$$

in which $P_{\alpha\beta}$ is the cross power spectral density of two signals and $P_{\alpha\alpha}$ and $P_{\beta\beta}$ are the power spectrum densities of the respective signals. The spectral coherence could be regarded as a measurement of the span-wise correlation of the lift coefficients in the frequency space. At $f_{ex} = 0.1$ and 0.15, high spatial coherence could be observed at the forcing frequency. Another illuminated region, located at around $f_{Cl} \approx 0.2$, could also be

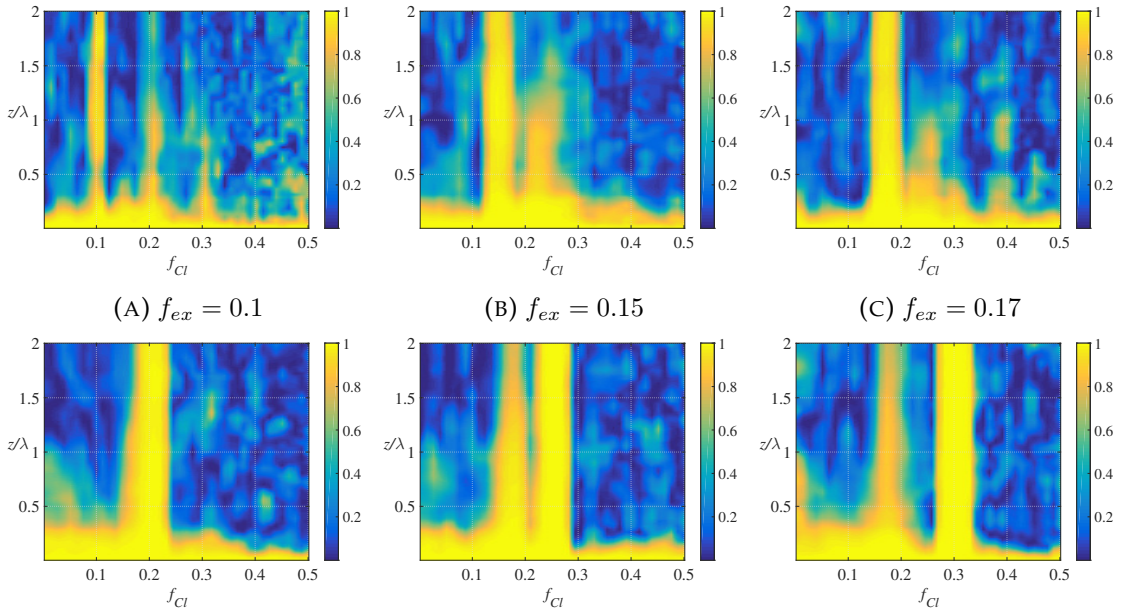

(A) $f_{ex} = 0.1$ (B) $f_{ex} = 0.15$ (C) $f_{ex} = 0.17$

(D) $f_{ex} = 0.2$ (E) $f_{ex} = 0.25$ (F) $f_{ex} = 0.3$

FIGURE 5.13: Spectral coherence of the lift force coefficients of the wavy cylinders undergoing forced oscillation at various forcing frequencies

vaguely recognized. This clearly depicts the resurrection of the Strouhal frequency in the oscillating wavy cylinders. As the forcing frequency increases to $0.17 \sim 0.2$, only a single band possesses high coherence, indicating the occurrence of the frequency lock-in. Further increasing the forcing frequency induces the bifurcation of the two frequencies, with the coherence of the Strouhal frequency strengthened compared with that in the smaller f_{ex} cases. Based on the above observations, it is clear that the Strouhal frequency in the wavy cylinder could be revealed by appropriate external forcing. In the free vibrations, the 'concealed' Strouhal frequency revives and play its role in determining the dynamic responses of the wavy cylinders.

5.8 Summary

A series of numerical simulations have been carried out to study the flow past a spring-mounted wavy cylinder. The aim is to clarify whether this hydrodynamically beneficial geometry is capable of alleviating the flow induced vibrations. We study mainly the Reynolds number of 5000. The stiffness k of the spring is varied to yield $U_r = 2 \sim 12$, at an interval of 1. Another set of computations are carried out for the normal cylinder in order to validate our computational model and serve as the basis upon which the performance of the wavy cylinder could be evaluated. The wavy cylinder studied in the current work exhibits impressive flow control efficacy in the static configuration. The mean drag and the r.m.s lift forces are reduced by 17% and 83% respectively in comparison with the normal cylinder at $Re = 5000$. In addition, no primary frequency is detected in the lift force of the wavy cylinder. This indicates that the Kármán vortices that prevails the wakes of bluff bodies have been almost eliminated by the span-wise waviness. Nevertheless, when the wavy cylinder is allowed to move in the transverse direction, the typical 'lock-in' phenomenon still occurs. Specifically, the main findings of the current work are summarized as follows.

- The vibration amplitude of the wavy cylinder is mitigated compared to the normal one, however, the extent of the mitigation falls far short of that of the lift coefficients in the fixed configuration. The amplitude response (Y_{max}/D vs U_r plot) of both cylinders exhibit the three-branch curve that is typical for low mass-damping cases. The vibration frequency of the wavy and normal cylinders alike locks to the natural frequency of the cylinder in the synchronization range. Similar to the normal cylinder, the maximum vibration amplitude of the wavy cylinder increases with the Reynolds number. However, we observe no qualitative change in the dynamic behavior of the wavy cylinder as the Reynolds number varies from 1000 to 5000.

- For the wavy cylinder, the magnification of the drag and lift forces during the lock-in is comparable with the normal cylinder. The span-wise correlation of the lift force for the wavy cylinder is greatly enhanced once it is excited to vibrate. An undulated pattern, which conforms to the wavy cylinder shape, is found in the C_l correlation curves, in contrast to the monotonic decrease in the correlation of normal cylinder case. The poorly correlated regimes at the end of the upper branch is detected for the normal cylinder, but not for the wavy cylinder.

- Similar with the normal cylinder, the phase between the lift force and the displacement of the wavy cylinder undergoes a change from 0 n the initial and upper branches to 180 n the lower branch. The hysteric regime in between the upper and lower branches in not detected in the wavy cylinder. Different vortex shedding modes are associated with the branches. The initial branch is found to correspond to the $2S$ mode while the upper and lower branches to the $2P$ mode.

- The performance of the normal and wavy cylinders are comparable in the case of small structural damping. However, as enough damping ($m^*\zeta \approx 0.9$) is supplied, the vortex induced vibration could be reduced more efficiently than the normal cylinder.

- The forced vibration test shows that the Strouhal-type frequency in the wavy cylinder could be revealed by selecting proper external forcing frequency. This should serve as an primary explanation for the destabilization of the wavy cylinder in the free vibrations.

Chapter 6

Final Remarks

6.1 Conclusions

By the means of large eddy simulation, the current thesis presented a detailed investigation of flow around wavy circular cylinders, with the aim to clarify whether such a morphology could still be control-effective in more complicated configurations. Two situations, i.e., static wavy cylinder placed inclined to the incoming flow, and flexibly mounted wavy cylinder freely oscillating in the transverse direction, have been considered.

When the wavy cylinder is inclined to the incoming flow, aerodynamic performance differs depending on the geometrics of the waviness. Small wavelength cylinder with the wavelength $\lambda/D_m = 2$ could completely suppress the Kármán vortex shedding in the non-inclined cases, however, at $\alpha = 30^\circ \sim 45^\circ$, the vortex shedding resurrects, and the resulted drag and lift coefficients becomes much larger than that for a normal cylinder, rendering this wavy cylinder impractical for the bridge cables. On the other hand, the long wavelength cylinders with $\lambda/D_m = 6$ exhibit much smaller increase in the force coefficients when they are inclined to the incoming flow. In addition, from the aesthetic point of view, the cylinders with longer wavelength generally presents elegant appearances to the users because of its slenderness. Thus, the long-wavelength cylinder presents a better choice for engineering applications where drag reduction is needed.

As for the vibrational characteristics of the wavy cylinder, it is revealed that the aeroelastic behavior of the wavy cylinder features that are also found in the normal cylinder, although the former presents glaring difference in the fixed configuration. This reminds us the discovery by Pastò (2008), in which the vortex induced vibration persists even at the critical Reynold number characterized by a cessation of coherent vortex shedding in steady configuration. Both cases imply that the vortex induced vibrations may not be initiated by the Kármán vortex shedding, and thus may defy the conventional view on the mechanism of vortex induced vibration that VIV is a resonance effect with nonlinear feedback (De Langre, 2006). We further suspect that the different behavior of the wavy cylinder at fixed and flexibly mounted configurations may be of similar mechanism with the finding that VIV of a circular cylinders could occur at Reynolds numbers inferior to 47, below which the lift force is strictly zero (Buffoni, 2003; Mittal and Singh, 2005; Leoniti and Thompson, 2010). In view of the above, the wavy cylinder does not lend itself to a perfect device for vibration suppression, at least for vortex induced vibration for marine structures where the mass ratio is usually small.

In spite of the overwhelmingly positive attitudes towards the aerodynamics of the wavy cylinders reported by the prior researches, the current thesis points out that such beneficial aerodynamic performance is not well preserved in the considered two aspects. It seems that the wavy cylinders need a delicate environment for them to be control-effective, that is non-inclined and stationary. For engineering applications, in which the operating condition is far more complicated than the cases considered here, the wavy

cylinders should be used with caution. The current thesis could also trigger more research interests into the fluid mechanics of the wavy cylinders, which are listed in section 6.2.

6.2 Prospects for future researches

While the wavy cylinders have been studied a lot in the past 30 years, and its flow control suppression capacity has been widely recognized, the current thesis clearly points out that there are still a lot to be discovered. We put forward some ideas that might be worth research effort in this section.

- The mechanism of the stabilization of the wavy cylinder in the static configuration is still not clear. Three dimensional global analysis must be helpful in understanding this phenomenon. However, the resolution of the tri-global modes is extremely computationally expensive. Alternatively, the dynamic mode decomposition based global stability analysis could be a possible way to resolve this problem (Stankiewicz et al., 2015; Ferrer, Vicente, and Valero, 2014). This topic is now undergoing by us.
- The destabilization of the wavy cylinder in the dynamic cases warrants deeper investigations. In future studies, linear stability analysis in the line of Zhang et al. (2015) and Mittal (2016) will be carried out further explore the mechanism of the hydro-elastic behavior of the wavy cylinders and the role of structural damping. Besides, in the current thesis, harmonic forcing in the form of structural motion has been applied. Other forms of forcing, such as temporally periodic flux injection, might facilitate the resolvent analysis (Taira et al., 2017), which is believed to be helpful in understanding the revival of the Strouhal-like frequency exhibited by the wavy cylinder better.
- It is interesting to know whether the combined passive and active flow control, in the current case, wavy cylinder with span-wise distributed forcing as in Kim and Choi (2005), could work to enhance the flow control efficacy of the wavy cylinder, or in another word, could the passive geometry further alleviate the energy consumption required in the distributed forcing method.
- Up to now, all the investigations on the wavy cylinders have been conducted at sub-critical Reynolds numbers. There is no information about the aerodynamic performance of the wavy cylinder at critical, or post-critical Reynolds numbers. This is one of the key issue of whether the wavy cylinder could be manufactured for the real bridge cables, for which the post-critical Reynolds numbers are of the greatest interest.
- In applying to the wavy cylinders to the cable-stayed bridges, the rain-wind induced vibration is expected to be mitigated since the undulation of the geometry could prevent the water rivulets from forming. However, we still do not know whether such a cylinder could be effective against the dry galloping.
- Conventionally, in order to reduce riser top tensile stresses and floating vessel connection loads, buoyancy in the form of added concentric circles are connected to the risers. This greatly increases the drag-to-weight ratio, and in turn affects the riser dynamic response (O'Brien and O'Sullivan, 1999). Instead of the concentric circles, the wavy coating could be used. In this case, the drag force could be largely reduced.

Appendix A

Validation and mesh dependency test

CFD simulations are carried out on computation domains that are properly meshed. The mesh resolution should be delicately chosen so that it could yield satisfactory result without posing excessive burden on the computational resources. The current appendix presents the mesh dependency test for both the static and dynamic cases in order to determine an appropriate set of mesh resolution of the simulations undertaken herein.

TABLE A.1: Mesh dependency test for a static circular cylinder at $Re = 5000$

NO.	Domain	Mesh	maxCo	C_d	$C_{l\ r.m.s.}$
A1	$40D \times 6.28D$	$160 \times 160 \times 96$	2	1.005	0.149
A2	$40D \times 6.28D$	$180 \times 180 \times 96$	2	0.985	0.121
B1	$40D \times 3.14D$	$160 \times 160 \times 48$	1	0.996	0.143
B2	$40D \times 3.14D$	$160 \times 160 \times 48$	2	1.021	0.153
B3	$40D \times 3.14D$	$200 \times 200 \times 48$	2	0.977	0.123

Table A.1 presents the five cases that are used in the mesh dependency test for the $x - y$ cross-section of the static circular cylinder at $Re = 5000$. Case A1 and A2 have a span-wise length of $6.28D$, while the cases titled B are performed with half of the span-wise length of case A to save computation time. It was revealed by Kravchenko and Moin (2000) and Breuer (1998) that doubling the cylinder span from πD to $2\pi D$ while maintaining the same axial resolution would yield similar results in terms of aerodynamic forces and mean wake properties. This conclusion grants us the rightful reason to make direct comparisons between Case As and Bs. With the same resolution in the span-wise direction, case A1, A2 and B3 are distinguished by their increasing grid points in the cross-section. The effect of time-step is compared by B1 and B2, in which the time-steps in each of the cases are decided by setting the maximum Courant number to be 1 and 2. The statistics of each case are gathered for 200 non-dimensional seconds after a 100 non-dimensional seconds pre-run to eliminate the initial transients. Three papers taken as reference in this section are the experimental work by Norberg (1998) and two LES works by Kim (2006) and Doolan (2010). Note that the last paper is dedicated to a slightly larger Reynolds number of 5600.

While the drag force coefficients are found to decrease as the cross-sectional mesh is refined, the difference between case A1 and B3 is only 3%. The effect of span-wise length is again proved of minor significance, based on case A1 and B2. From case B1 and B2 it is concluded that the effect of time-step is also trivial. The resulted time-step for case A1 is $\Delta t = 0.013$. It is noted that a time-step of around $\Delta t = 0.01$ was used in several cross cylinder flow studies at similar Reynolds numbers (e.g., $\Delta t = 0.01$ for Lee *et al.* Lee, Campbell, and Hambric, 2014's DES at $Re = 5000$, $\Delta t = 0.0172$ for Doolan (2010)'s LES at $Re = 5600$).

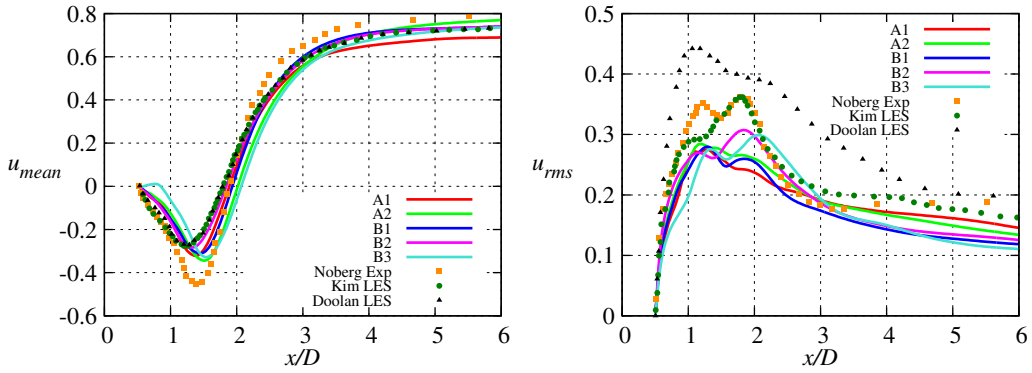

(A) Mean stream-wise velocity (B) Fluctuating stream-wise velocity

FIGURE A.1: Mean stream-wise velocity and *r.m.s.* fluctuating velocity along wake center line

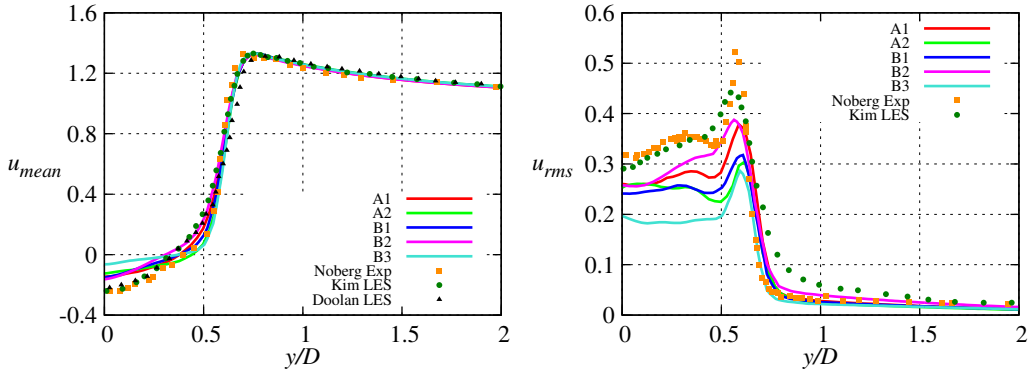

(A) Mean stream-wise velocity (B) Fluctuating stream-wise velocity

FIGURE A.2: Mean stream-wise velocity and *r.m.s.* fluctuating velocity at $x/D = 1$

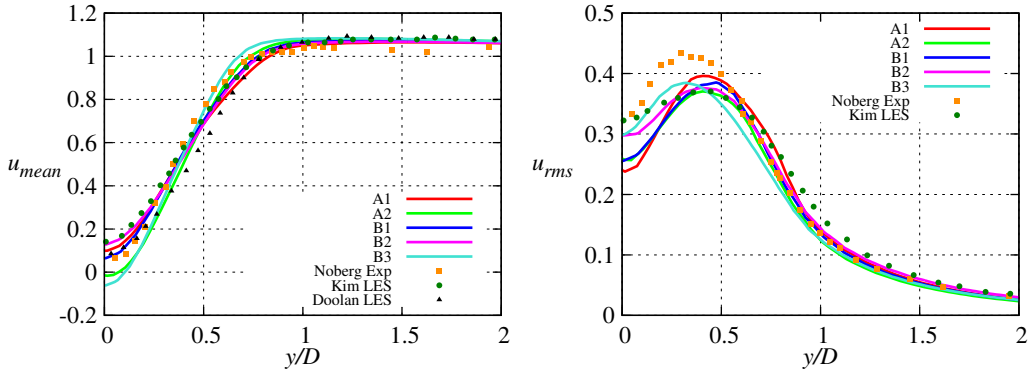

(A) Mean stream-wise velocity (B) Fluctuating stream-wise velocity

FIGURE A.3: Mean stream-wise velocity and *r.m.s.* fluctuating velocity at $x/D = 2$

The mean stream-wise velocity profiles are shown in Fig. A.1 to Fig. A.3. It could be observed from these figures that case A1, although possessing the relatively coarse mesh resolution, produces fare agreement with the existing literature. The results from the finer meshed cases deviate only slightly from that of A1, and this deviation does not improve the results to better agreement with the literature. Less satisfying result is obtained for

the $r.m.s.$ fluctuating velocity. Although the general trend has been reproduced, its value is smaller compared to that in the literature. The relatively lower value of u_{rms} may have its origin in the turbulence model we used. Lysenko, Ertesvåg, and Rian (2012) employed high spatial resolution (300×300 in the cross-section plane) for his LES of flow around circular cylinder at $Re = 3900$ with the dynamic k-equation turbulence model, the value of u_{rms} was also under-predicted. It would seem that the prediction of u_{rms} is more challenging than u_{mean} by this turbulence model.

Based on the above statements, it could be inferred that the case A1 is not perfectly converged; however, the discrepancy of A1 compared with other refined cases is small. Particularly, case A1 qualifies an accurate prediction of flow variables such as mean velocity, aerodynamic forces, etc.

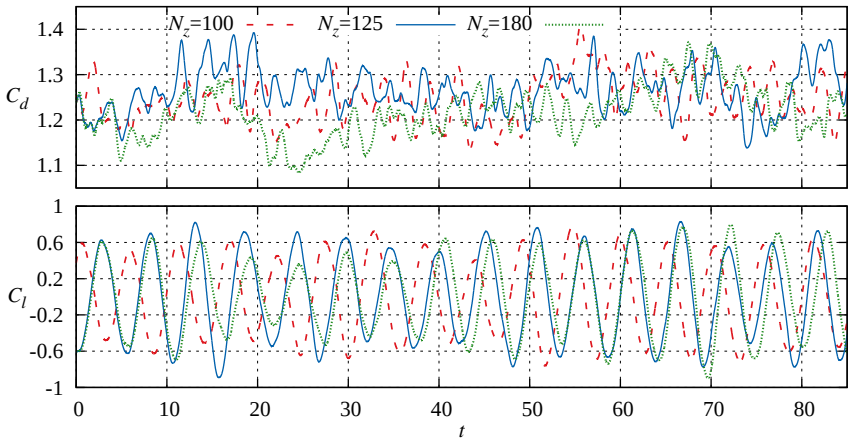

FIGURE A.4: Time histories of the force coefficients of the 2_0.15 wavy cylinder at $\alpha = 45°$ from three different meshes.

TABLE A.2: Summary of drag, lift coefficients and the Strouhal number for the 2_0.15 wavy cylinder at $\alpha = 45°$. The span-wise length of the cylinder is $8D_m$.

N_z	C_d	$C_d^{'}$	$C_l^{'}$	St
100	1.246	0.0527	0.426	0.1831
125	1.267	0.0491	0.471	0.1892
180	1.207	0.0539	0.407	0.1892

In the case of inclined flow around wavy cylinders, the wake aerodynamics are complicated by the involvement of the axial velocity over the wavy tubercles, making the mesh dependency test for the axial grid resolution indispensable. For the inclined cylinder cases, the 2_0.15 wavy cylinder at $\alpha = 45°$ is selected for the axial mesh dependency test since this particular case presents the most critical situation: the steepest geometric gradient with the largest span-wise velocity. We fix the planar mesh resolution to $N_r \times N_c = 180 \times 180$ and vary the span-wise grids N_z to see if there is qualitative changes in the flow variables such as the drag and lift coefficients. To save computational effort, a total length of $L = 8D_m$, which encompasses 4 waves, is investigated with three levels of span-wise grids number: $N_z = 100, 125$ and 180. The time histories of the span-wise averaged drag and lift coefficients are presented in Fig. A.2. Owing to the turbulence effect, the time histories of the drag and lift coefficients of the three meshes are very irregular. However, the mean and fluctuating values appear to be statistically close. Table **??** presents the comparison of the mean drag C_d, the rms drag and lift $C_d^{'}$, $C_l^{'}$ as well as the

Strouhal number St of the three meshes. The fair agreement between the three levels of grids indicates that the results have converged at $N_z = 125$. In view of this, the medium mesh, which has 125 grids for a span-wise length of $8D_m$ ($\Delta z = 0.064D_m$) is selected for the current work.

Another set of mesh dependency test has been conducted for the dynamic mesh cases, which will be employed for the simulation of free and forced vibration in Chapter 5. The results of this mesh dependency test is shown in Table A.3. Regarding the case naming conventions, the first letter N or W indicates the normal or wavy cylinder. The next word points out the reduced velocity. The last letter A, B, C or D indicates the mesh and temporal resolution. Specifically, compared with the case A, the time-step is halved in the cases denoted B, and the cases denoted C are associated with the refined mesh in the x-y plane. For the wavy cylinder, the D cases, in which the span-wise meshes are refined, are performed to account for the span-wise waviness. N_c, N_r and N_z denote the grids in the circumferential, radial and span-wise direction. Y_{max} is defined as the average of the top 10% peak amplitude. f is the primary frequency that contains the highest energy content from the spectrum of the vibration response and f_n is the natural frequency in vacuum. The averaged values as well as the root mean squared (rms) values of C_d and C_l are included in the table for comparison. We compare the results based on the cases denoted A, which has spatial resolution of $160 \times 160 \times 80$ and time-step $\Delta t = 0.01$. It could be seen that the results in terms of maximum amplitude, primary frequency, fluid-induced forces are in reasonable agreement when the spatial ro temporal resolutions are refined. Further more, as will be shown in the next chapter, the current results of the normal cylinder in terms of maximum vibration amplitude, primary frequency, drag and lift forces, etc., are in excellent agreement with the literature. Since the current work is the first study on the VIV of the wavy cylinder, its results could not be validated through previous literature. However, we have employed the same numerical model and the calculation method for the wavy and normal cylinders, and the results of the latter have shown to be of high fidelity. Thus, it is reasonable to believe that the results of the wavy cylinder is also of enough accuracy and trustworthy.

TABLE A.3: Mesh dependency test for the dynamic mesh cases

Case	$N_c \times N_r \times N_z$	Δt	Y_{max}/D	f/f_n	$C_{d_{mean}}$	$C_{d_{rms}}$	$C_{l_{rms}}$
N_Ur5_A	$160 \times 160 \times 80$	0.01	0.98	0.88	2.45	0.71	0.89
N_Ur5_B	$160 \times 160 \times 80$	0.005	0.94	0.93	2.53	0.69	0.81
N_Ur5_C	$200 \times 200 \times 80$	0.01	0.92	0.94	2.48	0.59	0.73
N_Ur7_A	$160 \times 160 \times 80$	0.01	0.62	1.09	1.51	0.24	0.29
N_Ur7_B	$160 \times 160 \times 80$	0.005	0.60	1.09	1.51	0.25	0.32
N_Ur7_C	$200 \times 200 \times 80$	0.01	0.60	1.07	1.49	0.22	0.26
W_Static_A	$160 \times 160 \times 80$	0.01	-	-	0.80	0.023	0.013
W_Static_D	$160 \times 160 \times 100$	0.01	-	-	0.80	0.017	0.014
W_Ur5_A	$160 \times 160 \times 80$	0.01	0.83	0.90	2.26	0.45	0.76
W_Ur5_D	$160 \times 160 \times 100$	0.01	0.79	0.91	2.26	0.45	0.69
W_Ur7_A	$160 \times 160 \times 80$	0.01	0.55	1.06	1.40	0.16	0.22
W_Ur7_D	$160 \times 160 \times 100$	0.01	0.56	1.09	1.42	0.17	0.20

Bibliography

Achenbach, Elmar (1971). "Influence of surface roughness on the cross-flow around a circular cylinder". In: *Journal of Fluid Mechanics* 46.2, pp. 321–335.

Ahmed, A, MJ Khan, and B Bays-Muchmore (1993). "Experimental investigation of a three-dimensional bluff-body wake". In: *AIAA Journal* 31.3, pp. 559–563.

Ahmed, Anwar and Byram Bays-Muchmore (1992). "Transverse flow over a wavy cylinder". In: *Physics of Fluids A: Fluid Dynamics (1989-1993)* 4.9, pp. 1959–1967.

Aljure, DE et al. (2017). "Three dimensionality in the wake of the flow around a circular cylinder at Reynolds number 5000". In: *Computers & Fluids* 147, pp. 102–118.

Anagnostopoulos, P (2000). "Numerical study of the flow past a cylinder excited transversely to the incident stream. Part 1: Lock-in zone, hydrodynamic forces and wake geometry". In: *Journal of Fluids and Structures* 14.6, pp. 819–851.

Anderson, EA and AA Szewczyk (1997). "Effects of a splitter plate on the near wake of a circular cylinder in 2 and 3-dimensional flow configurations". In: *Experiments in Fluids* 23.2, pp. 161–174.

Apelt, CJ and GS West (1975). "The effects of wake splitter plates on bluff-body flow in the range $10^4 < R < 5 \times 10^4$. Part 2". In: *Journal of Fluid Mechanics* 71.01, pp. 145–160.

Apelt, CJ, GS West, and Albin A Szewczyk (1973). "The effects of wake splitter plates on the flow past a circular cylinder in the range $10^4 < Re < 5 \times 10^4$". In: *Journal of Fluid Mechanics* 61.01, pp. 187–198.

Bahmani, MH and MH Akbari (2010). "Effects of mass and damping ratios on VIV of a circular cylinder". In: *Ocean Engineering* 37.5, pp. 511–519.

Bao, Yan and Jianjun Tao (2013a). "Active control of a cylinder wake flow by using a streamwise oscillating foil". In: *Physics of Fluids (1994-present)* 25.5, p. 053601.

— (2013b). "The passive control of wake flow behind a circular cylinder by parallel dual plates". In: *Journal of Fluids and Structures* 37, pp. 201–219.

Bao, Yan, Dai Zhou, and Jiahuang Tu (2011). "Flow interference between a stationary cylinder and an elastically mounted cylinder arranged in proximity". In: *Journal of fluids and structures* 27.8, pp. 1425–1446.

Bearman, P W (1976). "Golfball aerodynamics". In: *Aeronautical Quarterly* 27, pp. 112–122.

Bearman, Peter W (1984). "Vortex shedding from oscillating bluff bodies". In: *Annual Review of Fluid Mechanics* 16.1, pp. 195–222.

Bearman, Peter W and John C OWen (1998). "Reduction of bluff-body drag and suppression of vortex shedding by the introduction of wavy separation lines". In: *Journal of Fluids and Structures* 12.1, pp. 123–130.

Bearman, PW (1965). "Investigation of the flow behind a two-dimensional model with a blunt trailing edge and fitted with splitter plates". In: *Journal of Fluid Mechanics* 21.02, pp. 241–255.

— (1967). "The effect of base bleed on the flow behind a two-dimensional model with a blunt trailing edge". In: *Aeronautical Quarterly* 18.03, pp. 207–224.

Bearman, PW and JK Harvey (1993). "Control of circular cylinder flow by the use of dimples". In: *AIAA Journal* 31.10, pp. 1753–1756.

Beem, Heather, Matthew Hildner, and Michael Triantafyllou (2012). "Calibration and validation of a harbor seal whisker-inspired flow sensor". In: *Smart Materials and Structures* 22.1, p. 014012.

Berger, Eberhard (1967). "Suppression of vortex shedding and turbulence behind oscillating cylinders". In: *The Physics of Fluids* 10.9, S191–S193.

Berger, Eberhard and Rudolf Wille (1972). "Periodic flow phenomena". In: *Annual Review of Fluid Mechanics* 4.1, pp. 313–340.

Bishop, RED and AY Hassan (1964). "The lift and drag forces on a circular cylinder oscillating in a flowing fluid". In: *Proceedings of the Royal Society of London A: Mathematical, Physical and Engineering Sciences*. Vol. 277. 1368. The Royal Society, pp. 51–75.

Blackburn, HM and WH Melbourne (1996). "The effect of free-stream turbulence on sectional lift forces on a circular cylinder". In: *Journal of Fluid Mechanics* 306, pp. 267–292.

Blevins, Robert D (1990). *Flow-induced vibration*. New York, NY (USA); Van Nostrand Reinhold Co., Inc.

Bloor, M Susan (1964). "The transition to turbulence in the wake of a circular cylinder". In: *Journal of Fluid Mechanics* 19.02, pp. 290–304.

Bourguet, Rémi, George Em Karniadakis, and Michael S Triantafyllou (2015). "On the validity of the independence principle applied to the vortex-induced vibrations of a flexible cylinder inclined at 60°". In: *Journal of Fluids and Structures* 53, pp. 58–69.

Bourguet, Rémi and Michael S Triantafyllou (2016). "The onset of vortex-induced vibrations of a flexible cylinder at large inclination angle". In: *Journal of Fluid Mechanics* 809, pp. 111–134.

Breuer, Michael (1998). "Numerical and modeling influences on large eddy simulations for the flow past a circular cylinder". In: *International Journal of Heat and Fluid Flow* 19.5, pp. 512–521.

Buffoni, E (2003). "Vortex shedding in subcritical conditions". In: *Physics of Fluids (1994-present)* 15.3, pp. 814–816.

Burlina, Celeste et al. (2015). "Preliminary evaluation of two new cable surface innovations". In: *14th International Conference on Wind Engineering*.

— (2016). "Opitmization of bridge cables with concave fillets". In: *8th International Colloquium on Bluff Body Aerodynamics and Applications*.

Cabral, Brian and Leith Casey Leedom (1993). "Imaging vector fields using line integral convolution". In: *Proceedings of the 20th annual conference on Computer graphics and interactive techniques*. ACM, pp. 263–270.

Cajas, Juan C et al. (2016). "SHAPE Project Vortex Bladeless: Parallel multi-code coupling for Fluid-Structure Interaction in Wind Energy Generation". In:

Carberry, J, J Sheridan, and D Rockwell (2001). "Forces and wake modes of an oscillating cylinder". In: *Journal of Fluids and Structures* 15.3-4, pp. 523–532.

— (2005). "Controlled oscillations of a cylinder: forces and wake modes". In: *Journal of Fluid Mechanics* 538, pp. 31–69.

Chakrabarti, Subrata (2005). *Handbook of Offshore Engineering (2-volume set)*. Elsevier.

Chen, Shih-Sheng, Ruey-Hor Yen, and An-Bang Wang (2011). "Investigation of the resonant phenomenon of flow around a vibrating cylinder in a subcritical regime". In: *Physics of Fluids* 23.1, p. 014105.

Chiu, WS et al. (1967). "On real fluid flow over yawed circular cylinders". In: *Journal of Fluids Engineering* 89.4, pp. 851–857.

Choi, Haecheon, Woo-Pyung Jeon, and Jinsung Kim (2008). "Control of flow over a bluff body". In: *Annual Reviewer Fluid Mechanics* 40, pp. 113–139.

Constantinides, Yiannis and Owen H Oakley (2006). "Numerical prediction of bare and straked cylinder VIV". In: *25th International Conference on Offshore Mechanics and Arctic Engineering*. American Society of Mechanical Engineers, pp. 745–753.

Cossu, Carlo and Luigi Morino (2000). "On the instability of a spring-mounted circular cylinder in a viscous flow at low Reynolds numbers". In: *Journal of Fluids and Structures* 14.2, pp. 183–196.

De Langre, Emmanuel (2006). "Frequency lock-in is caused by coupled-mode flutter". In: *Journal of Fluids and Structures* 22.6, pp. 783–791.

Dehnhardt, Guido, Björn Mauck, and Horst Bleckmann (1998). "Seal whiskers detect water movements". In: *Nature* 394.6690, pp. 235–236.

Dehnhardt, Guido et al. (2001). "Hydrodynamic trail-following in harbor seals (Phoca vitulina)". In: *Science* 293.5527, pp. 102–104.

Doolan, CJ (2010). "Large eddy simulation of the near wake of a circular cylinder at subcritical Reynolds number". In: *Engineering Applications of Computational Fluid Mechanics* 4.4, pp. 496–510.

Dullweber, Andreas, Benedict Leimkuhler, and Robert McLachlan (1997). "Symplectic splitting methods for rigid body molecular dynamics". In: *The Journal of chemical physics* 107.15, pp. 5840–5851.

Edel, RK and HE Winn (1978). "Observations on underwater locomotion and flipper movement of the humpback whale Megaptera novaeangliae". In: *Marine Biology* 48.3, pp. 279–287.

Eguchi, Y et al. (2002). "Drag reduction mechanism and aerodynamic characteristics of a newly developed overhead electric wire". In: *Journal of Wind Engineering and Industrial Aerodynamics* 90.4, pp. 293–304.

El-Shahat, Adel (2016). "Bladeless Wind Turbine as Wind Energy Possible Future Technology". In: *Natural Gas & Electricity* 33.4, pp. 16–20.

Étienne, Stéphane and Dominique Pelletier (2012). "The low Reynolds number limit of vortex-induced vibrations". In: *Journal of Fluids and Structures* 31, pp. 18–29.

Feng, CC (2011). "The measurement of vortex induced effects in flow past stationary and oscillating circular and D-section cylinders". PhD thesis. University of British Columbia.

Ferrer, Esteban, Javier Vicente, and Eusebio Valero (2014). "Low cost 3D global instability analysis and flow sensitivity based on dynamic mode decomposition and high-order numerical tools". In: *International Journal for Numerical Methods in Fluids* 76.3, pp. 169–184.

Feymark, Andreas et al. (2013). "Large-Eddy Simulation of an Oscillating Cylinder in a Steady Flow". In: *AIAA Journal* 51.4, pp. 773–783.

Fish, FE and GV Lauder (2006). "Passive and active flow control by swimming fishes and mammals". In: *Annual Reviewer Fluid Mechanics* 38, pp. 193–224.

Fish, Franke E and Juliann M Battle (1995). "Hydrodynamic design of the humpback whale flipper". In: *Journal of Morphology* 225.1, pp. 51–60.

Fureby, C et al. (1997). "A comparative study of subgrid scale models in homogeneous isotropic turbulence". In: *Physics of Fluids (1994-present)* 9.5, pp. 1416–1429.

Gabbai, RD and H Benaroya (2005). "An overview of modeling and experiments of vortex-induced vibration of circular cylinders". In: *Journal of Sound and Vibration* 282.3, pp. 575–616.

Germano, Massimo et al. (1991). "A dynamic subgrid-scale eddy viscosity model". In: *Physics of Fluids A: Fluid Dynamics (1989-1993)* 3.7, pp. 1760–1765.

Gerrard, JH (1966). "The mechanics of the formation region of vortices behind bluff bodies". In: *Journal of Fluid Mechanics* 25.02, pp. 401–413.

Govardhan, R and CHK Williamson (2000). "Modes of vortex formation and frequency response of a freely vibrating cylinder". In: *Journal of Fluid Mechanics* 420, pp. 85–130.

Govardhan, R and CHK Williamson (2002). "Resonance forever: existence of a critical mass and an infinite regime of resonance in vortex-induced vibration". In: *Journal of Fluid Mechanics* 473, pp. 147–166.

Griffin, OM (1980). "Vortex-excited cross-flow vibrations of a single cylindrical tube". In: *Journal of Pressure Vessel Technology* 102.2, pp. 158–166.

Hanke, Wolf et al. (2010). "Harbor seal vibrissa morphology suppresses vortex-induced vibrations". In: *The Journal of Experimental Biology* 213.15, pp. 2665–2672.

Hansen, Kristy L, Richard M Kelso, and Bassam B Dally (2011). "Performance variations of leading-edge tubercles for distinct airfoil profiles". In: *AIAA Journal* 49.1, pp. 185–194.

Hanson, AR (1966). "Vortex shedding from yawed cylinders." In: *AIAA Journal* 4.4, pp. 738–740.

He, Tao (2015). "A partitioned implicit coupling strategy for incompressible flow past an oscillating cylinder". In: *International Journal of Computational Methods* 12.02, p. 1550012.

He, Tao, Dai Zhou, and Yan Bao (2012). "Combined interface boundary condition method for fluid-rigid body interaction". In: *Computer Methods in Applied Mechanics and Engineering* 223, pp. 81–102.

He, Tao et al. (2014). "Partitioned subiterative coupling schemes for aeroelasticity using combined interface boundary condition method". In: *International Journal of Computational Fluid Dynamics* 28.6-10, pp. 272–300.

Hirsch, C (1990). "Numerical computation of internal and external flows, vol. 2Wiley". In: *New York*.

Hoerner, Sighard F (1965). *Fluid-dynamic drag: practical information on aerodynamic drag and hydrodynamic resistance*. Hoerner Fluid Dynamics Midland Park, NJ.

Hojo, Tetsuo, Shinsuke Yamazaki, and Hiroyuki Okada (2000). "Development of lowdrag aerodynamically stable cable with indented processing". In: *Nippon Steel Technical Report* 82, pp. 15–22.

Hover, Franz S, Joshua T Davis, and Michael S Triantafyllou (2004). "Three-dimensionality of mode transition in vortex-induced vibrations of a circular cylinder". In: *European Journal of Mechanics-B/Fluids* 23.1, pp. 29–40.

Hover, FS, AH Techet, and MS Triantafyllou (1998). "Forces on oscillating uniform and tapered cylinders in crossflow". In: *Journal of Fluid Mechanics* 363.1, p. 97.

Hunt, Julian CR, Alan A Wray, and Parviz Moin (1988). "Eddies, streams, and convergence zones in turbulent flows". In: *Center for Turbulence Research CTR-S 88*.

Hwang, Yongyun, Jinsung Kim, and Haecheon Choi (2013). "Stabilization of absolute instability in spanwise wavy two-dimensional wakes". In: *Journal of Fluid Mechanics* 727, pp. 346–378.

Iida, A et al. (1997). "Prediction of aerodynamic sound spectra from a circular cylinder". In: *Proc. FLUCOME*. Vol. 97, pp. 121–6.

Jackson, CP (1987). "A finite-element study of the onset of vortex shedding in flow past variously shaped bodies". In: *Journal of Fluid Mechanics* 182, pp. 23–45.

Jasak, Hrvoje (1996). "Error analysis and estimation for finite volume method with applications to fluid flow". PhD thesis. Imperial College London.

Jauvtis, N and CHK Williamson (2004). "The effect of two degrees of freedom on vortex-induced vibration at low mass and damping". In: *Journal of Fluid Mechanics* 509, pp. 23–62.

Jiang, Renjie and Pengjun Zheng (2017). "Resonance in flow past oscillating cylinder under subcritical conditions". In: *Applied Mathematics and Mechanics* 38.3, pp. 363–378.

Johari, Hamid et al. (2007). "Effects of leading-edge protuberances on airfoil performance". In: *AIAA Journal* 45.11, pp. 2634–2642.

Jung, Jae Hwan and Hyun Sik Yoon (2014). "Large eddy simulation of flow over a twisted cylinder at a subcritical Reynolds number". In: *Journal of Fluid Mechanics* 759, pp. 579–611.

Khalak, A and CHK Williamson (1996). "Dynamics of a hydroelastic cylinder with very low mass and damping". In: *Journal of Fluids and Structures* 10.5, pp. 455–472.

— (1997). "Fluid forces and dynamics of a hydroelastic structure with very low mass and damping". In: *Journal of Fluids and Structures* 11.8, pp. 973–982.

— (1999). "Motions, forces and mode transitions in vortex-induced vibrations at low mass-damping". In: *Journal of Fluids and Structures* 13.7, pp. 813–851.

Kim, Eun Soo, Michael M Bernitsas, and R Ajith Kumar (2013). "Multicylinder Flow-Induced Motions: Enhancement by Passive Turbulence Control at 28,000< Re< 120,000". In: *Journal of Offshore Mechanics and Arctic Engineering* 135.2, p. 021802.

Kim, Jinsung and Haecheon Choi (2005). "Distributed forcing of flow over a circular cylinder". In: *Physics of Fluids (1994-present)* 17.3, p. 033103.

Kim, Sung Eun (2006). "Large eddy simulation of turbulent flow past a circular cylinder in subcritical regime". In: *AIAA Paper* 1418, pp. 9–12.

Kim, Woojin, Jungil Lee, and Haecheon Choi (2016). "Flow around a helically twisted elliptic cylinder". In: *Physics of Fluids* 28.5, p. 053602.

Kimura, Takeyoshi and Michihisa Tsutahara (1991). "Fluid dynamic effects of grooves on circular cylinder surface". In: *AIAA Journal* 29.12, pp. 2062–2068.

Konstantinidis, E, S Balabani, and M Yianneskis (2003). "The effect of flow perturbations on the near wake characteristics of a circular cylinder". In: *Journal of Fluids and Structures* 18.3, pp. 367–386.

Konstantinidis, E and D Bouris (2009). "Effect of nonharmonic forcing on bluff-body vortex dynamics". In: *Physical Review E* 79.4, p. 045303.

Konstantinidis, Efstathios and Demetri Bouris (2016). "Vortex synchronization in the cylinder wake due to harmonic and non-harmonic perturbations". In: *Journal of Fluid Mechanics* 804, pp. 248–277.

Koopmann, GH (1967). "The vortex wakes of vibrating cylinders at low Reynolds numbers". In: *Journal of Fluid Mechanics* 28.03, pp. 501–512.

Korkischko, Ivan et al. (2007). "An experimental investigation of the flow around straked cylinders". In: *ASME 2007 26th International Conference on Offshore Mechanics and Arctic Engineering*. American Society of Mechanical Engineers, pp. 641–647.

Kottapalli, AGP et al. (2015). "Harbor seal whisker inspired flow sensors to reduce vortex-induced vibrations". In: *Micro Electro Mechanical Systems (MEMS), 2015 28th IEEE International Conference on*. IEEE, pp. 889–892.

Kou, Jiaqing et al. (2017). "The lowest Reynolds number of vortex-induced vibrations". In: *Physics of Fluids* 29.4, p. 041701.

Kozakiewicz, Andrzej, Jørgen Fredsee, B Mutlu Sumer, et al. (1995). "Forces on pipelines in oblique attack: steady current and waves". In: *The fifth international offshore and polar engineering conference*. International Society of Offshore and Polar Engineers.

Kravchenko, Arthur G and Parviz Moin (2000). "Numerical studies of flow over a circular cylinder at ReD=3900". In: *Physics of Fluids (1994-present)* 12.2, pp. 403–417.

Kumar, Raghavan A, Chan-Hyun Sohn, and Bangalore HL Gowda (2008). "Passive control of vortex-induced vibrations: an overview". In: *Recent Patents on Mechanical Engineering* 1.1, pp. 1–11.

Kumar, Samvit, Navrose, and Sanjay Mittal (2016). "Lock-in in forced vibration of a circular cylinder". In: *Physics of Fluids* 28.11, p. 113605.

Kwon, Kiyoung and Haecheon Choi (1996). "Control of laminar vortex shedding behind a circular cylinder using splitter plates". In: *Physics of Fluids* 8.2, pp. 479–486.

Lam, K and YF Lin (2008). "Large eddy simulation of flow around wavy cylinders at a subcritical Reynoldss number". In: *International Journal of Heat and Fluid Flow* 29.4, pp. 1071–1088.

— (2009). "Effects of wavelength and amplitude of a wavy cylinder in cross-flow at low Reynolds numbers". In: *Journal of Fluid Mechanics* 620, pp. 195–220.

Lam, K, FH Wang, and RMC So (2004). "Three-dimensional nature of vortices in the near wake of a wavy cylinder". In: *Journal of Fluids and Structures* 19.6, pp. 815–833.

Lam, K et al. (2004). "Experimental investigation of the mean and fluctuating forces of wavy (varicose) cylinders in a cross-flow". In: *Journal of Fluids and Structures* 19.3, pp. 321–334.

Lam, K et al. (2010). "Investigation of turbulent flow past a yawed wavy cylinder". In: *Journal of Fluids and Structures* 26.7, pp. 1078–1097.

Larose, Guy L et al. (2013). "Wind-tunnel investigations of an inclined stay cable with a helical fillet". In: *6th European and African Conference on Wind Engineering, Cambridge, England*.

Lee, Abe H, Robert L Campbell, and Stephen A Hambric (2014). "Coupled delayed-detached-eddy simulation and structural vibration of a self-oscillating cylinder due to vortex-shedding". In: *Journal of Fluids and Structures* 48, pp. 216–234.

Lee, JH and MM Bernitsas (2011). "High-damping, high-Reynoldss VIV tests for energy harnessing using the VIVACE converter". In: *Ocean Engineering* 38.16, pp. 1697–1712.

Lee, Sang-Joon and Anh-Tuan Nguyen (2007). "Experimental investigation on wake behind a wavy cylinder having sinusoidal cross-sectional area variation". In: *Fluid Dynamics Research* 39.4, pp. 292–304.

Leehey, P and CE Hanson (1970). "Aeolian tones associated with resonant vibration". In: *Journal of Sound and Vibration* 13.4, pp. 465–483.

Lehmkuhl, O et al. (2014). "Unsteady forces on a circular cylinder at critical Reynoldss numbers". In: *Physics of Fluids* 26.12, p. 125110.

Lei, Chengwang, Liang Cheng, and Ken Kavanagh (2001). "Spanwise length effects on three-dimensional modelling of flow over a circular cylinder". In: *Computer methods in applied mechanics and engineering* 190.22, pp. 2909–2923.

Leoniti, J.S. and M.C. Thompson (2010). "Cylinder wake destabilisation due to elastic mounting". In: *IUTAM Symposium on Bluff Body Wakes and Vortex-Induced Vibrations*. 22-25 June, Capri, Italy, pp. 221–224.

Lilly, Douglas K (1992). "A proposed modification of the Germano subgrid-scale closure method". In: *Physics of Fluids A: Fluid Dynamics (1989-1993)* 4.3, pp. 633–635.

Lin, YF et al. (2016). "Effects of large spanwise wavelength on the wake of a sinusoidal wavy cylinder". In: *Journal of Fluids and Structures* 61, pp. 392–409.

Lucor, D, J Foo, and GE Karniadakis (2005). "Vortex mode selection of a rigid cylinder subject to VIV at low mass-damping". In: *Journal of Fluids and Structures* 20.4, pp. 483–503.

Lucor, Didier and George Em Karniadakis (2003). "Effects of oblique inflow in vortex-induced vibrations". In: *Flow, Turbulence and Combustion* 71.1-4, pp. 375–389.

Lysenko, Dmitry A, Ivar S Ertesvåg, and Kjell Erik Rian (2012). "Large-eddy simulation of the flow over a circular cylinder at Reynolds number 3900 using the OpenFOAM toolbox". In: *Flow, Turbulence and Combustion* 89.4, pp. 491–518.

Matsumoto, M, N Shiraishi, and H Shirato (1992). "Rain-wind induced vibration of cables of cable-stayed bridges". In: *Journal of wind engineering and industrial aerodynamics* 43.1-3, pp. 2011–2022.

Matsumoto, M et al. (1990). "Aerodynamic behavior of inclined circular cylinders-cable aerodynamics". In: *Journal of Wind Engineering and Industrial Aerodynamics* 33.1-2, pp. 63–72.

Matsumoto, Masaru et al. (2010). "Dry galloping characteristics and its mechanism of inclined/yawed cables". In: *Journal of Wind Engineering and Industrial Aerodynamics* 98.6, pp. 317–327.

Matsumura, Toshio et al. (2002). "Development of Low Wind-Pressure Insulated Wires". In: *Furukawa Electric Review*, pp. 39–44.

Miklosovic, DS et al. (2004). "Leading-edge tubercles delay stall on humpback whale (Megaptera novaeangliae) flippers". In: *Physics of Fluids* 16.5, pp. L39–L42.

Mittal, Sanjay (2016). "Lock-in in vortex-induced vibration". In: *Journal of Fluid Mechanics* 794, pp. 565–594.

Mittal, Sanjay and Saurav Singh (2005). "Vortex-induced vibrations at subcritical Re". In: *Journal of Fluid Mechanics* 534, pp. 185–194.

Monkewitz, Peter A (1988). "The absolute and convective nature of instability in two-dimensional wakes at low Reynoldss numbers". In: *The Physics of fluids* 31.5, pp. 999–1006.

Morse, TL and CHK Williamson (2009). "Prediction of vortex-induced vibration response by employing controlled motion". In: *Journal of Fluid Mechanics* 634, pp. 5–39.

Nakamura, Hajime (2011). "Suppression of Fluctuating Lift on a Circular Cylinder by Attaching Cylindrical Rings". In: *Journal of Fluid Science and Technology* 6.6, pp. 1036–1050.

Nakamura, Hajime and Tamotsu Igarashi (2008). "Omnidirectional reductions in drag and fluctuating forces for a circular cylinder by attaching rings". In: *Journal of wind engineering and industrial aerodynamics* 96.6, pp. 887–899.

Nakamura, Y (1996). "Vortex shedding from bluff bodies and a universal Strouhal number". In: *Journal of fluids and structures* 10.2, pp. 159–171.

Nakamura, Y and Y Tomonari (1982). "The effects of surface roughness on the flow past circular cylinders at high Reynolds numbers". In: *Journal of Fluid Mechanics* 123, pp. 363–378.

Navrose and Sanjay Mittal (2013). "Free vibrations of a cylinder: 3-D computations at Re= 1000". In: *Journal of Fluids and Structures* 41, pp. 109–118.

— (2016). "Lock-in in vortex-induced vibration". In: *Journal of Fluid Mechanics* 794, pp. 565–594.

Nebres, J and S Batill (1992). "Flow about cylinders with helical surface protrusions". In: *30th Aerospace Sciences Meeting and Exhibit*, p. 540.

Norberg, C (1998). "LDV-measurements in the near wake of a circular cylinder". In: *ASME Paper No. FEDSM98-521*.

Norberg, Christoffer (2003). "Fluctuating lift on a circular cylinder: review and new measurements". In: *Journal of Fluids and Structures* 17.1, pp. 57–96.

O'Brien, PJ, EJ O'Sullivan, et al. (1999). "The Role of buoyancy in deepwater riser design". In: *Offshore Technology Conference*. Offshore Technology Conference.

Owen, John C, Peter W Bearman, and Albin A Szewczyk (2001). "Passive control of VIV with drag reduction". In: *Journal of Fluids and Structures* 15.3, pp. 597–605.

Ozono, Shigehira (1999). "Flow control of vortex shedding by a short splitter plate asymmetrically arranged downstream of a cylinder". In: *Physics of Fluids* 11.10, pp. 2928–2934.

Park, Hongrae, R Ajith Kumar, and Michael M Bernitsas (2013). "Enhancement of flow-induced motion of rigid circular cylinder on springs by localized surface roughness at $3 \times 10^4 \leq Re \leq 1.2 \times 10^5$". In: *Ocean Engineering* 72, pp. 403–415.

Pastò, S (2008). "Vortex-induced vibrations of a circular cylinder in laminar and turbulent flows". In: *Journal of Fluids and Structures* 24.7, pp. 977–993.

Placzek, Antoine, Jean-Francois Sigrist, and Aziz Hamdouni (2009). "Numerical simulation of an oscillating cylinder in a cross-flow at low Reynolds number: Forced and free oscillations". In: *Computers & Fluids* 38.1, pp. 80–100.

Prasad, Anil and Charles HK Williamson (1997). "The instability of the shear layer separating from a bluff body". In: *Journal of fluid mechanics* 333, pp. 375–402.

Ramberg, SE (1983). "The effects of yaw and finite length upon the vortex wakes of stationary and vibrating circular cylinders". In: *Journal of Fluid Mechanics* 128, pp. 81–107.

Rodríguez, I et al. (2015). "On the flow past a circular cylinder from critical to supercritical Reynoldss numbers: Wake topology and vortex shedding". In: *International Journal of Heat and Fluid Flow* 55, pp. 91–103.

Roshko, Anatol (1954a). "On the development of turbulent wakes from vortex streets". In: *NACA Technical Note No. 1190*.

— (1954b). *On the drag and shedding frequency of two-dimensional bluff bodies*. Tech. rep. DTIC Document.

— (1955). "On the wake and drag of bluff bodies". In: *Journal of the aeronautical sciences* 22.2.

Sarpkaya, T (2004). "A critical review of the intrinsic nature of vortex-induced vibrations". In: *Journal of Fluids and Structures* 19.4, pp. 389–447.

Schewe, Günter (1983). "On the force fluctuations acting on a circular cylinder in crossflow from subcritical up to transcritical Reynoldss numbers". In: *Journal of fluid mechanics* 133, pp. 265–285.

Schumm, Michael, Eberhard Berger, and Peter A Monkewitz (1994). "Self-excited oscillations in the wake of two-dimensional bluff bodies and their control". In: *Journal of Fluid Mechanics* 271, pp. 17–53.

Sears, Wo R (1948). "The boundary layer of yawed cylinders". In: *Journal of the Aeronautical Sciences* 15.1, pp. 49–52.

Seo, Seong-Ho et al. (2013). "Drag Reduction of a Bluff Body by Grooves Laid Out by Design of Experiment". In: *Journal of Fluids Engineering* 135.11, p. 111202.

Shao, Chuan Ping and Qing Ding Wei (2008). "Control of vortex shedding from a square cylinder". In: *AIAA journal* 46.2, pp. 397–407.

Shao, Chuanping and Jianming Wang (2007). "Control of mean and fluctuating forces on a circular cylinder at high Reynolds numbers". In: *Acta Mechanica Sinica* 23.2, pp. 133–143.

Shewchuk, Jonathan Richard et al. (1994). *An introduction to the conjugate gradient method without the agonizing pain*.

Smagorinsky, Joseph (1963). "General circulation experiments with the primitive equations: I. the basic experiment". In: *Monthly Weather Review* 91.3, pp. 99–164.

Stankiewicz, Witold et al. (2015). "Modal decomposition-based global stability analysis for reduced order modeling of 2D and 3D wake flows". In: *International Journal for Numerical Methods in Fluids*.

Stappenbelt, Brad, Farhad Lalji, and Garry Tan (2007). "Low mass ratio vortex-induced motion". In: *16th Australasian Fluid Mechanics Conference*. 2-7 December, Crown Plaza, Gold Coast, Australia, pp. 1491–1497.

Strykowski, PJ and KR Sreenivasan (1990). "On the formation and suppression of vortex 'shedding'at low Reynoldss numbers". In: *Journal of Fluid Mechanics* 218, pp. 71–107.

Sumer, B Mutlu and Jørgen Fredsøe (2006). *Hydrodynamics around cylindrical strucures*. Vol. 26. World scientific.

Surry, D and J Surry (1967). "The effect of inclination on the Strouhal number and other wake properties of circular cylinders at subcritical Reynoldss numbers". In: *Technical Report*.

Svensson, Holger (2013). *Cable-stayed bridges: 40 years of experience worldwide*. John Wiley & Sons.

Taira, Kunihiko et al. (2017). "Modal Analysis of Fluid Flows: An Overview". In: *arXiv preprint arXiv:1702.01453*.

Theofilis, Vassilios (2011). "Global linear instability". In: *Annual Review of Fluid Mechanics* 43, pp. 319–352.

Tombazis, N and PW Bearman (1997). "A study of three-dimensional aspects of vortex shedding from a bluff body with a mild geometric disturbance". In: *Journal of Fluid Mechanics* 330, pp. 85–112.

Tu, Jiahuang et al. (2014). "Flow-induced vibration on a circular cylinder in planar shear flow". In: *Computers & Fluids* 105, pp. 138–154.

Van Atta, C.W. (1968). "Experiments on vortex shedding from yawed circular cylinders". In: *AIAA Journal* 6.5, pp. 931–933.

Versteeg, Henk Kaarle and Weeratunge Malalasekera (2007). *An introduction to computational fluid dynamics: the finite volume method*. Pearson Education.

Vo, Hung D et al. (2016). "A wind tunnel study on control methods for cable dry-galloping". In: *Frontiers of Structural and Civil Engineering* 10.1, pp. 72–80.

Weber, Paul W et al. (2011). "Computational evaluation of the performance of lifting surfaces with leading-edge protuberances". In: *Journal of Aircraft* 48.2, pp. 591–600.

Wehrmann, OH (1965). "Reduction of Velocity Fluctuations in a Karman Vortex Street by a Vibrating Cylinder". In: *Physics of Fluids (1958-1988)* 8.4, pp. 760–761.

Wei, Zhaoyu, TH New, and YD Cui (2015). "An experimental study on flow separation control of hydrofoils with leading-edge tubercles at low Reynolds number". In: *Ocean Engineering* 108, pp. 336–349.

Williamson, CHK (1988). "The existence of two stages in the transition to three-dimensionality of a cylinder wake". In: *The Physics of fluids* 31.11, pp. 3165–3168.

— (1996). "Three-dimensional wake transition". In: *Journal of Fluid Mechanics* 328, pp. 345–407.

Williamson, CHK and R Govardhan (2004). "Vortex-induced vibrations". In: *Annual Review of Fluid Mechanics* 36, pp. 413–455.

Williamson, CHK and A Roshko (1988). "Vortex formation in the wake of an oscillating cylinder". In: *Journal of fluids and structures* 2.4, pp. 355–381.

Witte, Matthias et al. (2012). "On the wake flow dynamics behind harbor seal vibrissae–a fluid mechanical explanation for an extraordinary capability". In: *Nature-inspired fluid mechanics*. Springer, pp. 271–289.

Wood, Cc J (1964). "The effect of base bleed on a periodic wake". In: *Journal of the Royal Aeronautical Society* 68.643, pp. 477–482.

Yeo, DongHun and Nicholas P Jones (2008). "Investigation on 3-D characteristics of flow around a yawed and inclined circular cylinder". In: *Journal of Wind Engineering and Industrial Aerodynamics* 96.10, pp. 1947–1960.

Yoon, HS et al. (2011). "Effect of the wavy leading edge on hydrodynamic characteristics for flow around low aspect ratio wing". In: *Computers & Fluids* 49.1, pp. 276–289.

Zdravkovich, MM (1997). *Flow around circular cylinders, vol. 1: Fundamentals,*

— (2003). "Flow around circular cylinders, vol. 2: Applications". In: *Oxford University Press, ISBN 0* 19.856561, p. 5.

Zebib, A (1987). "Stability of viscous flow past a circular cylinder". In: *Journal of Engineering Mathematics* 21.2, pp. 155–165.

Zhang, Kai et al. (2016). "Numerical study on the effect of shape modification to the flow around circular cylinders". In: *Journal of Wind Engineering and Industrial Aerodynamics* 152, pp. 23–40.

Zhang, Wei, Sang Joon Lee, et al. (2005). "PIV measurements of the near-wake behind a sinusoidal cylinder". In: *Experiments in Fluids* 38.6, pp. 824–832.

Zhang, Weiwei et al. (2015). "Mechanism of frequency lock-in in vortex-induced vibrations at low Reynolds numbers". In: *Journal of Fluid Mechanics* 783, pp. 72–102.

Zhao, Ming, Liang Cheng, and Tongming Zhou (2009). "Direct numerical simulation of three-dimensional flow past a yawed circular cylinder of infinite length". In: *Journal of Fluids and Structures* 25.5, pp. 831–847.

Zhao, Ming et al. (2013). "Three-dimensional transition of vortex shedding flow around a circular cylinder at right and oblique attacks". In: *Physics of Fluids* 25.1, p. 014105.

Zhao, Ming et al. (2014). "Three-dimensional numerical simulation of vortex-induced vibration of an elastically mounted rigid circular cylinder in steady current". In: *Journal of Fluids and Structures* 50, pp. 292–311.

Zhou, T et al. (2009). "Dependence of the wake on inclination of a stationary cylinder". In: *Experiments in Fluids* 46.6, pp. 1125–1138.

Zhou, T et al. (2011). "On the study of vortex-induced vibration of a cylinder with helical strakes". In: *Journal of Fluids and Structures* 27.7, pp. 903–917.